NASA TECHNICAL MEMORANDUM

NASA TM X-53217

MARCH 1, 1965

NASA TM X-53217

ASTRIONICS RESEARCH AND DEVELOPMENT REPORT NO. 3

ASTRIONICS LABORATORY
RESEARCH AND DEVELOPMENT OPERATIONS
GEORGE C. MARSHALL SPACE FLIGHT CENTER
HUNTSVILLE, ALABAMA

NASA TM X -53217

NATIONAL AERONAUTICS AND SPACE ADMINISTRATION
WASHINGTON, D.C.

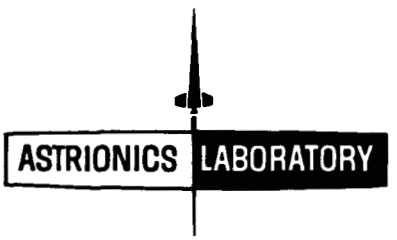

ASTRIONICS RESEARCH AND DEVELOPMENT REPORT NO. 3

FOR THE PERIOD JANUARY 1, 1964 THROUGH DECEMBER 31, 1964

ASTRIONICS LABORATORY
RESEARCH AND DEVELOPMENT OPERATIONS
GEORGE C. MARSHALL SPACE FLIGHT CENTER
HUNTSVILLE, ALABAMA

MARCH 1, 1965

preface...

This document is the third issue of a Research and Development Report prepared by the Astrionics Laboratory, Research and Development Operations, George C. Marshall Space Flight Center, Huntsville, Alabama.

The subjects discussed cover technical information that, we believe, will be interesting and helpful to other organizations engaged in space flight and related efforts.

Reprints of these articles may be obtained from the NASA Library, MSFC, Huntsville, Alabama

W. Haeussermann

W. HAEUSSERMANN
Director, Astrionics Laboratory

ASTRIONICS LABORATORY / 1965

GEORGE C. MARSHALL SPACE FLIGHT CENTER
NATIONAL AERONAUTICS AND SPACE ADMINISTRATION
HUNTSVILLE, ALABAMA

CONTENTS...

I. GUIDANCE AND CONTROL SYSTEMS AND COMPONENTS

II. INSTRUMENTATION SYSTEMS

III. PUBLICATIONS AND PRESENTATIONS

acknowledgments...

The articles for this report were contributed by various engineers and physicists of the Astrionics Laboratory, reviewed and compiled by Hubert E. Kroh, and edited by Jeanene Flowers.

Grateful acknowledgment is given to the Technical Publications Section and the Astrionics Support Unit, Graphic Engineering and Model Studies Branch, Management Services Office, MSFC, for preparing the report.

I. GUIDANCE AND CONTROL SYSTEMS AND COMPONENTS

A. INTRODUCTION TO THE KALMAN-SCHMIDT FILTER

by John W. Kenelly and Kenneth S. Williamson

This article provides an insight into the application of the Kalman-Schmidt filter to navigation for technical personnel with limited background in probability theory. The scope of the article includes the statistical derivation of the Kalman-Schmidt filter within the context of space flight navigation. The filter may be used to locate a space vehicle and to determine its velocity vector from data containing random errors. The filter is superior to least squares because each observation datum does not have to determine the position of the vehicle.

INTRODUCTION

Space navigation includes the determination of position and velocity of a vehicle by onboard or earth based measurements of range, range rate, or various combinations of star-planet, sun-planet angular position fixes. The instruments used in making the measurements are not perfect and will produce errors. One method of handling the errors (i.e., data reduction of the measurement) is the Kalman-Schmidt filter theory, which is a mathematical method of processing data to remove errors in measurement. Since the filter* only receives as input inaccurate measurements, precise determination of position and velocity is not possible. However, with reasonable instrumentation, the Kalman-Schmidt filter can give results that will minimize errors.

The mathematical background for the Kalman-Schmidt filter was performed by Kalman (Ref. 1). Schmidt was the first to notice that Kalman's results could be applied to space navigation (Ref. 2). Varied applications have been studied by the National Aeronautics and Space Administration. Because the original paper by Kalman is highly theoretical, several papers have been written for the purpose of bringing the results as applied to navigation direct to the engineer. This article is one of these papers and includes necessary navigational background. The reader needs only a slight acquaintance with matrices and statistics. This article should provide insight into the data reduction problems of navigation and into the Kalman-Schmidt filter. This insight will be of value in programing and studying a computer simulation of the navigation problem.

*In this article, the term "filter" denotes a mathematical method or computer device that receives noisy measurements (i.e., measurements with superimposed error) and puts out a more realistic approximation of the trajectory.

NOMENCLATURE

t_n	time of n^{th} set of measurements
X_n	state (column) vector at t_n. X_n is a perturbation vector; i.e., X_n is the difference between the actual trajectory and the standard or reference trajectory at time t_n.
Y_n	measurement (column) vector at t_n. Y_n is also a perturbation vector; i.e., Y_n is the difference between the measurables on the trajectory and the reference.
Y_n^{*m}	the value of the perturbation vector Y_n of measurements that are indicated by the instrumentation; i.e., Y_n^{*m} is the perturbation of the measurement of Y_n.

u_n — $Y_n^{*m} = Y_n + u_n$; i.e., u_n is a zero mean random noise (column) vector. u_n is the error made by the measuring instruments.

Q_n — $Q_n = E(u_n u_n^T)$; i.e., Q_n is the covariance of the noise u_n. Q_n is given information, and the noise u_n at time t_n is given to be uncorrelated with the noise at any time not t_n, i.e., any different time t_m.

$\varphi_{n+1,n}$ — $X_{n+1} = \varphi_{n+1,n} X_n$; i.e., $\varphi_{n+1,n}$ is the state transition matrix, mentioned previously, which translates X_n into X_{n+1}. This matrix can be precomputed before a mission.

M_n — $Y_n = M_n X_n$ or $X_n = M_n^{-1} Y_n$. M_n is the geometry mapping matrix, mentioned previously and precomputable, which maps the measurement perturbation vector Y_n into the state perturbation vector X_n.

X_n^* — the best estimate of X_n as determined by the filter to be derived. X_n^* is a filter approximation of X_n and is based on the given statistics and all measurement vectors Y_n^{*m} taken prior to time t_n. $E(X_n^* - X_n) = 0$. (E is the expected value operator and is a statistical average. $E(X_n^* - X_n) = 0$ states that the average value of the approximation X_n^* of X_n is X_n or equivalently that the difference is zero.)

$\overline{X}_{n+1}$ — the projection of the perturbation vector X_n^* of time t_n into $\overline{X}_{n+1}$ at time t_{n+1}; i.e., $\overline{X}_{n+1} = \varphi_{n+1,n} X_n^*$. Since E is a linear operator, and $\varphi_{n+1,n}$ is a constant matrix, $\varphi_{n+1,n}$ can pass directly over the expected value operator E. $E(X_n^* - X_n) = 0$, $E(X_n^*) - E(X_n) = 0$, $E(X_n^*) = X_n$, $\varphi_{n+1,n} E(X_n^*) = \varphi_{n+1,n} X_n$, and finally $E(\overline{X}_{n+1}) = X_{n+1}$, from assumptions in the definition of X_n^* above.

$\overline{Y}_n$ — $\overline{Y}_n = M_n X_n^*$; $\overline{Y}_n$ is an estimate of $\overline{Y}_n^{*m}$

$E(\overline{Y}_n) = E(M_n X_n^*) = M_n E(X_n^*)$

$E(\overline{Y}_n) = M_n X_n$

$E(\overline{Y}_n) = Y_n$ or the average value of the perturbation measurement vector Y_n. The difference between $\overline{Y}_n$ and Y_n is that $\overline{Y}_n$ also contains instrument noise, where Y_n does not.

$\delta\overline{X}_n$ — error in $\overline{X}_n$

$\delta\overline{X}_n = \overline{X}_n - X_n$

$\delta\overline{Y}_n$ — error in $\overline{Y}_n$

$\delta\overline{Y}_n = \overline{Y}_n - Y_n^{*m} = M_n X_n^{*m}$

Also, $E(Y_n^{*m}) = Y_n$ and since $E(\overline{Y}_n) = Y_n$

then $E(\delta\overline{Y}_n) = E(Y_n) - E(Y_n^{*m}) = Y_n - Y_n = 0$

$\delta\overline{X}_{n+1}^*$ — the best estimate (or approximation) of $\delta\overline{X}_n$, $\delta\overline{X}_{n+1}^* = \overline{X}_n - X_n^*$

P_n^* — given statistics; i.e., the covariance matrix of errors in the state vector X_n

$P_n^* = E[(X_n^* - X_n)(X_n^* - X_n)^T]$

DERIVATION OF KALMAN-SCHMIDT FILTER

The Kalman-Schmidt filter as applied to a typical space navigation problem is derived in this section. In particular that part of a mission in which position and velocity are determined is examined. Deviations from a reference trajectory are assumed where the reference trajectory is calculated by a computer before the mission. The advantage of using a reference trajectory lies chiefly in the capability of precalculating two kinds of transition (or mapping) matrices.

The two matrices are the state-transition matrix $\varphi_{n+1,n}$ and the geometry mapping matrix M_n. The geometry mapping matrix maps the measurements into the state (position and velocity), and the state-transition matrix translates the state at time t_n into the state at a later time t_{n+1}.

The state-transition and geometry mapping matrices are approximations based on the assumption that the trajectory is not perturbed far from the standard. In general, the matrices will not work for large deviations.

A theorem from statistics (Ref. 3) relates some of the vectors by $\delta\overline{X}^*_{n+1} = [E(\delta\overline{X}_{n+1}\ \delta\overline{Y}_n^T)]\ [E(\delta\overline{Y}_n\ \delta\overline{Y}_n^T)]^{-1}\ \delta\overline{Y}_n$.

This statement is the core of the derivation of the filter and it only remains to rearrange these terms into more useful relations.

Note that the matrices $\varphi_{n+1,n}$ and M_n translate and map any perturbation vector near the reference; i.e., one definition says $\overline{X}_{n+1} = \varphi_{n+1}\ X^*_n$ since X^*_n is sufficiently close to the reference.

Figures 1 and 2 illustrate the action of a filter. The filter receives continuous or discrete noisy measurements of a trajectory and then puts out an estimated trajectory. The smooth lines represent the actual trajectory and are included for convenience since a filter would have no knowledge of the actual trajectory.

The trajectory and reference are shown along with the perturbation state vector X_n in Figure 3. The measurement perturbation vectors Y_n and Y_n^{*m} are given in the equations. The angles shown are included for convenience. The star-planet etc. fixes are not sufficient to determine a velocity component for the state vector X_n in one measurement.

Note that there is a one-to-one correspondence between X_n and Y_n and that $Y_n = M_n X_n$, and it is not necessary to clutter the illustrations unnecessarily with measurement perturbation vectors. Again, assuming there is a measurement vector Y_n which determines a state vector X_n, then any illustration of state vectors implies a corresponding illustration of measurement vectors.

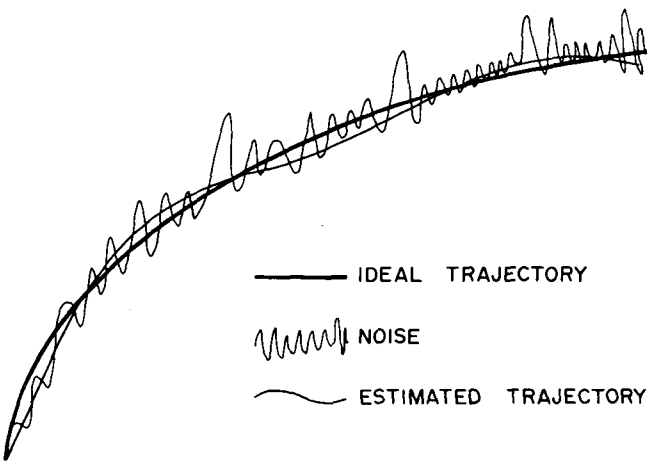

FIGURE 1. FILTERING OF CONTINUOUS NOISE

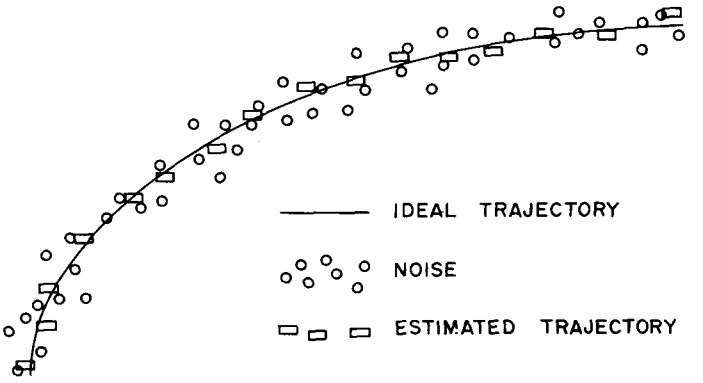

FIGURE 2. FILTERING OF DISCRETE NOISE

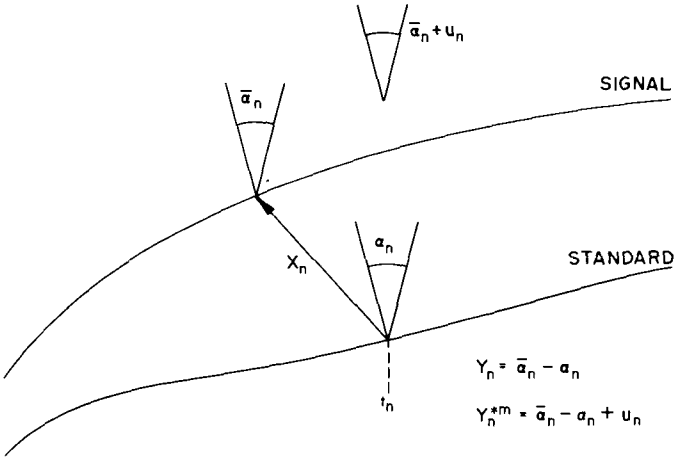

FIGURE 3. MEASUREMENTS ON TRAJECTORY

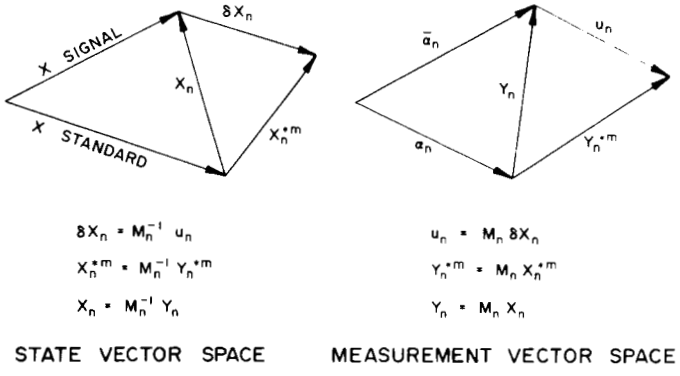

FIGURE 4. GEOMETRY MAPPING MATRIX – M_n

Figure 4 further illustrates the correspondence between state and measurement perturbation vectors. The similarities are self-explanatory. δX_n and X_n^{*m} were not in the definitions and are included for illustration. Note that only state vectors need be drawn because of the correspondence.

Figure 5 illustrates the state transition matrix and is self-explanatory.

Measurement vectors Y_n^{*m} are taken at predetermined time steps. After each estimate, the filter revises its estimation of the state vector X_n (the estimate of X_n is X_n^*).

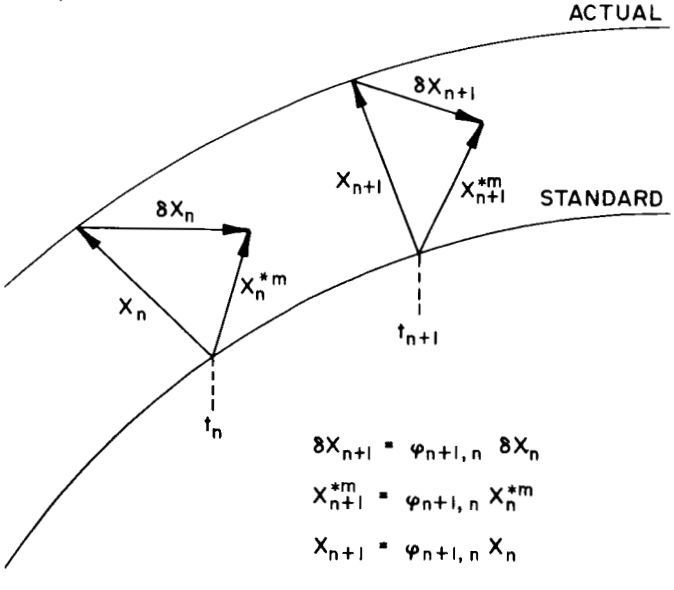

FIGURE 5. STATE TRANSITION MATRIX – $\varphi_{n+1,\,n}$

Figure 6 is not as complex as it first appears if it is noted that the vectors at t_{n-1}, t_n, and t_{n+1} are the same, with the exception of δX_n, which corresponds to $\delta \overline{Y}_n$. The parallel curves to the reference are estimated trajectories for times t_{n-3}, t_{n-2}, t_{n-1}, and t_n, respectively, going from bottom to top. At time t_{n-1}, X_{n-1}^* is the best estimate of X_n, Y_{n-1}^{*m} is taken, and the filter yields X_{n+1}^*, and so on. Thus the filter updates the estimated trajectory each time a measurement is taken. Only the vectors X_n^* and $\overline{X}_{n+1}$ and δY_n are used to update X_n^* when Y_n^{*m} is measured into X_{n+1}^*.

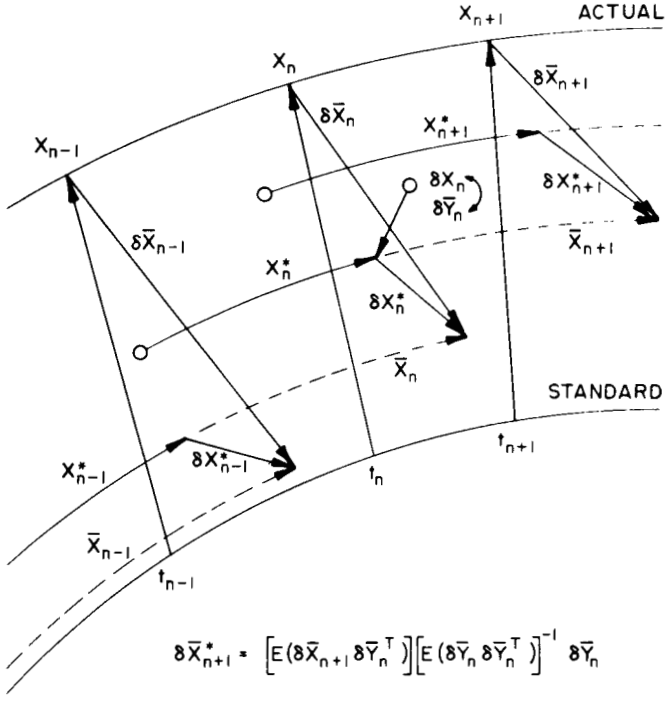

FIGURE 6. GEOMETRY OF VECTORS USED BY FILTER

The fundamental theorem previously mentioned is now stated: Let $\delta \overline{Y}_n$ and $\delta \overline{X}_{n+1}$ be two column vector random variables, not necessarily of the same dimension with zero means; then the best linear estimate

$\delta \overline{X}_{n+1}^*$ of $\delta \overline{X}_{n+1}$ is given $\delta \overline{Y}_n$,

$$\delta \overline{X}_{n+1}^* = [E(\delta \overline{X}_{n+1}\, \delta \overline{Y}_n^T)]\,[E(\delta \overline{Y}_n\, \delta \overline{Y}_n^T)]^{-1}\, \delta \overline{Y}_n$$

where "best" means that the covariance matrix of the

TABLE 1. PERTINENT DETAILS*

T 1. Definition - A random variable is statistical and a constant variable is nonstatistical.

T 2. $E(A + B) = E(A) + E(B)$; A and B are random

T 3. $E(C) = C$; C is a constant

T 4. $E(CA) = CE(A)$; C is constant and A is random

T 5. $E(AB) = 0$, if A and B are uncorrelated

T 6. $(AB)^T = B^T A^T$

T 7. $AX = B \Rightarrow X = A^{-1} B$

T 8. $(A + B)^T = A^T + B^T$, $(DA + DB)^T = (A+B)^T D^T$

T 9. $Y_n^{*m} = Y_n + u_n$

T 10. $Q_n = E(u_n u_n^T)$

T 11. $X_{n+1} = \varphi_{n+1,n} X_n$

T 12. $Y_n = M_n X_n$

T 13. $E(X_n^* - X_n) = 0$

T 14. $E(\overline{X}_{n+1}) = X_{n+1}$

T 15. $\overline{Y}_n = M_n X_n^*$; $E(\overline{Y}_n) = M_n E(X_n^*)$

$= M_n X_n$; $E(Y_n) = Y_n$

T 16. $\delta\overline{X}_n = \overline{X}_n - X_n$

T 17. $\delta\overline{Y}_n = \overline{Y}_n - Y_n^{*m} = M_n X_n^{*m}$

$- Y_n^{*m}$, $E(\delta\overline{Y}_n) = 0$

T 18. $\delta\overline{X}_n^* = \overline{X}_n - X_n^*$

T 19. $P_n^* = E[(X_n^* - X_n)(X_n^* - X_n)^T]$

* Numbers on the left are referred to in the following equations.

error in $\delta\overline{X}_{n+1}^*$ is such that variance in the estimate of any quantity $\psi = A^T \delta\overline{X}_{n+1}$ is minimized, or

$\delta_\psi^2 = E[(\psi - \tilde{\psi})(\psi - \tilde{\psi})^T]$

is a minimum ($\tilde{\psi} = A^T \delta\overline{X}_{n+1}^*$).

Table 1 shows all usable material in the derivation. Note that P_n^* and Q_n must appear in the result because they are the only given statistics.

The first step in the derivation consists in solving and substituting for the three factors in the equation from the theorem.

Theorem,

$$\delta\overline{X}_{n+1}^* = [E(\delta\overline{X}_{n+1}\, \delta\overline{Y}_n^T)][E(\delta\overline{Y}_n\, \delta\overline{Y}_n^T)]^{-1} \delta Y_n$$

Part 1.

$$E(\delta\overline{Y}_n\, \delta\overline{Y}_n^T) = E[(\overline{Y}_n - Y_n^{*m})(\overline{Y}_n - Y_n^{*m})^T] \quad (T\ 17)$$

$$= E[(\overline{Y}_n - Y_n - u_n)(\overline{Y}_n - Y_n - u_n)^T] \quad (T\ 9)$$

$$= E[\{M_n(X_n^* - X_n) - u_n\}\{(X_n^* - X_n)^T M_n^T - u_n^T\}] \quad (T\ 12, 15, 8)$$

$$= M_n E[(X_n^* - X_n)(X_n^* - X_n)^T]\, M_n^T + E(u_n u_n^T)$$

$$- E[M_n(X_n^* - X_n)\, u_n^T] - E[u_n(X_n^* - X_n)^T]. \quad (T\ 4, 6)$$

Since $E[X_n^* - X_n] = 0$, this reduces to

$$= M_n P_n^* M_n^T + Q_n. \quad (T\ 10, 19, 5)$$

Part 2.

$$E(\delta\overline{X}_{n+1}\ \delta\overline{Y}_n^T) = E[(\overline{X}_{n+1} - X_{n+1})\ (\overline{Y}_n - Y_n^{*\,m})^T]$$

(T 16,17)

$$= \varphi_{n+1,n}\, E[(X_n^* - X_n)\{(X_n^* - X_n)^T M_n^T - u_n^T\}]$$

(T 4,11,8,9)

$$= \varphi_{n+1,n}\, E[(X_n^* - X_n)\ (X_n^* - X_n)^T]\ M_n^T$$

$$- \varphi_{n+1,n}\, E[(X_n^* - X_n)\ u_n^T] \qquad \text{(T 5,8)}$$

$$E(\delta\overline{X}_{n+1}\ \delta\overline{Y}_n^T) = \varphi_{n+1,n}\, P_n^*\, M_n^T \qquad \text{(T 19)}$$

since $E[X_n^* - X_n] = 0$.

Part 3. Parts 1 and 2 give substitution for the theorem and

$$\delta\overline{X}_{n+1}^* = [\varphi_{n+1,n}\, P_n^*\, M_n^T]\ [M_n P_n^*\, M_n^T + Q_n]^{-1} \delta\overline{Y}_n$$

$$\overline{X}_{n+1} - X_{n+1}^* = [\varphi_{n+1,n}\, P_n^*\, M_n^T][M_n P_n^*\, M_n^T + Q_n]^{-1}$$

$$\times\ (M_n X_n^* - Y_n^{*\,m}). \qquad \text{(T 18,17,12)}$$

Therefore

$$X_{n+1}^* = \varphi_{n+1,n}\, X_n^* - \varphi_{n+1,n} P_n^* M_n^T (M_n P_n^* M_n^T + Q_n)^{-1}$$

$$\times\ (M_n X_n^* - Y_n^{*\,m})$$

which is the prediction of the filter in terms of known matrices.

Now some substitutions are made and P_n^* is iterated into P_{n+1}^*. The covariance matrix P_{n+1}^* is updated from P_n^* because each observation changes the covariance matrix.

Rearranging X_{n+1}^*,

$$X_{n+1}^* = [\varphi_{n+1,n} - \varphi_{n+1,n}\, P_n^* M_n^T (M_n P_n^* M_n^T + Q_n)^{-1} M_n]\ X_n^* + [(\varphi_{n+1,n}\, P_n^* M_n^T)\ M_n P_n^{*} M_n^T + Q_n]^{-1}\ Y_n^{*\,m}.$$

Let

$$\Delta_n^* = \varphi_{n+1,n}\, P_n^*\, M_n^T (M_n P_n^*\, M_n^T + Q_n)^{-1}$$

then

$$X_{n+1}^* = [\varphi_{n+1,n} - \Delta_n^*\, M_n]\ X_n^* + \Delta_n^*\, Y_n^{*\,m}.$$

Let

$$\varphi_{n+1,n}^* = \varphi_{n+1,n} - \Delta_n^*\, M_n$$

then

$$X_{n+1}^* = \varphi_{n+1,n}^*\, X_n^* + \Delta_n^*\, Y_n^{*\,m}.$$

Next P_n^* into P_{n+1}^* is derived. Observe

$$P_{n+1}^* = E[(X_{n+1}^* - X_{n+1})\ (X_{n+1}^* - X_{n+1})^T].$$

$$X_{n+1}^* - X_{n+1} = \varphi_{n+1,n}^*\, X_n^* + \Delta_n^*\, Y_n^{*\,m} - \varphi_{n+1,n}\, X_n$$

$$+ (\varphi_{n+1,n}^*\, X_n - \varphi_{n+1,n}^*\, X_n)$$

$$= \varphi_{n+1,n}^*\, (X_n^* - X_n) + \varphi_{n+1,n}^*\, X_n - \varphi_{n+1,n}\, X_n$$

$$+ \Delta_n^*\, Y_n + \Delta_n^*\, u_n$$

$$= \varphi_{n+1,n}^*\, (X_n^* - X_n) + (\varphi_{n+1,n}^* - \varphi_{n+1,n}$$

$$+ \Delta_n^*\, M_n)\ X_n + \Delta_n^*\, u_n$$

$$X_{n+1}^* - X_{n+1} = \varphi_{n+1,n}^*\, (X_n^* - X_n) + \Delta_n^*\, u_n$$

since $(\varphi_{n+1,n}^* - \varphi_{n+1,n}) = 0$

$$P_{n+1}^* = E[\{\varphi_{n+1,n}^*\, (X_n^* - X_n) + \Delta_n^*\, u_n\}\ \{\varphi_{n+1,n}^*\, (X_n^*$$

$$- X_n) + \Delta_n^*\, u_n^T\}]$$

$$P^*_{n+1} = \varphi^*_{n+1,n} P^*_n \varphi^{*T}_{n+1,n} + \Delta^*_n Q_n \Delta^{*T}_n$$

$$P^*_{n+1} = \varphi^*_{n+1,n} P^*_n [\varphi^{*T}_{n+1,n} + (\varphi^T_{n+1,n} - \varphi^T_{n+1,n})] + \Delta^*_n Q_n \Delta^{*T}_n.$$

Finally

$$P^*_{n+1} = \varphi^*_{n+1,n} P^*_n \varphi_{n+1,n} + \{\varphi^*_{n+1,n} P^*_n [\varphi^{*T}_{n+1,n} - \varphi^T_{n+1,n}] + \Delta^*_n Q_n \Delta^{*T}_n\}.$$

Now, $(\varphi^{*T}_{n+1,n} - \varphi^T_{n+1,n}) = 0$. This is shown to be true by the following

$$\varphi^*_{n+1,n} P^*_n (\varphi^*_{n+1,n} - \varphi_{n+1,n})^T + \Delta^*_n Q_n \Delta^{*T}_n = 0$$

$$\varphi^*_{n+1,n} P^*_n (-\Delta^*_n M_n)^T + \Delta^*_n Q_n \Delta^{*T}_n = 0$$

by definition of $\varphi^*_{n+1,n}$.

$$[-\varphi^*_{n+1,n} P^*_n M^T_n + \Delta^*_n Q_n] \Delta^{*T}_n = 0.$$

Since

$$\varphi^*_{n+1,n} = \varphi_{n+1,n} - \Delta^*_n M_n$$

$$\varphi_{n+1,n} P^*_n M^T_n - \Delta^*_n M_n P^*_n M^T_n - \Delta^*_n Q_n = 0$$

$$\varphi_{n+1,n} P^*_n M^T_n - \Delta^*_n (M_n P^*_n M^T_n + Q_n) = 0$$

and since

$$\Delta^*_n = \varphi_{n+1,n} P^*_n M^T_n (M_n P^*_n M^T_n + Q_n)^{-1}$$

then

$$\varphi_{n+1,n} P^*_n M^T_n - \varphi_{n+1,n} P^*_n M^T_n = 0.$$

The final result is exhibited as follows. Given X^*_0, P^*_0, and tables for $\varphi_{n+1,n}$, M_n, and Q_n, then an onboard computational cycle is

$$\Delta^*_n = \varphi_{n+1,n} P^*_n M^T_n (M_n P^*_n M^T_n + Q_n)^{-1}$$

$$\varphi^*_{n+1,n} = \varphi_{n+1,n} - \Delta^*_n M_n$$

$$P^*_{n+1} = \varphi^*_{n+1,n} P^*_n \varphi^T_{n+1,n}$$

$$X^*_{n+1} = \varphi^*_{n+1,n} X^*_n + \Delta^*_n Y^{*m}_n$$

where the measurements of Y^{*m}_n are given each cycle. Some insight is given to these relations if Q_n or P^*_n equals zero. If $P^*_n = 0$,

$$\Delta^*_n = 0$$

$$\varphi^*_{n+1,n} = \varphi_{n+1,n}$$

$$P^*_{n+1} = 0$$

$$X^*_{n+1} = \varphi_{n+1,n} X^*_n.$$

These equations imply that no error in X^*_n from X_n is expected. No statistics are involved since only the transition matrix appears.

If $Q_n = 0$,

$$\Delta^*_n = \varphi_{n+1,n} M^{-1}_n$$

$$\varphi^*_{n+1,n} = \varphi_{n+1,n} - \varphi_{n+1,n} = 0$$

$$P^*_{n+1} = 0$$

$$X^*_{n+1} = \varphi_{n+1,n} M^{-1}_n Y^{*m}_n = \varphi_{n+1,n} X^{*m}_n.$$

These equations imply that the expected value of noise is zero, and Y^{*m}_n is Y_n. Thus $X^*_{n+1} = X_{n+1}$.

CONCLUSION

Since instrumentation will always contain some errors, some method of accounting for these errors is necessary. The basic cycle of the Kalman filter as applied to navigation is estimated trajectory, measurement, and new estimated trajectory.

If the four equations of the final result are recalled, onboard computation and updating of the statistics are seen to be possible.

The basic weakness of this derivation is the assumption that the actual trajectory is sufficiently close to the reference for the state transitions and geometry mapping matrices to function accurately. This restriction can be relaxed by obtaining operators (possibly a matrix of partials) to transform $\varphi_{n+1,n}$ and M_n such that the transformed values will function away from the reference.

REFERENCES

1. Kalman, R. E.; A New Approach to Linear Filtering and Prediction Problems, Journal of Basic Engineering, March 1960.

2. Smith, Gerald L., Schmidt, Stanley F., and McGee, Leonard A.; Applications of Statistical Filter Theory to the Optimal Estimation of Position and Velocity on Board a Circumlunar Vehicle, NASA TR 135, Washington, D. C.

3. Capabilities of MSFN for Apollo Guidance and Navigation, The Bissett-Berman Corp., Santa Monica, Calif., March 1964.

BIBLIOGRAPHY

1. McLean, John D., Schmidt, Stanley F., and McGee, Leonard A.; Optimal Filtering and Linear Prediction Applied to a Midcourse Navigation System for the Circumlunar Mission, NASA TN D-1208, Washington, D. C., March 1962.

2. Kalman, R. E., and Bucy, R. S.; New Results in Linear Filtering and Prediction Theory, Journal of Basic Engineering, March 1961.

B. A MATHEMATICAL METHOD TO DETERMINE THE ATTITUDE OF A SPHERE by Hans F. Kennel

A method for determining the attitude of a sphere without restricting its angular freedom is presented. Only the mathematical aspect of the problem is treated. Neither implementation nor accuracy of performance is discussed. The method has an application in spacecraft attitude simulators supported on spherical gas bearings.

The sphere is marked with three mutually perpendicular great circles and intersected in a minor circle by a stationary plane. The intersections of the great circles with the minor circle define the attitude of the sphere relative to the plane.

The orthogonal transformation matrix is developed, which allows the calculation of the Euler angles of any desired sequence.

INTRODUCTION

A method is needed for determining the instantaneous attitude of a sphere relative to a room-fixed reference coordinate system. The determination must be made without knowledge of the history of the sphere's angular motion. The described method accomplishes this and imposes no angular restrictions on the sphere. One application is for a spacecraft attitude simulation table supported by a spherical gas bearing. There will be other applications; therefore, the problem is treated in general.

The proposed method works as follows. The sphere is marked with three mutually perpendicular great circles as shown in Figure 1. The axes passing through the great circle intersections form the orthogonal sphere coordinate system. These intersections will henceforth be called axis pierce points. Each great circle is split into half circles and each circle

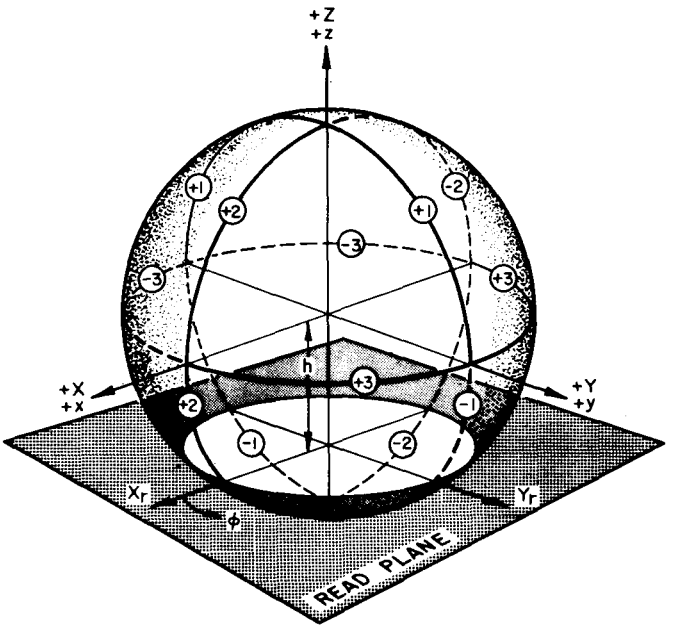

FIGURE 1. SPHERE MARKINGS

is marked or given some distinguishing characteristic. The six distinctly identifiable half circles prevent ambiguity in the attitude determination.

The half circles are applied to the sphere in such a way that each axis pierce point is formed by three half circles; one is continuous through the pierce point and the other two join at the pierce point. This is shown in Figure 2, which gives a direct view of any of the six axis pierce points of the sphere. This leaves two choices of orientation with respect to the sphere coordinate system; the end points of the half circle that passes through one axis may touch either of the remaining two axes. Once this choice is made, the orientation of all the half circles is fixed.

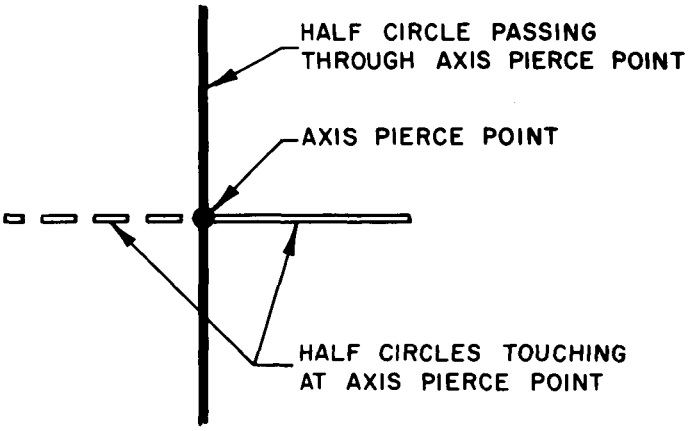

FIGURE 2. AXIS PIERCE POINT GEOMETRY

A stationary plane intersects the sphere in a minor circle. This plane (read plane, Fig. 1) must be located so that the radius r of the minor circle (read circle) is large enough to eliminate the possibility that in some cases it may be intersected by only one half circle, thus providing insufficient information for attitude determination (Fig. 3). This possibility is eliminated if a radius r greater than $R/\sqrt{2}$ is selected (where R is the radius of the sphere). Then, four or six intersections will occur, depending on the position of the sphere.

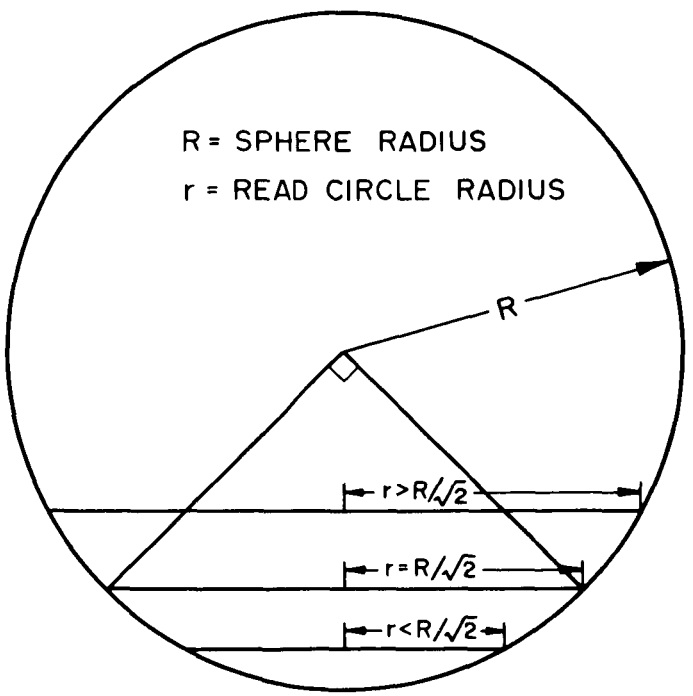

FIGURE 3. RELATIONSHIP OF r TO R

Angles are measured in the stationary read plane from a reference on the read circle to the intersections between the read circle and the half circles of the sphere. These angles, along with the identification of the half circles, uniquely define the attitude of the sphere with respect to the reference coordinate system.

The introduction of an additional coordinate system allows vast simplification of the problem. This additional coordinate system is superimposed on the sphere coordinate system in such a way (one of 24 possible ways) that its attitude can be determined without the aid of the half circle identifications. That is, for the attitude determination of the superimposed coordinate system with respect to the reference coordinate system, the sphere only needs to be marked with three great circles having no distinguishing characteristics.

The problem may now be solved in three distinct steps. First, the orthogonal transformation matrix from the reference coordinate system to the superimposed coordinate system is found. Second, the superimposed coordinate system is correlated with the sphere coordinate system, resulting in the orthogonal transformation matrix from the reference system to the sphere system. Third, the appropriate direction cosines of the orthogonal transformation matrix are used to calculate the selected rotation angles. The selection of the rotation angle sequence is arbitrary with respect to the method discussed here.

The following mathematical treatment assumes an ideal case, i.e., a perfect sphere, infinitely thin lines, perfect intersection angle information, etc. An error analysis for a practical case will be left to a future study, as will actual mechanization of the readout, identification of the intersection angles and half circles, and high speed digital data processing to allow readout with minimum time lag to accommodate the dynamics of a vehicle control loop. This loop is usually of low response for control investigations on gas bearing supported simulation tables.

NOMENCLATURE

a	direction cosine
h	distance along Z axis
i	subscript denoting x, y, or z

J	subscript denoting X, Y, or Z
L	half circle identification number (label)
r	read circle radius
r'	radius of the circle touching the three axis pierce points of a sphere octant
R	sphere radius
sgn L	$\triangleq L/\lvert L\rvert$
u, v, w	superimposed coordinate system
x, y, z	sphere coordinate system
X, Y, Z	reference coordinate system
X_r, Y_r, Z_r	coordinate system parallel to X, Y, Z with the Z and Z_r axes coinciding and the origin at Z = -h
α_u	angle between the -u axis and the XY plane
α_v	angle between the v axis and the XY plane (Fig. 4)
ϕ	angle from X_r, positive counterclockwise
ϕ_1, ϕ_2, etc.	angles of the half circle intersections with the read circle
ϕ_{u1}, ϕ_{u2}	pair of intersection angles caused by half circle(s) perpendicular to the u axis
ϕ_{v1}, ϕ_{v2}	pair of intersection angles caused by half circle(s) perpendicular to the v axis
ϕ_u	$\triangleq 0.5\ (\phi_{u2} + \phi_{u1})$
$\Delta\phi_u$	$\triangleq 0.5\ (\phi_{u2} - \phi_{u1})$
ϕ_v	$\triangleq 0.5\ (\phi_{v2} + \phi_{v1})$
$\Delta\phi_v$	$\triangleq 0.5\ (\phi_{v2} - \phi_{v1})$
Φ	rotation about the z'' axis
θ	rotation about the y' axis
Ψ	rotation about the x axis

(Fig. 12)

DEFINITIONS

Let x, y, z be the sphere coordinate system and X, Y, Z the room-fixed reference coordinate system. Figure 1 shows both systems coinciding. Another system, X_r, Y_r, Z_r, is parallel to X, Y, Z with the Z_r and the Z axes coinciding and the origin of X_r, Y_r, Z_r the distance h below the origin of the X, Y, Z system. The read circle is defined by the intersection of the X_r, Y_r plane (i.e., the read plane, Fig. 1) with the sphere. The intersection angles are read positively from X_r toward Y_r.

The axes of the superimposed coordinate system are labeled u, v, w. For zero rotation of the superimposed system, u coincides with X, v with Y, and w with Z. The angle between u and X, as well as between v and Y and w and Z, will not exceed $\pm \pi/2$.

For identification, the sphere half axes are assigned the following numbers:

+x = +1 +y = +2 +z = +3

-x = -1 -y = -2 -z = -3.

The half circles are also identified by numbers. Note that the magnitude of the half circle numbers is the same as the magnitude of the numbers for the axes perpendicular to the half circles. The following identifications were chosen (Fig. 1):

Axis pierce point through which half circle passes	Half circle identification
+x	+2
-x	-2
+y	+3
-y	-3
+z	+1
-z	-1

ATTITUDE DETERMINATION OF THE SUPERIMPOSED COORDINATE SYSTEM

The intersections of the great circles with the read circle (there may be four or six intersections, depending on the position of the sphere) are labeled ϕ_1, ϕ_2, etc., in the order in which they appear when the angle ϕ is increased from its reference X_r.

Any two intersections formed by the same great circle are considered a pair. Each pair will allow the calculation of the three direction cosines associated with the axis perpendicular to the great circle causing the intersections.

The first intersection pair defines the v axis and is called ϕ_{v1} and ϕ_{v2}. The second pair (ϕ_{u1} and ϕ_{u2}) defines the u axis. If there are six intersections, two are disregarded as explained in the next section.

The following quantities are calculated for the v axis:

$$\Delta\phi_v \triangleq 0.5\,(\phi_{v2} - \phi_{v1}) \qquad \phi_v \triangleq 0.5\,(\phi_{v2} + \phi_{v1})$$

$$\sin\alpha_v = \frac{\cos\Delta\phi_v}{+\sqrt{(h/r)^2 + \cos^2\Delta\phi_v}}$$

$$\cos\alpha_v = \frac{(h/r)}{+\sqrt{(h/r)^2 + \cos^2\Delta\phi_v}} \quad . \qquad (1)$$

This is illustrated in Figure 4.

Similarly for the u axis:

$$\Delta\phi_u \triangleq 0.5\,(\phi_{u2} - \phi_{u1}) \qquad \phi_u \triangleq 0.5\,(\phi_{u2} + \phi_{u1})$$

$$\sin\alpha_u = \frac{\cos\Delta\phi_u}{+\sqrt{(h/r)^2 + \cos^2\Delta\phi_u}}$$

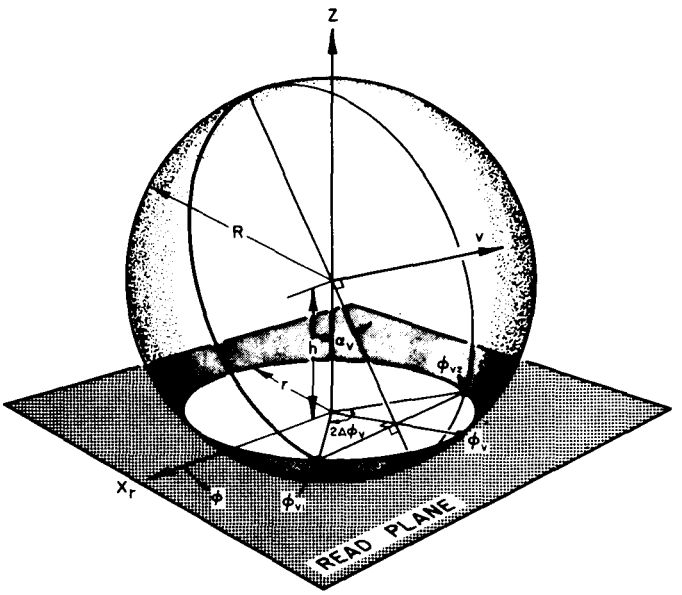

$\Delta\phi_v \triangleq \frac{1}{2}(\phi_{v2} - \phi_{v1})$

$\phi_v \triangleq \frac{1}{2}(\phi_{v2} + \phi_{v1})$

$$\sin\alpha_v = \frac{\cos\Delta\phi_v}{+\sqrt{\left(\frac{h}{r}\right)^2 + \cos^2\Delta\phi_v}}$$

$$\cos\alpha_v = \frac{\left(\frac{h}{r}\right)}{+\sqrt{\left(\frac{h}{r}\right)^2 + \cos^2\Delta\phi_v}}$$

FIGURE 4. ANGLE CALCULATIONS

$$\cos\alpha_u = \frac{(h/r)}{+\sqrt{(h/r)^2 + \cos^2\Delta\phi_u}} \quad . \qquad (2)$$

The orthogonal transformation matrix may be written now.

$$\begin{bmatrix} u \\ v \\ w \end{bmatrix} = \begin{bmatrix} a_{uX} & a_{uY} & a_{uZ} \\ a_{vX} & a_{vY} & a_{vZ} \\ a_{wX} & a_{wY} & a_{wZ} \end{bmatrix} \begin{bmatrix} X \\ Y \\ Z \end{bmatrix} \qquad (3)$$

with the values shown below.

$$a_{uX} = -\cos\alpha_u \cos\phi_u \qquad a_{vX} = \cos\alpha_v \cos\phi_v \qquad a_{wX} = a_{uY}a_{vZ} - a_{uZ}a_{vY}$$

$$a_{uY} = -\cos\alpha_u \sin\phi_u \qquad a_{vY} = \cos\alpha_v \sin\phi_v \qquad -a_{wY} = a_{uX}a_{vZ} - a_{uZ}a_{vX}$$

$$a_{uZ} = -\sin\alpha_u \qquad a_{vZ} = \sin\alpha_v \qquad a_{wZ} = a_{uX}a_{vY} - a_{uY}a_{vX}.$$

The difference in sign between the direction cosines for u and v is explained by the fact that the angle ϕ_v is the angle of the projection of the +v axis on the read plane, whereas ϕ_u is the angle of the -u axis projection.

As mentioned earlier, the orthogonal transformation matrix from the reference coordinate system to the superimposed coordinate system is found without recourse to any great circle split or identification other than proper pairing.

DETERMINATION OF THE COORDINATE SYSTEM CORRELATION

The superimposed coordinate system may have any one of 24 different superpositions with respect to the sphere coordinate system. The proper superposition is identified by combining two separate pieces of information. First, the absolute value of the half circle identification number indicates which axis is correlated. Second, the sign sequence of the half circle intersections indicates the sequence of the signs for the axes coinciding with u, v, w, respectively.

There are eight possible sign sequences for the four intersection case (Fig. 5). This can be seen in

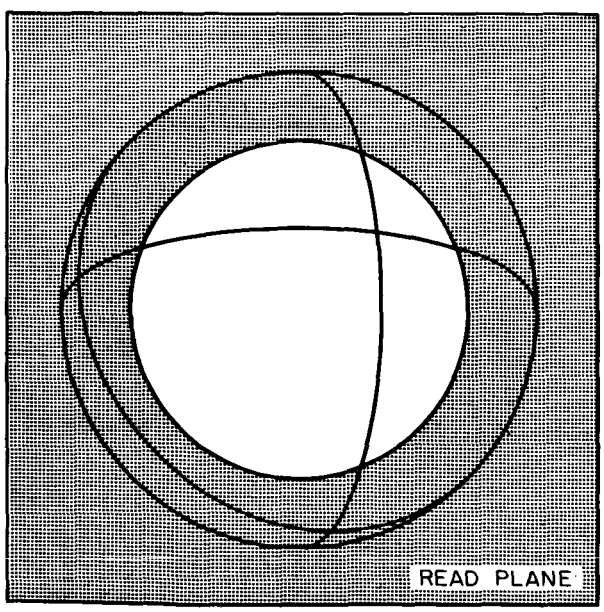

BOTTOM VIEW

FIGURE 5. FOUR INTERSECTION CASE

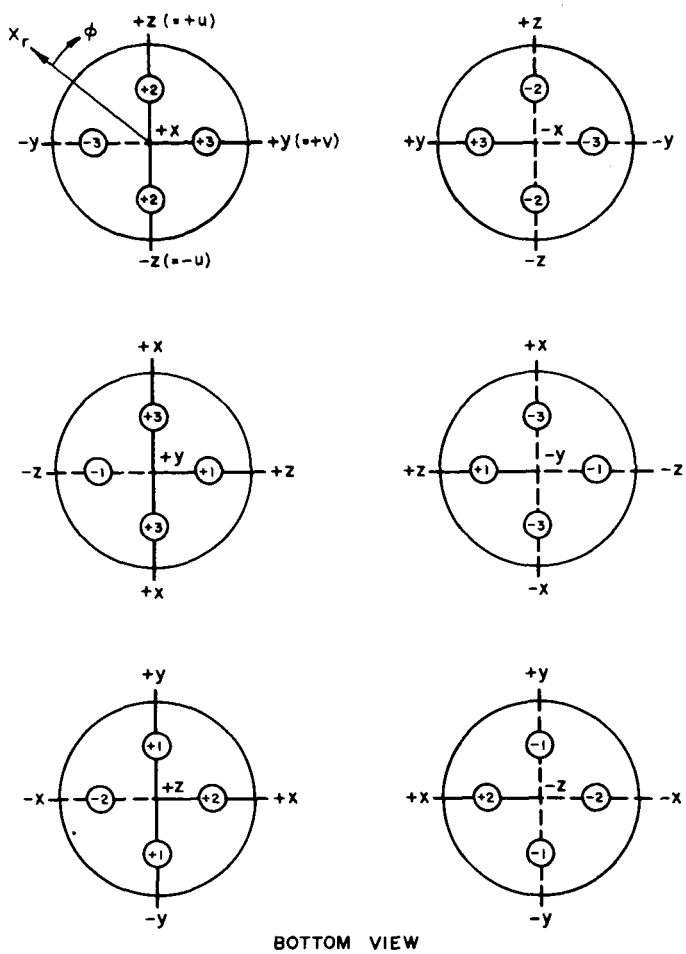

BOTTOM VIEW

FIGURE 6. POSSIBLE FOUR INTERSECTION CASES

Figure 6 by starting the sequence clockwise in each quadrant of the six circles shown. Each sign sequence appears three times with different number magnitudes. One of the three possibilities for the sequence +, +, +, - is used as an example. The eight sign sequences are shown in Table 1. For each of these sequences, there is a sign sequence for the axes coinciding with u, v, w. Labels L_{V1}, L_{V2}, etc., are the half circle identifications.

For the case of six half circle intersections, there are several subcases: zero, one, two, or three axis pierce points may be visible within the read circle (Figs. 7, 8, 9, and 10). These subcases will be called 6_0, 6_1, 6_2, and 6_3, respectively. Cases 6_0 and 6_3 are mutually exclusive, depending on whether the read circle radius is smaller or larger than $r' = R\sqrt{2/3}$, where r' is the radius of a circle touching three axis pierce points belonging to the same sphere octant.

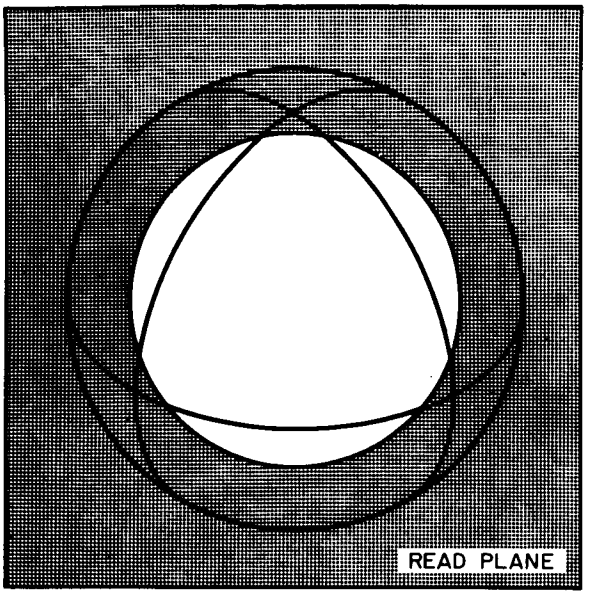

BOTTOM VIEW

$r < R\sqrt{\frac{2}{3}}$

FIGURE 7. SIX INTERSECTION CASE (NO AXIS PIERCE POINT IN READ CIRCLE)

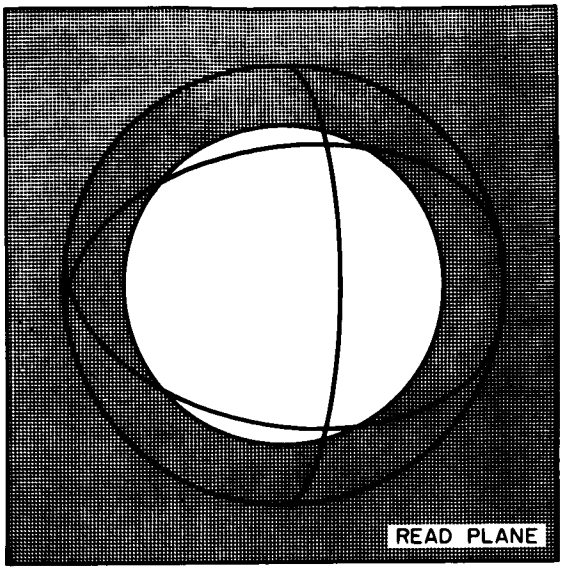

BOTTOM VIEW

FIGURE 9. SIX INTERSECTION CASE (TWO AXIS PIERCE POINTS IN READ CIRCLE)

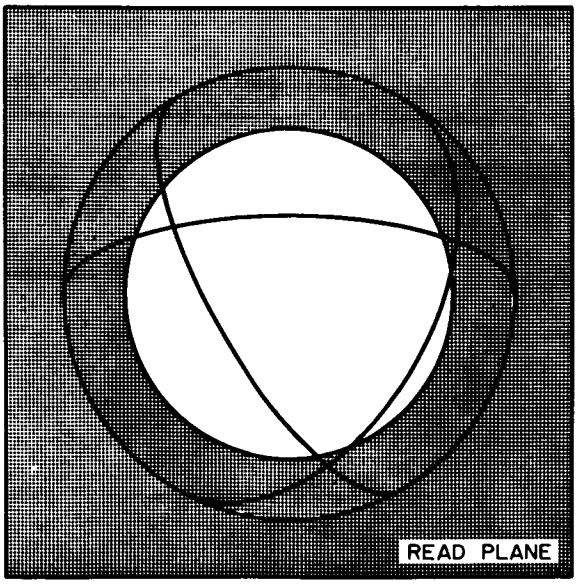

BOTTOM VIEW

FIGURE 8. SIX INTERSECTION CASE (ONE AXIS PIERCE POINT IN READ CIRCLE)

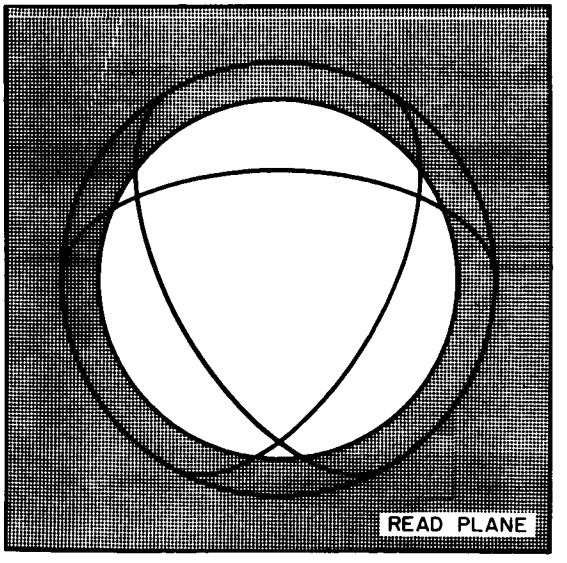

BOTTOM VIEW

$r > R\sqrt{\frac{2}{3}}$

FIGURE 10. SIX INTERSECTION CASE (THREE AXIS PIERCE POINTS IN READ CIRCLE)

TABLE 1. FOUR INTERSECTION CASE

sgn L_{v1}	sgn L_{u1}	sgn L_{v2}	sgn L_{u2}	v	u	w
+1	+1	+1	-1	+	+	-
+1	+1	-1	+1	-	+	-
+1	-1	+1	+1	-	-	-
-1	+1	+1	+1	+	-	-
-1	-1	-1	+1	-	+	+
-1	-1	+1	-1	-	-	+
-1	+1	-1	-1	+	-	+
+1	-1	-1	-1	+	+	+

TABLE 2. SIX INTERSECTION SUBCASE 6_0

sgn L_v	sgn L_u	sgn L_w	v	u	w
+1	+1	+1	-	+	-
+1	+1	-1	-	-	-
+1	-1	+1	+	+	-
-1	+1	+1	-	+	+
-1	-1	-1	+	-	+
-1	-1	+1	-	-	+
-1	+1	-1	+	-	-
+1	-1	-1	+	+	+

To determine the subcase by inspection of the half circle intersections, it should be remembered that they are labeled ϕ_1, ϕ_2, etc, as they appear. A pair (belonging to the same great circle) can be unseparated ($\phi_1\phi_2$, $\phi_2\phi_3$, . . . , $\phi_6\phi_1$), or separated by one ($\phi_1\phi_3$, $\phi_2\phi_4$, . . . , $\phi_6\phi_2$) or two ($\phi_1\phi_4$, $\phi_2\phi_5$, . . . , $\phi_6\phi_3$) intersections belonging to other pairs. These properties are used to determine the proper subcase.

Subcase 6_0 has three unseparated pairs (Fig. 7).

Subcase 6_1 has one unseparated pair and two single-separation pairs (Fig. 8).

Subcase 6_2 has two single-separation pairs and one double-separation pair (Fig. 9).

Subcase 6_3 has three double-separation pairs (Fig. 10).

For the matrix calculation, subcases 6_1, 6_2, and 6_3 are reduced to the four intersection case by disregarding two intersections. In 6_1 the unseparated pair is disregarded, in 6_2 the pair with the smallest $\Delta\phi$ is disregarded, and in 6_3 the third pair is disregarded.

Subcase 6_0 must be treated separately; Table 2 applies with $L_{v1} = L_{v2} = L_v$, etc. This is also illustrated in Figure 11.

Using the correlation between the superimposed coordinate system and the sphere coordinate system, the reference-system/sphere-system orthogonal transformation matrix may be established. This is done by writing a correlation matrix and multiplying it with the reference-system/superimposed-system matrix. Consider, for example, the following sequence of identification numbers:

$L_1 = +3$; $L_2 = +2$; $L_3 = -3$; $L_4 = +2$;

or after proper pairing,

$L_{v1} = +3$; $L_{v2} = -3$; $L_{u1} = +2$; $L_{u2} = +2$.

The second sign sequence in Table 1 applies, with the following result:

$v = -z \quad u = +y \quad w = -x$

and accordingly

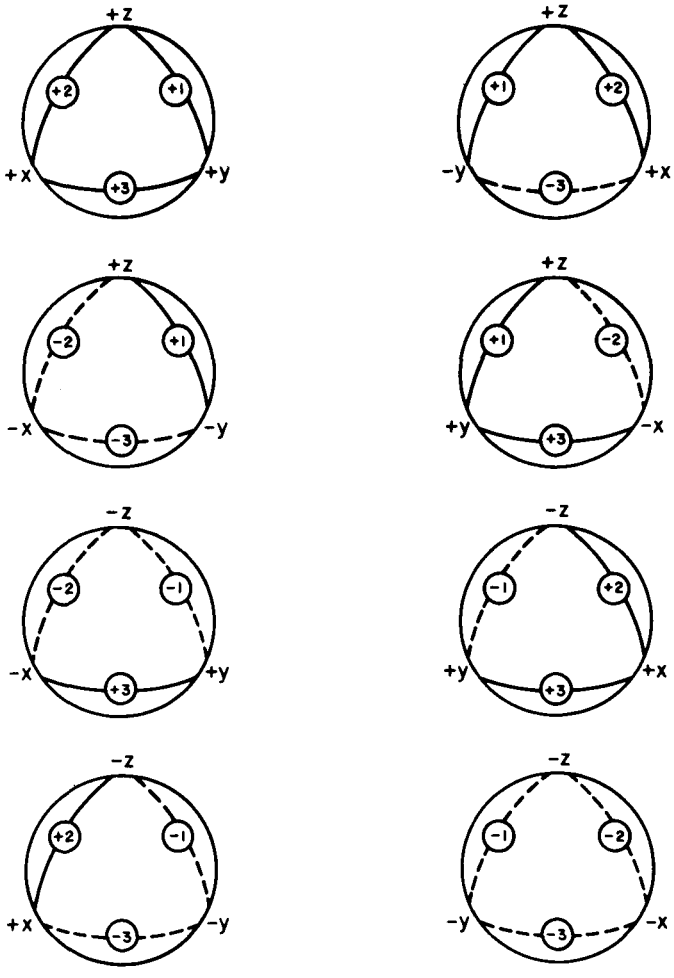

BOTTOM VIEW

FIGURE 11. POSSIBLE CONFIGURATIONS FOR CASE 6

$$\begin{bmatrix} x \\ y \\ z \end{bmatrix} = \begin{bmatrix} 0 & 0 & -1 \\ +1 & 0 & 0 \\ 0 & -1 & 0 \end{bmatrix} \begin{bmatrix} u \\ v \\ w \end{bmatrix}$$

$$\begin{bmatrix} x \\ y \\ z \end{bmatrix} = \begin{bmatrix} 0 & 0 & -1 \\ +1 & 0 & 0 \\ 0 & -1 & 0 \end{bmatrix} \begin{bmatrix} a_{uX} & a_{uY} & a_{uZ} \\ a_{vX} & a_{vY} & a_{vZ} \\ a_{wX} & a_{wY} & a_{wZ} \end{bmatrix} \begin{bmatrix} X \\ Y \\ Z \end{bmatrix}$$

$$\begin{bmatrix} x \\ y \\ z \end{bmatrix} = \begin{bmatrix} -a_{wX} & -a_{wY} & -a_{wZ} \\ a_{uX} & a_{uY} & a_{uZ} \\ -a_{vX} & -a_{vY} & -a_{vZ} \end{bmatrix} \begin{bmatrix} X \\ Y \\ Z \end{bmatrix}$$

DETERMINATION OF EULER ANGLES

In general, the orthogonal transformation matrix has the form:

$$\begin{bmatrix} x \\ y \\ z \end{bmatrix} = \begin{bmatrix} a_{xX} & a_{xY} & a_{xZ} \\ a_{yX} & a_{yY} & a_{yZ} \\ a_{zX} & a_{zY} & a_{zZ} \end{bmatrix} \begin{bmatrix} X \\ Y \\ Z \end{bmatrix} . \qquad (4)$$

Any order of rotation may be treated. The sphere axes are designated x", y", z" (identical with X, Y, Z) before rotation. The first rotation through the angle Φ, for example, is about the z" axis, resulting in x', y', z". The second rotation through the angle θ is about the axis y', resulting in x, y', z'. The third rotation through the angle Ψ is about the x axis, resulting in the final attitude x, y, z. This is illustrated in Figure 12 and expressed in matrix notation in equation 5. Multiplication of the individual rotation matrices gives the orthogonal transformation matrix expressed in equation 6.

$$\begin{bmatrix} x \\ y \\ z \end{bmatrix} = \begin{bmatrix} 1 & 0 & 0 \\ 0 & \cos\Psi & \sin\Psi \\ 0 & -\sin\Psi & \cos\Psi \end{bmatrix} \begin{bmatrix} \cos\theta & 0 & -\sin\theta \\ 0 & 1 & 0 \\ \sin\theta & 0 & \cos\theta \end{bmatrix} \begin{bmatrix} \cos\Phi & \sin\Phi & 0 \\ -\sin\Phi & \cos\Phi & 0 \\ 0 & 0 & 1 \end{bmatrix} \begin{bmatrix} X \\ Y \\ Z \end{bmatrix} \qquad (5)$$

$$\begin{bmatrix} x \\ y \\ z \end{bmatrix} = \begin{bmatrix} \cos\Phi\cos\theta & \sin\Phi\cos\theta & -\sin\theta \\ \cos\Phi\sin\theta\sin\Psi - \sin\Phi\cos\Psi & \sin\Phi\sin\theta\sin\Psi + \cos\Phi\cos\Psi & \cos\theta\sin\Psi \\ \cos\Phi\sin\theta\cos\Psi + \sin\Phi\sin\Psi & \sin\Phi\sin\theta\cos\Psi - \cos\Phi\sin\Psi & \cos\theta\cos\Psi \end{bmatrix} \begin{bmatrix} X \\ Y \\ Z \end{bmatrix} \qquad (6)$$

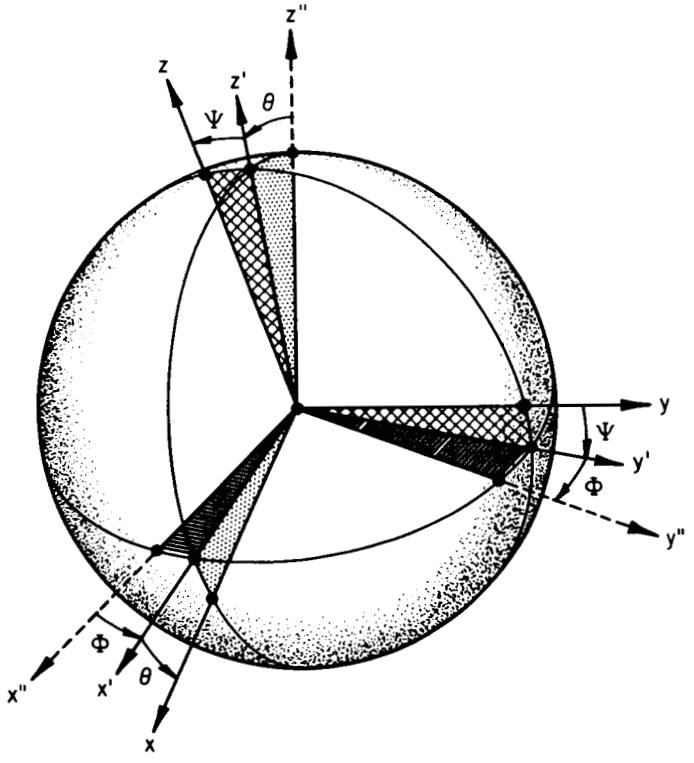

ORDER OF ROTATION
1. Φ CCW ABOUT z"-AXIS
2. θ CCW ABOUT y'-AXIS
3. Ψ CCW ABOUT x-AXIS

FIGURE 12. ROTATION ANGLES

Comparison of the direction cosines between equations 4 and 6 leads to

$\Phi = \arctan (a_{xY}/a_{xX})$

$\theta = \arcsin (-a_{xZ})$

$\Psi = \arctan (a_{yZ}/a_{zZ})$.

To make the solution single valued, the following limits must be imposed:

$-\pi \leq \Phi \leq +\pi$

$-\pi/2 \leq \theta \leq +\pi/2$

$-\pi \leq \Psi \leq +\pi$.

These limits force $\cos\theta \geq 0$ allowing the determination of the proper quadrant for Φ and Ψ by

$(\text{sgn } a_{xY})/(\text{sgn } a_{xX})$

and

$(\text{sgn } a_{yZ})/(\text{sgn } a_{zZ})$.

One sample was calculated and is presented in the appendix.

CONCLUSIONS

It appears that the mathematical solution presented can be implemented with reasonable cost while rendering adequate accuracy for the problems to be investigated on gas bearing supported simulation tables. An exact error analysis, however, to determine the accuracy of the attitude readout is left to a future study.

The orthogonal transformation matrices and the Euler angles can be calculated with standard digital computer equipment.

A method for the readout of the intersection angles must be devised and the necessary equipment developed and mechanized.

APPENDIX

DERIVATIONS OF CORRELATION FORMULAS

A. FOUR INTERSECTION CASE

The correlation information contained in Table 1 for the four intersection case may be condensed into a mathematical formulation. This is demonstrated for the axis coinciding with v. Two modifiers are introduced: $0.5\ (1 + \text{sgn}\ L_{v_1})$ and $0.5\ (1 - \text{sgn}\ L_{v_1})$. Each can only assume the value zero or +1. One is present when the other vanishes and vice versa, thus affording a selection. For sgn $L_{v_1} = +1$, we can see from Table 1 that sgn v = sgn L_{u_2}; and for sgn $L_{v_1} = -1$, sgn v = sgn L_{u_1}. The combination of the above statements with the modifiers and the absolute value of the label results in

$$v = -L_{v_1}\,[0.5\ (1 + \text{sgn}\ L_{v_1})\ \text{sgn}\ L_{u_2} + 0.5\ (1 - \text{sgn}\ L_{v_1})\ \text{sgn}\ L_{u_1}]\,.$$

Similarly the correlation for u is

$$u = L_{u_1}\,[0.5\ (1 + \text{sgn}\ L_{u_1})\ \text{sgn}\ L_{v_1} + 0.5\ (1 - \text{sgn}\ L_{u_1})\ \text{sgn}\ L_{v_2}]\,.$$

Axis w is correlated by the formula:

$$w = -0.25\,[12 - |L_{u_1}| - |L_{u_2}| - |L_{v_1}| - |L_{v_2}|\,]\ \Sigma\text{sgn}\ L$$

with $\Sigma\text{sgn}\ L = \text{sgn}\ L_{u_1} + \text{sgn}\ L_{u_2} + \text{sgn}\ L_{v_1} + \text{sgn}\ L_{v_2}$,

which can be explained as follows. The sum of the absolute values of all half circles is 12. For the four intersection case under discussion here, there are never more than four intersections showing. Therefore, subtracting the magnitude of the visible labels from 12 leaves twice the magnitude of the not-visible labels, which provides the magnitude of the axis with which w correlates. Summing the label signs determines whether w coincides with a plus or minus axis (compare Fig. 6).

B. SIX INTERSECTION CASE, SUBCASE 6_0

When six intersections between the half circles and the read circle occur and no axis pierce point is visible within the read circle (Fig. 7), the following formulas apply. These formulas were derived from Table 2, which summarizes the eight possible sign sequences. When sgn L_u is positive, multiplication by sgn L_w gives the proper sign for u. When sgn L_u is negative, it must be multiplied by sgn L_v and the resulting sign inverted. This is achieved by the formula:

$$u = -L_u\,[0.5\ (1 - \text{sgn}\ L_u)\ \text{sgn}\ L_v - 0.5\ (1 + \text{sgn}\ L_u)\ \text{sgn}\ L_w]\,.$$

Again two selective modifiers are used to cause the unwanted part of the equation to drop out. The equations for v and w are similar:

$$v = L_v\,[0.5\ (1 - \text{sgn}\ L_v)\ \text{sgn}\ L_w - 0.5\ (1 + \text{sgn}\ L_v)\ \text{sgn}\ L_u]$$

$$w = L_w\,[0.5\ (1 - \text{sgn}\ L_w)\ \text{sgn}\ L_u - 0.5\ (1 + \text{sgn}\ L_w)\ \text{sgn}\ L_v]\,.$$

SAMPLE CALCULATION

Assume four intersections ϕ_1 through ϕ_4 identified by the angles from the reference X_r and by the labels of the intersecting half circles.

$\phi_1 = 45.4°$ $\phi_2 = 61.0°$ $\phi_3 = 165.5°$ $\phi_4 = 301.1°$

$L_1 = -1$ $L_2 = +3$ $L_3 = +1$ $L_4 = +3$.

To find the direction cosines of the axes perpendicular to the intersecting great circles, the angles ϕ_v, $\Delta\phi_v$, ϕ_u, and $\Delta\phi_u$ must be identified.

$$\phi_v = 0.5\ (165.5 + 45.4) = 105.45°$$

$$\Delta\phi_v = 0.5\ (165.5 - 45.4) = 60.05°$$

$$\phi_u = 0.5\ (301.1 + 61.0) = 181.05°$$

$$\Delta\phi_u = 0.5\ (301.1 - 61.0) = 120.05°\,.$$

Then

$$\sin\phi_v = +0.96386$$

$$\cos\phi_v = -0.26640$$

$\sin \Delta\phi_v = +0.86646$

$\cos \Delta\phi_v = +0.49924$

$\sin \phi_u = -0.01832$

$\cos \phi_u = -0.99983$

$\sin \Delta\phi_u = +0.86559$

$\cos \Delta\phi_u = -0.50076$.

Substituting into equations 1 and 2 results in (with h/r = 1)

$\sin \alpha_v = +0.44667$ $\quad$ $\sin \alpha_u = -0.44776$

$\cos \alpha_v = +0.89470$ $\quad$ $\cos \alpha_u = +0.89416$

and allows the orthogonal transformation matrix of equation 3 to be written. Because the intersection angle values were derived graphically, the matrix is not precisely orthogonal.

$$\begin{bmatrix} u \\ v \\ w \end{bmatrix} = \begin{bmatrix} +0.89401 & +0.01638 & +0.44776 \\ -0.23835 & +0.86237 & +0.44667 \\ -0.37882 & +0.50605 & +0.77487 \end{bmatrix} \begin{bmatrix} X \\ Y \\ Z \end{bmatrix}.$$

The correlation between the superimposed and the sphere coordinate system is found from Table 1, fourth sequence, to be:

$u = -z \quad v = +x \quad w = -y.$

With this correlation, the above matrix can be transformed into the final orthogonal transformation matrix:

$$\begin{bmatrix} x \\ y \\ z \end{bmatrix} = \begin{bmatrix} -0.23835 & +0.86237 & +0.44667 \\ +0.37882 & -0.50605 & -0.77487 \\ -0.89401 & -0.01638 & -0.44776 \end{bmatrix} \begin{bmatrix} X \\ Y \\ Z \end{bmatrix}.$$

This results in

$\tan \Phi = +0.86237/-0.23835 = (+1/-1) \cdot 3.6181$

$\sin \theta = -0.44667$

$\tan \Psi = -0.77487/-0.44776 = (-1/-1) \cdot 1.7305.$

The sign relationship of the direction cosines indicates that the angle Φ is in the second quadrant and that the angle Ψ is in the third quadrant. The final result is $\Phi = +105°37'$, $\theta = -26°32'$, and $\Psi = -120°1'$.

C. DEVELOPMENT OF SQUEEZE FILM BEARINGS

by Peter H. Broussard, Jr., John Burch, and Emmett L. Martz

In the past, the term "gas bearing" has referred to bearings in which the load-carrying member is supported on a gas film resulting either from external pressurization or from the high-speed relative lateral motion of the bearing surfaces. In the bearing described in this article, the necessary gas pressure is obtained by vibrating one bearing surface in a normal direction at a high frequency, thus alternately squeezing and releasing the gas film between the surfaces. This bearing does not require either external gas supply or high-speed rotation.

The first part of the article describes the theoretical development of the squeeze bearing using Reynolds' equation. The second part describes the design of a working model in which a piezoelectric sleeve and end plates provide motion normal to the supported member at all points.

AUTHOR

INTRODUCTION

The most commonly used gas-lubricated bearings have been either hydrostatic or hydrodynamic. The theoretical solution of either follows from Reynolds' equation. For the hydrostatic type, no relative motion of the bearing surfaces is necessary, as a pressure gradient is maintained by external pressurization. For the hydrodynamic type, a pressure gradient is maintained by lateral, relative motion of the bearing surfaces. Also contained in Reynolds' equation is a term pertaining to the rate of change of the product of gap height and density with respect to time; this is the type of motion treated in this article. It is shown that a net load carrying capacity is generated by cyclic squeeze motion of two parallel surfaces.

According to Reference 1, the earliest mention of gas squeeze films seems to have been made in 1954. At least as early as 1960, the idea of utilizing gas squeeze film bearings in the gyro field occurred to Dr. B. Sternlicht of Mechanical Technology, Inc. Astrionics Laboratory commenced work in squeeze films in November 1963, after having become aware of the work reported in Reference 1.

NOMENCLATURE

R_1	inner radii of annuli
R_2	outer radii of annuli
r	radial coordinate
θ	angular coordinate
h_o	mean gap height
h	instantaneous gap height
Δh	peak amplitude of excursion
p	pressure
ρ	density
μ	viscosity
t	time
ω	frequency
T	absolute temperature
R_c	gas constant
p_a	ambient pressure

ANALYSIS

Consider two parallel flat annuli as shown in Figure 1, the top annulus to be fixed and the bottom annulus to be capable of executing vertical cyclic motion. Let the inner and outer radii of the annuli be R_1 and R_2, respectively. Denote the instantaneous gap height between the annuli by h and let the bottom annulus execute a sinusoidal motion (Fig. 2) such that the instantaneous gap height is given by

$$h = h_o - \Delta h \cos \omega t$$

or, if made dimensionless by division of h_o,

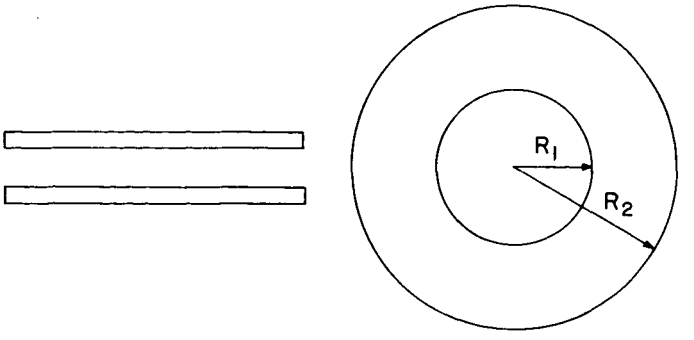

FIGURE 1. PARALLEL FLAT ANNULI

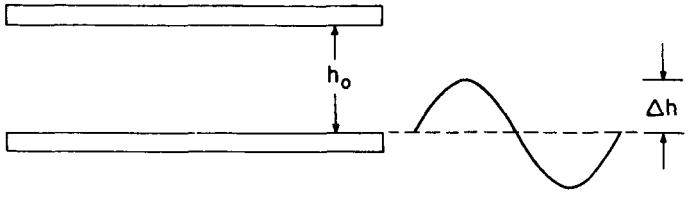

FIGURE 2. BOTTOM ANNULUS IN SINUSOIDAL MOTION

$$H = \frac{h}{h_o} = 1 - \epsilon \cos \omega t$$

where $\epsilon = \frac{\Delta h}{h_o}$

h_o = mean gap height.

The dynamic behavior of the gas is described by Reynolds' equation in cylindrical coordinates:

$$\frac{1}{r}\frac{\partial}{\partial r}\left[r\,\frac{h^3}{12\mu}\,\rho\,\frac{\partial p}{\partial r}\right] = \frac{\partial(\rho h)}{\partial t} \qquad (1)$$

where r = radial coordinate

h = gap height

p = pressure

ρ = density

μ = viscosity

t = time.

This equation can be made dimensionless by letting

$$P = \frac{p}{p_a},\ R = \frac{r}{R_2 - R_1},\ H = \frac{h}{h_o},\ \tau = \omega t,\ \omega = \text{frequency}$$

where p_a = ambient pressure

and by assuming that the process is isothermal:

$$\rho = \frac{p}{R_c T},\ R_c = \text{gas constant},\ T = \text{absolute temperature.}$$

Substituting into equation 1 and noting that

$$\frac{\partial}{\partial r} = \frac{1}{R_2 - R_1}\,\frac{\partial}{\partial R} \text{ and } \frac{\partial}{\partial t} = \omega\,\frac{\partial}{\partial \tau}$$

equation 1 becomes

$$\frac{1}{R}\,\frac{\partial}{\partial R}\left[RH^3\,P\,\frac{\partial P}{\partial R}\right] = \sigma\,\frac{\partial(PH)}{\partial \tau}, \qquad (2)$$

where σ = squeeze number = $\dfrac{12\mu\omega(R_2 - R_1)^2}{p_a h_o^2}$.

For a specified motion of the bottom plate, $H = H(\tau)$, the pressure P can be found as a function of R and τ in theory. Practically, however, equation 2 cannot be solved in closed form and recourse must be made to solution either by numerical methods or by perturbation techniques, either one of which is relatively lengthy.

Fortunately, an approximate method exists (Refs. 1 and 2) that has given excellent agreement with experiment where the squeeze number σ approaches infinity (100 or more). As can be seen from the definition of σ, this can happen in several different ways, but the cases in which either $\omega \to \infty$ or $h_o \to 0$ are appropriate here.

Let both sides of equation 2 be integrated with respect to τ over one cycle, 2π:

$$\int_0^{2\pi} \frac{1}{R}\,\frac{\partial}{\partial R}\left[RH^3P\,\frac{\partial P}{\partial R}\right] d\tau = \sigma \int_0^{2\pi} \frac{\partial(PH)}{\partial \tau}\, d\tau$$

$$= 0, \qquad (3)$$

since PH is periodic of period 2π. Thus

$$\int_0^{2\pi} \frac{1}{R} \frac{\partial}{\partial R} \left[RH^3 P \frac{\partial P}{\partial R} \right] d\tau = 0$$

$$\text{or } \int_0^{2\pi} \frac{\partial}{\partial R} \left[RH^3 P \frac{\partial P}{\partial R} \right] d\tau = 0.$$

Interchanging the order of integration and differentiation,

$$\frac{\partial}{\partial R} \int_0^{2\pi} \left[RH^3 P \frac{\partial P}{\partial R} \right] d\tau = 0$$

and integrating

$$\int_0^{2\pi} \left[RH^3 P \frac{\partial P}{\partial R} \right] d\tau = C$$

or, since R is not a function of τ,

$$\int_0^{2\pi} \left[H^3 P \frac{\partial P}{\partial R} \right] d\tau = \frac{C}{R} . \qquad (4)$$

Since H is not a function of R, the integrand can be written as

$$\frac{1}{2} \frac{\partial}{\partial R} (H^3 P^2) ,$$

equation 4 can be written as

$$\int_0^{2\pi} \left[\frac{\partial}{\partial R} H^3 P^2 \right] d\tau = \frac{C_1}{R} ,$$

and, interchanging the order of integration and differentiation,

$$\frac{\partial}{\partial R} \int_0^{2\pi} \left[H^3 P^2 \right] d\tau = \frac{C_1}{R} .$$

Integrating,

$$\int_0^{2\pi} \left[H^3 P^2 \right] d\tau = C_1 \ln R + C_2 . \qquad (5)$$

Applying the boundary conditions $P = 1$ at $R = \frac{R_1}{R_2 - R_1}$ and $P = 1$ at $R = \frac{R_2}{R_2 - R_1}$ gives two equations:

$$\int_0^{2\pi} H^3 \, d\tau = C_1 \ln \frac{R_1}{R_2 - R_1} + C_2$$

$$\int_0^{2\pi} H^3 \, d\tau = C_1 \ln \frac{R_2}{R_2 - R_1} + C_2 .$$

These two equations imply that $C_1 = 0$. Thus

$$C_2 = \int_0^{2\pi} H^3 \, d\tau = \int_0^{2\pi} (1 - \epsilon \cos \tau)^3 \, d\tau$$

or $C_2 = 2\pi (1 + 3/2 \, \epsilon^2)$.

Therefore, from equation 5,

$$\int_0^{2\pi} H^3 P^2 \, d\tau = 2\pi (1 + 3/2 \, \epsilon^2). \qquad (6)$$

Equation 6 is used now for the case in which the squeeze number σ is very large, i.e., $\sigma \to \infty$. From equation 2, if $\sigma \to \infty$, then

$$\frac{\partial (PH)}{\partial \tau} = 0$$

or, integrating,

$$PH = f(r). \qquad (7)$$

where f(r) is to be determined. The fact that PH is a function of r is explained as follows: H can be a function only of τ, since the plates are parallel. P is a function of H, τ, and r. P is not a function of angular position on the annulus θ, since there is no circumferential variation in pressure. Therefore, P can depend only on H, τ, and r. This means that the product PH can be a function of, at most, two variables, r and τ. If

$$\frac{\partial (PH)}{\partial \tau} = 0,$$

then it follows that PH is a function of, at most, one variable, r. Substituting equation 7 into equation 6 gives

$$\int_0^{2\pi} H^3 P^2 \, d\tau = \int_0^{2\pi} H (PH)^2 \, d\tau$$

$$= \int_0^{2\pi} f(r)^2 H \, d\tau = f(r)^2 \int_0^{2\pi} (1 - \epsilon \cos \tau) \, d\tau$$

$$= 2\pi f(r)^2 .$$

That is,

$$\int_0^{2\pi} H^3 P^2 \, d\tau = 2\pi f(r)^2 \quad . \tag{8}$$

Equations 6 and 8 together imply that

$$2\pi f(r)^2 = 2\pi (1 + 3/2\ \epsilon^2)$$

or

$$f(r) = (1 + 3/2\ \epsilon^2)^{\frac{1}{2}} \quad . \tag{9}$$

Using equation 9 in equation 7 gives

$$P = \frac{f(r)}{H} = \frac{(1 + 3/2\ \epsilon^2)^{\frac{1}{2}}}{1 - \epsilon \cos \omega t} \tag{10}$$

or in dimensional form,

$$p = \frac{p_a (1 + 3/2\ \epsilon^2)^{\frac{1}{2}}}{1 - \epsilon \cos \omega t} \quad . \tag{11}$$

Equation 11 shows that p is a function of time but not of R.* The plot of p versus time is shown in Figure 3 for $\epsilon = 0.5$.

As can be seen from the plot, the average pressure in the gap is higher than ambient pressure. This means that there is a net force. The force F caused by the pressure in the gap is given by

$$F = \int_{R_1}^{R_2} 2\pi r p \, dr = 2\pi p_a \frac{(1 + 3/2\ \epsilon^2)}{1 - \epsilon \cos \omega t} \int_{R_1}^{R_2} r \, dr$$

or

$$F = \frac{\pi \left(R_2^2 - R_1^2\right) p_a (1 + 3/2\ \epsilon^2)^{\frac{1}{2}}}{1 - \epsilon \cos \omega t} \quad . \tag{12}$$

* It has been pointed out that this pressure distribution fails to meet the boundary conditions at the edges, $p = p_{am}$.

$$p = \frac{p_a (1 + 3/2\epsilon^2)^{1/2}}{1 - \epsilon \cos \omega t}, \quad \epsilon = 0.5$$

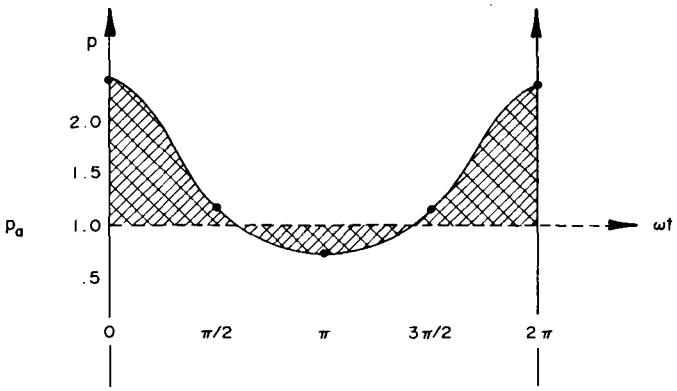

FIGURE 3. VARIATION OF PRESSURE WITH TIME, $\epsilon = 0.5$

The average force over one cycle is given by

$$\bar{F} = \frac{1}{2\pi} \int_0^{2\pi} F \, d\tau = \pi \left(R_2^2 - R_1^2\right) p_a (1 + 3/2\ \epsilon^2)^{\frac{1}{2}}$$

$$\frac{1}{2\pi} \int_0^{2\pi} \frac{d\tau}{1 - \epsilon \cos \tau}$$

or

$$F = \pi \left(R_2^2 - R_1^2\right) p_a \left(\frac{1 + 3/2\ \epsilon^2}{1 - \epsilon^2}\right)^{\frac{1}{2}} \tag{13}$$

since

$$\int_0^{2\pi} \frac{d\tau}{1 - \epsilon \cos \tau} = \frac{2\pi}{(1 - \epsilon^2)^{\frac{1}{2}}} \quad .$$

Equation 13 shows that the average force F is proportional to the ambient pressure, p_a. Hence, for a fixed ϵ, the average force can be increased by raising the ambient pressure in which the squeeze bearing operates. Figure 4 shows a load displacement curve which is applicable to either a disc or an annulus of the same area.

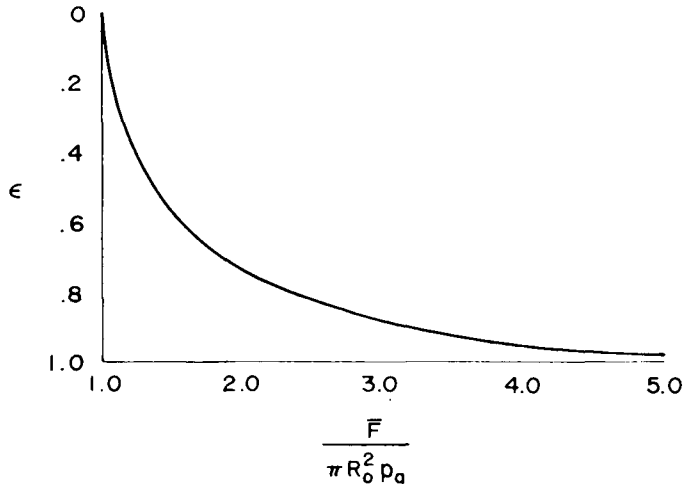

FIGURE 4. AVERAGE LOAD CARRYING CAPACITY VS ECCENTRICITY RATIO

JOURNAL SQUEEZE FILM BEARING

The expression for the force developed by the squeeze film can be used to determine the load carrying capacity of the journal bearing when certain assumptions are made.

In Figure 5, the inner cylinder is subjected to a constant radial force W. If a squeeze film force of sufficient magnitude is being generated, the inner cylinder will be displaced an average distance d from its concentric position relative to the sleeve and will float in this position. The system is in equilibrium; that is, the squeeze film force is exactly equal to the applied force W.

Assume that instead of being circular, the inner cylinder and journal are right cylindrical polygons having N sides each. This assumption will not introduce any appreciable error provided N is sufficiently large. Also, assume that the sleeve is subjected to a sinusoidal vibration and that the vibrating frequency is sufficiently large to give a squeeze number of 100 or more. There are two possible means of vibrating the sleeve relative to the inner cylinder; each will be treated separately.

1. The case of the sleeve vibrating in the direction of the applied force W will be considered first. The sleeve does not change size; that is, it does not expand and contract. The squeeze film force is generated over N separate pads. Now, the component of

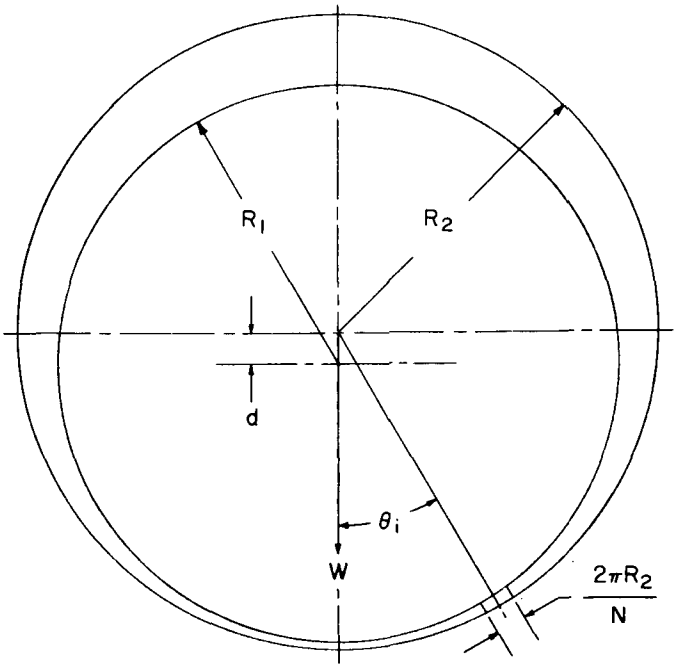

FIGURE 5. JOURNAL BEARING DISPLACEMENT GEOMETRY

the squeeze film force in the direction of the applied force W that is generated over the i^{th} pad will be determined.

The gap height at the i^{th} pad is given by

$$h = h_j (1 - \epsilon \cos \theta_i)$$

where h = the gap height at the i^{th} pad

h_j = the radial clearance = $R_2 - R_1$

ϵ = the eccentricity of the inner cylinder = $\frac{d}{R_2 - R_1}$

θ_i = the angular position of the i^{th} gap.

Since the gap height at any pad is considered constant across the pad, the expression developed for the thrust bearing to the journal bearing can be applied, remembering that only the component of the squeeze film force in the direction of the applied force W is of interest.

Therefore, the force generated over the i^{th} pad in the direction of the applied force W is given by

$$W_i = p_{am} A \left\{ \frac{1 + \frac{3}{2}\left[\frac{\Delta h \cos\theta_i}{h_j(1 - \epsilon\cos\theta_i)}\right]^2}{1 - \left[\frac{\Delta h \cos\theta_i}{h_j(1 - \epsilon\cos\theta_i)}\right]^2} \right\} \cos\theta_i$$

where W_i = the squeeze film force generated over the i^{th} pad in the direction of the applied force W

p_{am} = ambient pressure

A = the area of the i^{th} pad = $\frac{2\pi R_1 L}{N}$ where

L = the length of the inner cylinder

Δh = the amplitude of vibration.

Therefore, the total force generated over the entire sleeve in the direction of the applied force W is given in equation 14.

2. The second means of vibration is given by the sleeve expanding and contracting sinusoidally with respect to time. This mode of vibration would be given by using a piezoelectric sleeve. In this mode of vibration, for all practical purposes, the sleeve is moving normal to the inner cylinder at all points around the inner cylinder. For this mode of vibration, the total load carrying capacity of the journal bearing is given in equation 15.

Computer runs were made to determine the load carrying capacity of the journal bearing using both modes of vibration. Separate runs were made for both the AB-5 and AB-3 bearings to determine the effect of varying bearing clearances and amplitude of vibration. The results are plotted in Figures 6, 7, 8, and 9.

$$W = \frac{2\pi R_1 L P_{am}}{N} \sum_{i=1}^{i=N} \left\{ \frac{2h_j^2(1 - \epsilon\cos\theta_i)^2 + 3\Delta h^2\cos^2\theta_i}{2\left[h_j^2(1 - \epsilon\cos\theta_i)^2 - \Delta h^2\cos^2\theta_i\right]} \right\}^{\frac{1}{2}} \cos\theta_i \,. \qquad (14)$$

$$W = \frac{2\pi R_1 L P_{am}}{N} \sum_{i=1}^{i=N} \left\{ \frac{2h_j^2(1 - \epsilon\cos\theta_i)^2 + 3\Delta h^2}{2\left[h_j^2(1 - \epsilon\cos\theta_i)^2 - \Delta h^2\right]} \right\}^{\frac{1}{2}} \cos\theta_i \,. \qquad (15)$$

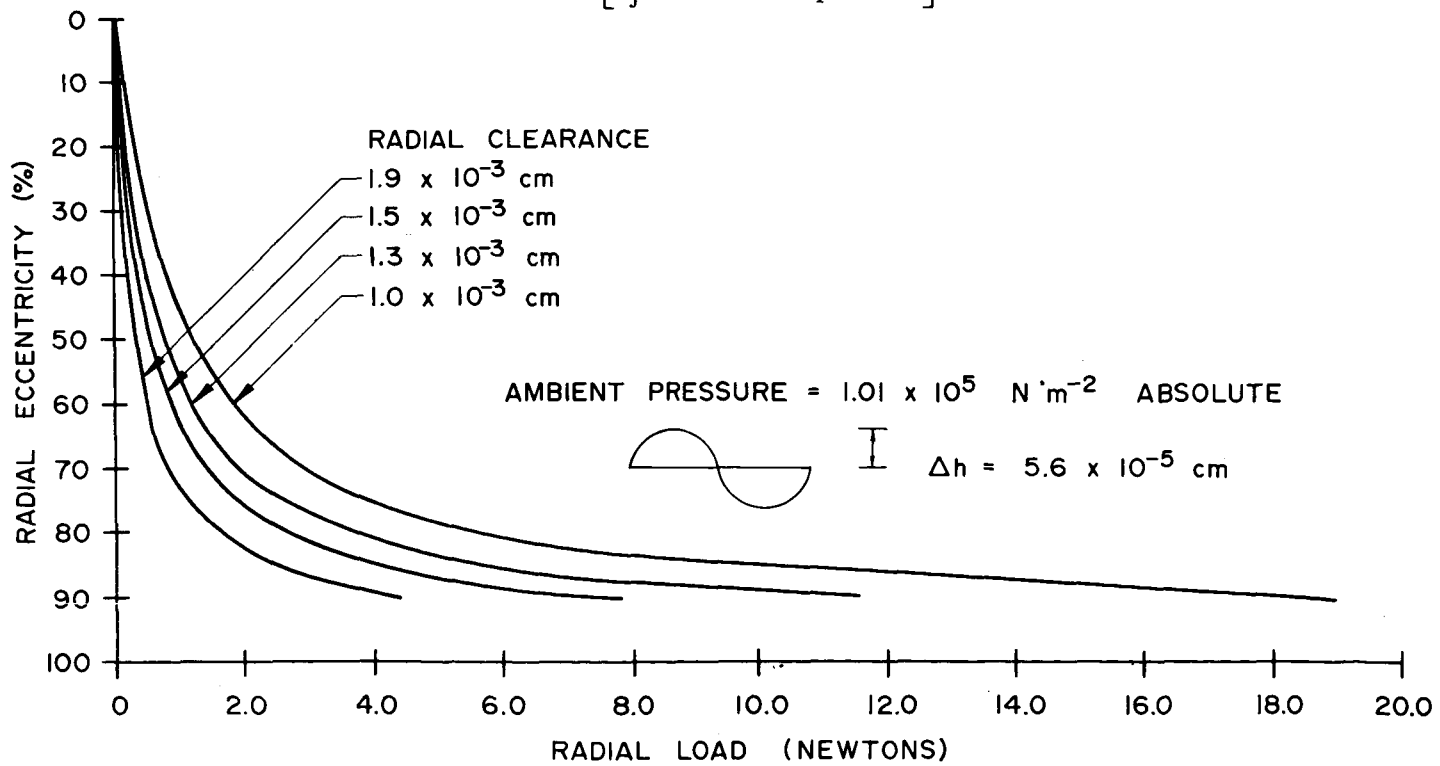

FIGURE 6. RADIAL ECCENTRICITY VS LOAD, AB-3 JOURNAL SQUEEZE FILM BEARING (PIEZOELECTRIC SLEEVE)

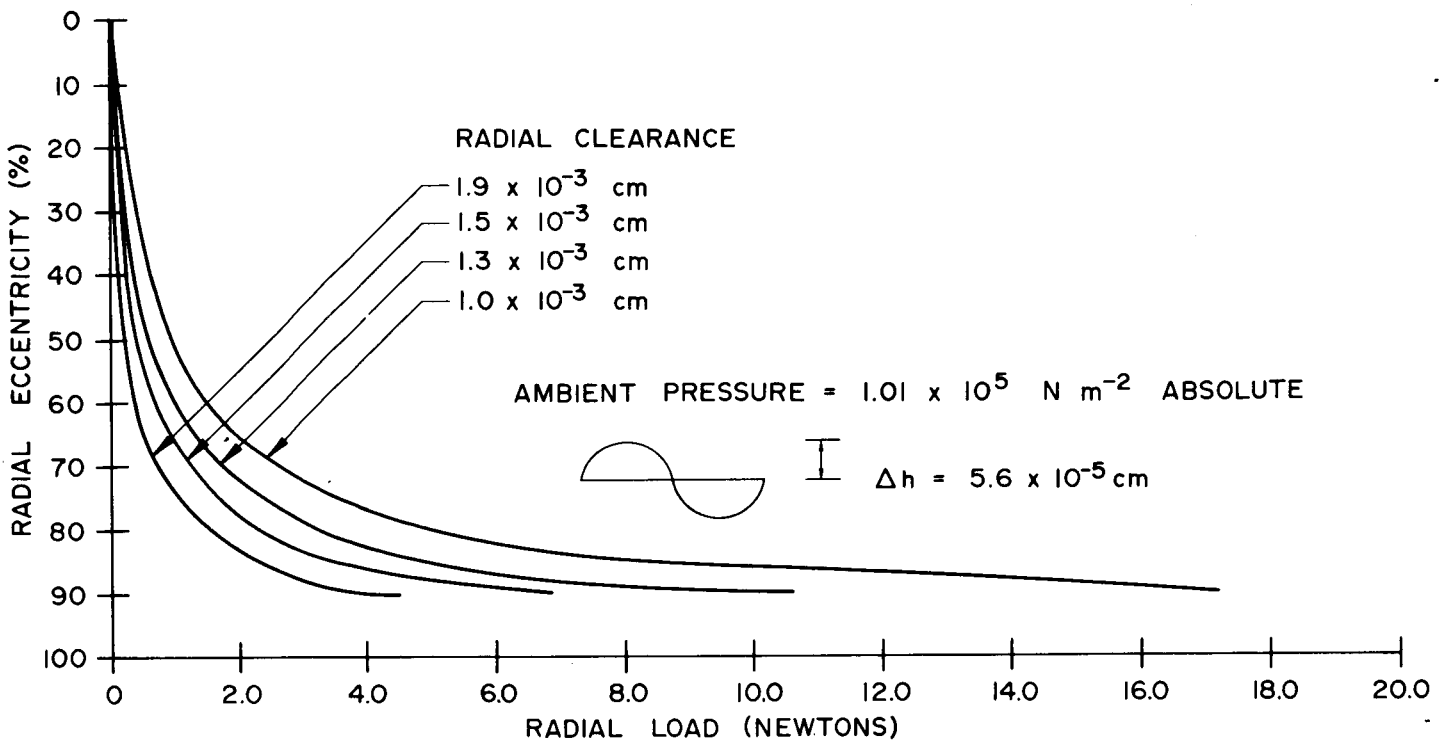

FIGURE 7. RADIAL ECCENTRICITY VS LOAD, AB–3 JOURNAL SQUEEZE FILM BEARING (UNIDIRECTIONAL SLEEVE MOVEMENT AS WOULD BE OBTAINED ON A SHAKE TABLE)

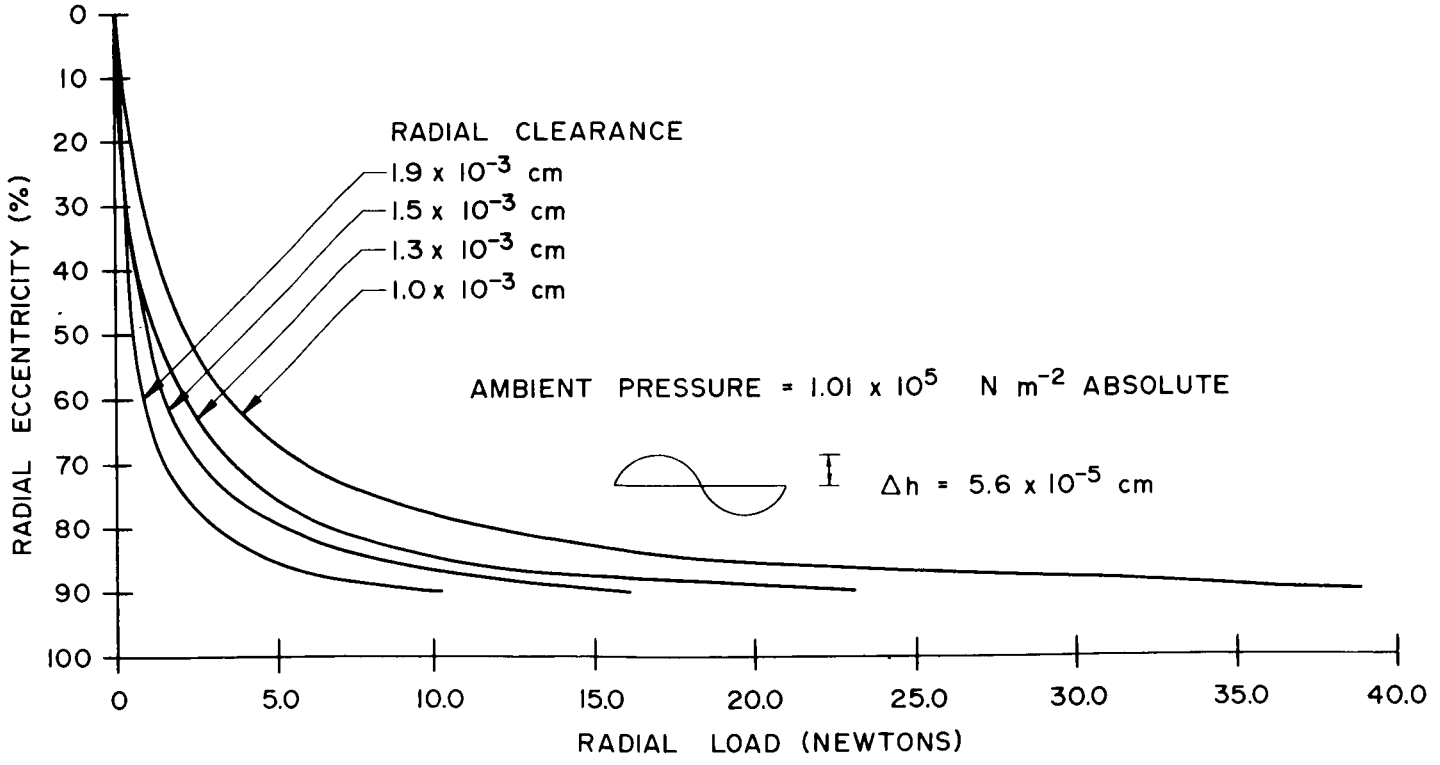

FIGURE 8. RADIAL ECCENTRICITY VS LOAD, AB–5 JOURNAL SQUEEZE FILM BEARING (UNIDIRECTIONAL SLEEVE MOVEMENT AS WOULD BE OBTAINED ON A SHAKE TABLE)

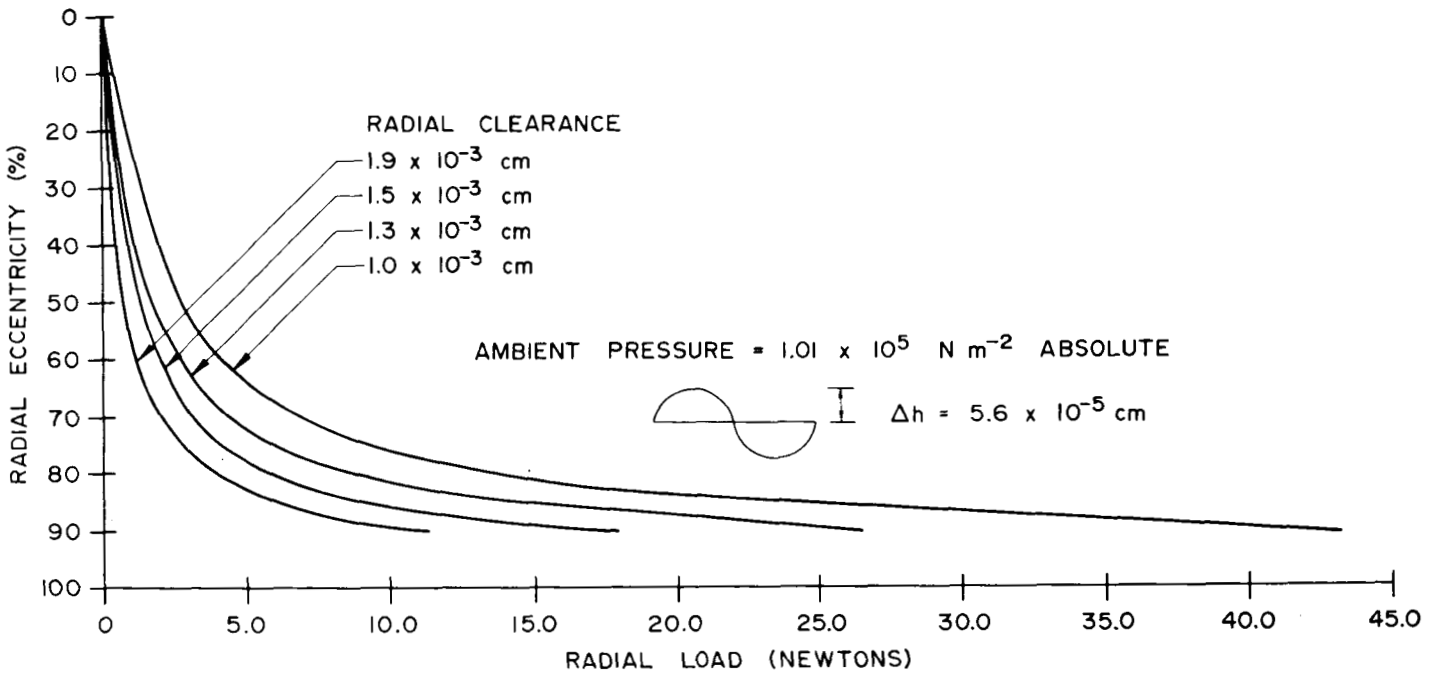

FIGURE 9. RADIAL ECCENTRICITY VS. LOAD, AB-5 JOURNAL SQUEEZE FILM BEARING (PIEZOELECTRIC SLEEVE)

A standard AB-3 assembly was vibrated on the shake table in an effort to compare theory with experiment for this mode of vibration (no piezoelectric sleeves were available at the time). Several factors such as resonance effects, cocking of the inner cylinder, inadequate means of loading, etc., made it impossible to accurately check theory against experiment for this mode of vibration. It was found that a sufficient squeeze film force was generated to float the inner cylinder for an applied radial force equivalent to 1 g acceleration.

EXPERIMENTAL

A. Squeeze Film Generator. After checking the theory of the squeeze film bearing and proving that it works by tests on the shake table, the next step has been the development of self-energized experimental models. Three types of power were considered:

1. Voice coil
2. Magnetostrictive
3. Piezoelectric

Requirements of minimum size, weight, power, magnetic field, and self-heating have made the piezoelectric ceramic transducer our choice for this application.

The ceramic is composed of a multitude of crystals, originally in random orientation. Its properties are the sum of the properties of all these crystallites. The ceramic is then poled by a strong dc field, whereby a majority of dipoles of the component crystals are aligned. After poling, if any electric field opposite in sense to the aligned dipoles is applied at higher and higher voltage, the dipoles of some crystals reverse their direction. To do this, the ions that form the dipole suddenly shift position slightly and a net expansion or contraction of the ceramic takes place. A rapidly changing electric field causes an in-phase changing of physical dimensions of the ceramic. Conversely, a rapid squeezing of the ceramic produces an in-phase changing in the polarity of the ceramic. This motor-generator property of the poled ceramic is known as piezoelectricity.

B. There are several problems associated with the use of piezoelectric ceramic. Some of these are:

1. Elliptical Radial Airgap. Tests conducted at MSFC with capacitive and photonic probes have

shown that when a piezoelectric ceramic sleeve is energized by an alternating current across curvilinear electrodes the radial excursion is 2.5 times as much at the center as near the ends. This asymmetric motion generates an elliptical radial airgap.

2. Resonant Frequency. By exciting the ceramic at its natural mechanical resonant frequency, the excursion can be amplified as much as 500 times. Resonance of a ceramic sleeve of equal length and diameter is about 1.6 times higher in frequency in the axial than in the radial direction. Although the resonant frequencies can be changed by changing the dimensions, simultaneous axial and radial resonance cannot be obtained.

3. Power and Heating. Power is limited by the physical strength of the ceramic and by the limit to which the material may be electrically driven before de-poling begins. In a squeeze film bearing, the power may also be limited by internal heating, which is a partial function of frequency.

4. Aging. The parameters of ferroelectric ceramics change with time after major disturbances such as temporary heating to high temperatures for electroding or the poling process. A reverse trend sets in after poling and is usually described as "aging per decade." The aging process is a logarithmic function of time but can be speeded up by exposure to radiation.

5. Electrodes. Electrodes should be good conductors, should not peel, and should be resistant to wear and corrosion. Electrolysis nickel plating, 50 to 75 μ thick, meets these requirements if the ceramic surface is carefully prepared in advance.

6. Attachment of Endplates. Endplates can be mounted either rigidly or flexibly to the ceramic sleeve. Rigidly mounted endplates have the same excursion and frequency as the sleeve-plus-endplate mass combination. This resonant frequency is slightly less than for the sleeve alone. Flexibly mounted endplates can be "tuned" to have an excursion much larger than the sleeve and to resonate at a lower frequency.

C. Conventional Test Models. There are several ways to design the ceramic transducers to float the conventional right inner cylinder. Three of these methods are described.

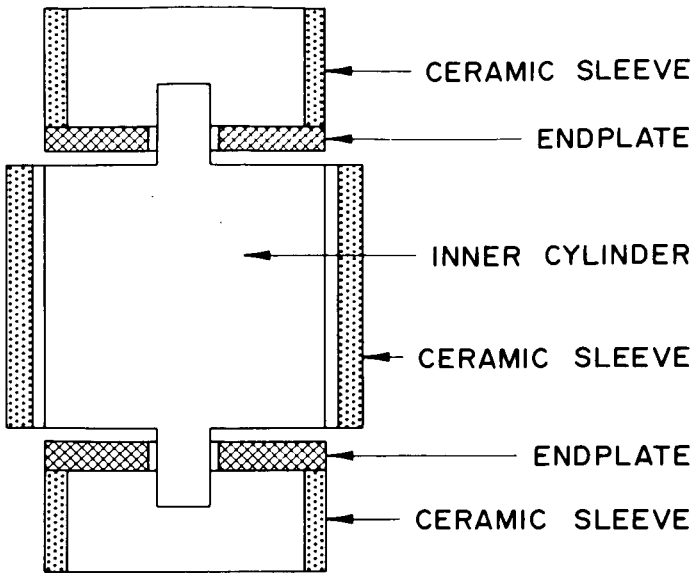

FIGURE 10. THREE TRANSDUCER SQUEEZE FILM BEARING

1. Three-Transducer Model (Fig. 10). This model has not been built. Its advantages are that maximum excursion can be maintained in the radial direction and a smaller excursion, proportional to sleeve length, can be maintained in the axial direction with all three ceramic sleeves operating at their individual resonant frequencies. A large amount of heat is generated but heat transfer is good. Disadvantages are the large size, alignment problems, and power required for three piezoelectric ceramic sleeves.

2. Two-Transducer Model (Fig. 11). This model was built and tested at MSFC. Its advantages are that maximum excursion can be maintained in both axial and radial directions. The axial airgap is generated by the endplates attached to the outer ceramic

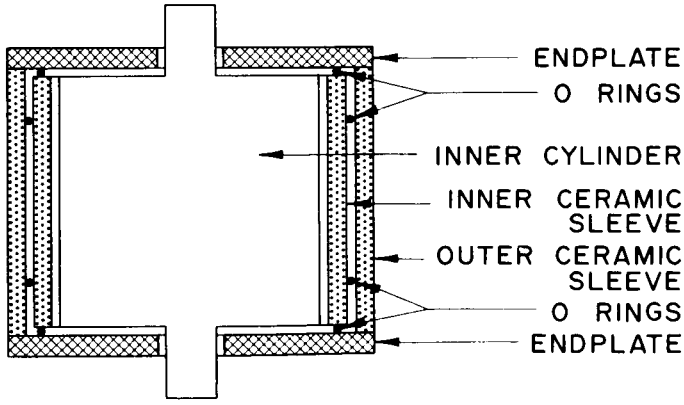

FIGURE 11. TWO TRANSDUCER SQUEEZE FILM BEARING

sleeve; the radial airgap is generated by the inner sleeve. Both sleeves are operated at their individual resonant frequencies. The two sleeves can be separated by O rings (as shown), by foamed metal, or even by gas if the two ceramic surfaces are lapped to close dimensional tolerances. The ability of a ceramic sleeve to support itself and an inner cylinder was demonstrated by Mechanical Technology, Inc. Disadvantages of this model are alignment problems, power required for two piezoelectric ceramic sleeves, and the relatively poor heat transfer.

3. One-Transducer Model (Fig. 12). This model was built and tested at MSFC. Its advantages are that maximum excursion in both axial and radial directions is obtained with only one ceramic sleeve. This is done by exciting the piezoelectric ceramic sleeve at resonant frequency in the radial direction and amplifying the smaller axial excursion by means of "tuned" endplates, held by flexible mounts. The

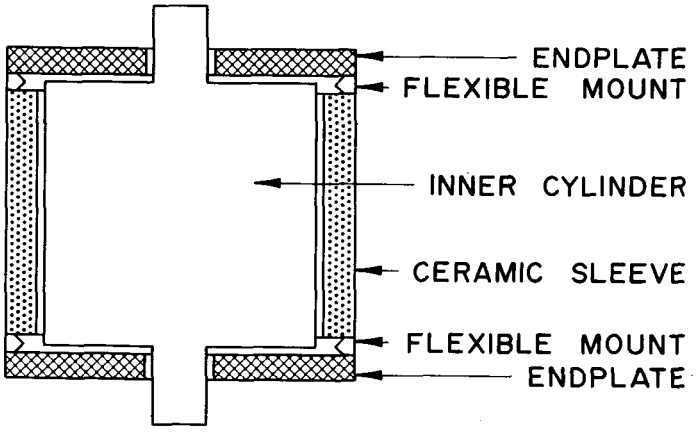

FIGURE 12. ONE TRANSDUCER SQUEEZE FILM BEARING

power required and heat generated are less for this model than for the other two. The disadvantage of this model is the added complexity of making the flexible mounts and maintaining them at the correct tension.

4. Other Configurations. The models shown in Figures 13 and 14 were built and tested at MSFC. Their purpose was to demonstrate the feasibility of spherical and conical shapes for squeeze film bearings. Components of both bearings were held together by epoxy.

a. The cup and ball used in our first spherical squeeze film bearing came from existing gas bearing parts. The ball weighs 1.81 kg and is 7.62 cm

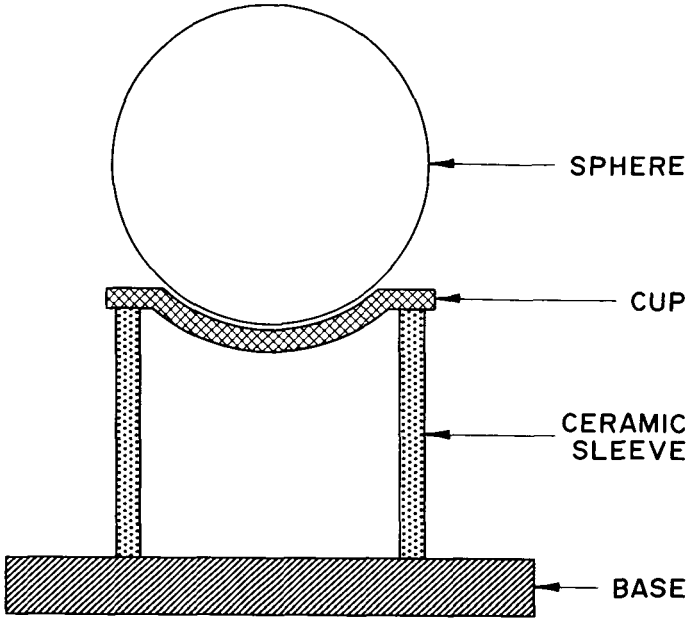

FIGURE 13. SPHERICAL SQUEEZE FILM BEARING

in diameter. A flat groove was cut on the under side of the cup so that it could be cemented to a ceramic sleeve. The sleeve measures 7.62 cm in length and inside diameter and 0.51 cm in thickness. The ball floats freely at the resonant frequency of 17,000 Hz, 80 V, and 1.2 W power.

b. The second model of the spherical squeeze film bearing is considerably smaller than the first and uses a standard steel ball bearing which weighs

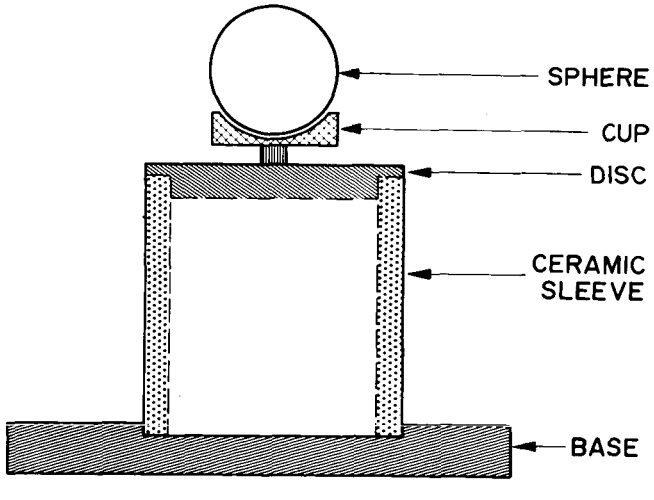

FIGURE 14. SPHERICAL SQUEEZE FILM BEARING WITH AMPLIFYING DISC

0.23 kg and is 3.81 cm in diameter. On this model the thickness of the disc supporting the cup was calculated to make the disc resonate at the same frequency as the ceramic sleeve and to amplify its motion. The sleeve measures 5.08 cm in length and outside diameter and 0.64 cm in thickness. The ball floats freely at the resonant frequencies of 9,200 and 13,600 Hz, 60 V, and 0.54 W power.

CONCLUSIONS

Knowledge gained from both experimental and theoretical work suggests that certain limitations of ceramics be observed. Since the ceramic is a heat source, it should be used in a squeeze film bearing in such a manner that its own heat is dissipated and that it does not interfere with heat dissipation of other sources. Ceramics can undergo small but important dimensional changes from both self-heating and aging. These dimensional changes can result in bearing seizure when the ceramic is used as a bearing surface if proper care is not taken in matching the thermal expansion characteristics of this ceramic bearing surface and the other bearing surface. Finally, the problem of providing the ceramic with an adequately hard metal surface presents itself if the ceramic is to be used as a bearing surface.

It appears that most, if not all, of these problems are avoided if the ceramic is used only as a source of excitation for a conventional metallic bearing surface. This arrangement allows use of mechanical amplification of the ceramic's relatively small (0.000127 cm is typical) excursion by proper suspension.

The existence of a squeeze film force, under the conditions described earlier, has been verified many times, both theoretically and experimentally. The feasibility of constructing a squeeze film bearing for gyro applications able to comply with the imposed constraints of weight, power required, heat generated, static and dynamic behavior, etc., remains to be determined. As the present time, however, there appear to be no insurmountable problems in the construction of an adequate squeeze film bearing suitable for gyro applications.

REFERENCES

1. Salbu, E. O. J.; Compressible Squeeze Films and Squeeze Bearings, IBM Research Report, RJ253, July 1, 1963.

2. Pan, C. H. T.; Analysis, Design, and Prototype Development of Squeeze-Film Bearings for AB-5 Gyro -- Phase I Final Report, Bearing Analysis and Preliminary Design Studies, MTI 64TR66, Mechanical Technology, Inc., November 15, 1964.

D. RECENT DEVELOPMENTS IN ADAPTIVE TRACKING NOTCH FILTER TECHNIQUES

by Michael T. Borelli, Stanley N. Carroll, and Hans H. Hosenthien

Some recent advancements in the development and analysis of the adaptive tracking notch (ATN) filter are presented. The ATN filter was developed to help stabilize the structural bending signals encountered in the control loop of large aerospace vehicle boosters. First, an ATN filter that utilizes a simple differential amplifier is described, and its equivalence to the ATN filter that utilizes a chopper-stabilized operational amplifier is presented. Second, the presence of a quadrature component in the output signal of the ATN filter is shown to exist, and its effect on the notch characteristics is presented. A means of minimizing this effect is given along with a theoretical expression that approximately describes the magnitude of the in-phase and quadrature components when the input and commutating frequencies are the same. Finally, an analytical expression for the transfer function of the coupled ATN filter is presented, and its frequency response characteristics are discussed and compared to experimental data. Also, the relationship showing the dependence of the output harmonic frequencies of the ATN filter on the number of commutated capacitors employed and the respective phasing of the commutating functions is summarized.

INTRODUCTION

The adaptive tracking notch (ATN) filter was developed to help stabilize the structural bending signals encountered in the control loop of large aerospace vehicle boosters. In two previous articles (Refs. 1 and 2), the ATN filter was described in detail and results from its use in analog computer simulations of the Saturn V flight were presented. Although an ATN filter breadboard autopilot has operated very satisfactorily in all laboratory tests and simulations conducted thus far, the present design is by no means considered optimum.

This article describes some of the work completed in the continued development of the ATN filter and includes (1) a mechanization simplification by the substitution of differential amplifiers for chopper stabilized amplifiers, (2) investigations of compensation for the filter's quadrature component of the structural bending mode signals, and (3) analytical studies that include (a) the derivation of a suitable transfer function for the RC commutated network utilized in the ATN filter, (b) the determination of the sideband signals generated by the RC commutated network, and (c) the calculation of the optimum value of feedback adjustment for the RC commutated network.

NOMENCLATURE

a	phasing parameter (equal to 1 or 2)
a_k	Fourier coefficients of output signal
A_{2k}	attenuation of filter at frequency $2k\omega_o$
b_k	Fourier coefficients of output signal
D	special function
e	voltage function, volts
G	transfer function
h(t), H(s)	linear network, (time, frequency domain)
j	$\sqrt{-1}$
k	integer
K	potentiometer setting
K'	feedback gain
m	integer
n	integer
N	number of commutated capacitors (also equal to number of paths)
$P_n(t)$	commutating function

P_m, P_k	Fourier coefficients of commutating functions
q	integer
s	complex variable, radians/second
t	time, seconds
T_o	period of commutating functions
x, X	input signal (time, frequency domain)
y, Y	output signal (time, frequency domain)
α_o	reciprocal of equivalent time constant, 1/seconds
β	normalized frequency
γ	dimensionless parameter
δ	phase angle, radians
λ	time shift, seconds
ϕ_{2k}	phase shift of filter at frequency $2k\omega_o$
τ	time constant, seconds
ω	angular frequency, radians/second
ω_o	angular frequency of commutating functions, radians/second

DIFFERENTIAL AMPLIFIER ATN FILTER

In the ATN filters developed previously, chopper-stabilized operational amplifiers were used in the RC commutated networks. To simplify the mechanization of the ATN filter, investigations were conducted to determine if differential amplifiers could be used in lieu of the chopper-stabilized operational amplifiers. Both analytical and experimental investigations have shown that equivalent performance can be obtained.

Schematic diagrams for the RC commutated networks as used with chopper-stabilized operational and differential amplifiers are shown in Figures 1 and 2, respectively. The derivation of the equation representing the commutated network output voltage e_2 of Figure 1 is obtained in the following way.

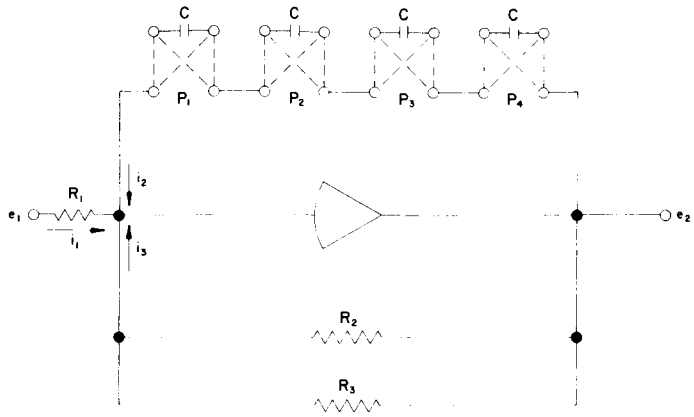

FIGURE 1. RC COMMUTATED NETWORK FOR CHOPPER-STABILIZED OPERATIONAL AMPLIFIER

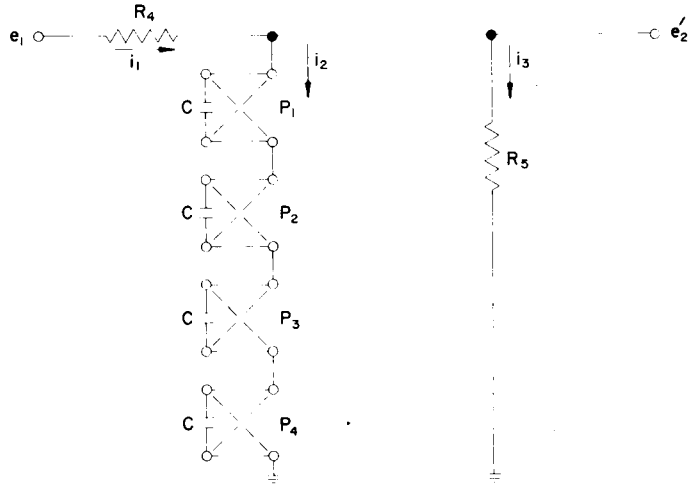

FIGURE 2. RC COMMUTATED NETWORK FOR DIFFERENTIAL AMPLIFIER

$$i_1 + i_2 + i_3 = 0 \qquad (1)$$

where $i_1 = \frac{e_1}{R_1}$ and $i_3 = e_2 \left(\frac{1}{R_2} + \frac{1}{R_3} \right)$;

therefore

$$i_2 = -\left[\frac{e_1}{R_1} + e_2 \left(\frac{1}{R_2} + \frac{1}{R_3} \right) \right]. \qquad (2)$$

The voltage across the commutated capacitors is

$$e_2 = \sum_{n=1}^{4} \frac{P_n}{C} \int P_n \, i_2 \, dt \qquad (3)$$

where P_n is the square-wave commutating functions for each capacitor.

Now substitute equation 2 into equation 3 to obtain the desired relation

$$e_2 = -\sum_{n=1}^{4} \frac{P_n}{C} \int P_n \left[\frac{e_1}{R_1} + e_2 \left(\frac{1}{R_2} + \frac{1}{R_3} \right) \right] dt \ . \quad (4)$$

The equation for the output voltage of the RC commutated network of Figure 2 is obtained in much the same manner.

$$i_1 = i_2 + i_3 \quad (5)$$

$$\text{where } i_1 = \frac{e_1 - e_2'}{R_4} \quad \text{and } i_3 = \frac{e_2'}{R_5} \ ;$$

therefore

$$i_2 = \frac{e_1}{R_4} - e_2' \left(\frac{1}{R_4} + \frac{1}{R_5} \right) \ . \quad (6)$$

The voltage across the commutated capacitors is

$$e'_2 = \sum_{n=1}^{4} \frac{P_n}{C} \int P_n \, i_2 \, dt. \quad (7)$$

Now substituting equation 6 into equation 7,

$$e_2' = \sum_{n=1}^{4} \frac{P_n}{C} \int P_n \left[\frac{e_1}{R_4} - e_2' \left(\frac{1}{R_4} + \frac{1}{R_5} \right) \right] dt. \quad (8)$$

By the proper selection of the resistors, equations 4 and 8 can be seen to have the same form. For example, in equation 4 let $R_2 = R_1$ and in equation 8 let $R_4 = R_1$ and $R_5 = R_3$; then equations 4 and 8 have the same form except for some important differences in signs. The differences in signs are resolved when the two circuits are utilized in a notch filter circuit as shown in Figures 3 and 4.

From Figure 3 the output of the ATN filter utilizing a chopper-stabilized operational amplifier commutated network is

$$e_3 = -(e_1 + e_2) \ . \quad (9)$$

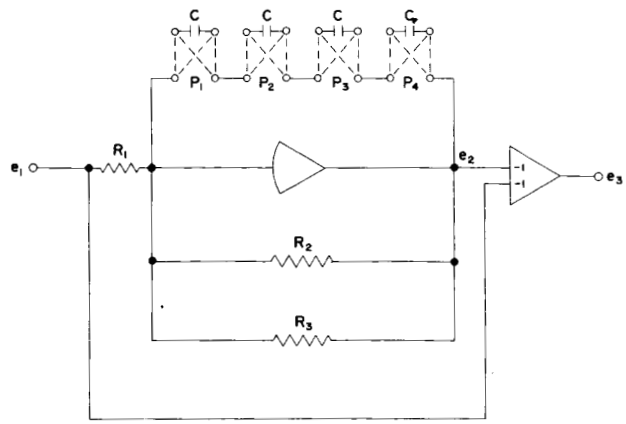

FIGURE 3. ATN FILTER WITH CHOPPER-STABILIZED OPERATIONAL AMPLIFIER

Substituting equation 9 into equation 4 to eliminate the voltage e_2 and letting $R_2 = R_1$, the output voltage of the ATN filter is obtained.

$$e_3 = -\left\{ e_1 + \sum_{n=1}^{4} \frac{P_n}{R_3 C} \int P_n \left[e_1 + \left(1 + \frac{R_3}{R_1} \right) e_3 \right] dt \right\}. \quad (10)$$

The output of the ATN filter utilizing the differential amplifier commutated network of Figure 4 is

$$e_3 = e_2' - e_1 \ . \quad (11)$$

Substituting equation 11 into equation 8 to eliminate the voltage e_2' and letting $R_4 = R_1$ and $R_5 = R_3$, the output voltage of the ATN filter is obtained.

$$e_3 = -\left\{ e_1 + \sum_{n=1}^{4} \frac{P_n}{R_3 C} \int P_n \left[e_1 + \left(1 + \frac{R_3}{R_1} \right) e_3 \right] dt \right\}. \quad (12)$$

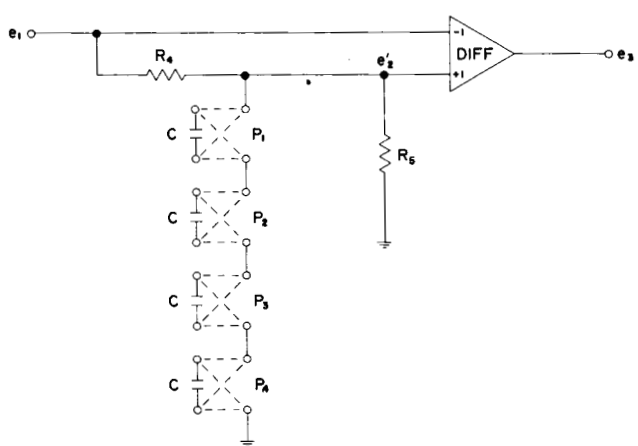

FIGURE 4. ATN FILTER USING A DIFFERENTIAL AMPLIFIER

Thus the equivalence of the two ATN filter circuits is established. In addition to the simplification achieved by replacing a chopper stabilized amplifier with a differential amplifier, one less amplifier is required for the ATN filter of Figure 4 than for the ATN filter of Figure 3.

To verify these analytical results experimentally, two equivalent circuits were built and tested. Although the values of the circuit parameters (R_1, R_2, C, etc.) for the two circuits are not equal, the values of R_3 C and R_3/R_1 are equal. Normalized amplitude frequency response plots of the two circuits tested are shown in Figure 5. Good correspondence (approximately 5 percent error or less) between the two circuits is obtained below and around the notch. By trimming the values of R_3 C and R_3/R_1 in one of the circuits, a closer correspondence between the dynamic performance of the two circuits can be obtained.

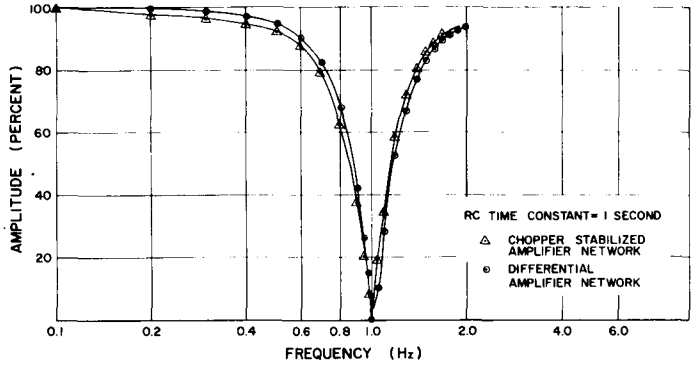

FIGURE 5. ATN FILTER AMPLITUDE, FREQUENCY RESPONSES FOR FOUR CAPACITOR NETWORKS

The equivalence between the differential and the chopper-stabilized amplifier circuits have thus been shown, but some specific limitations are imposed on networks employing transistorized differential amplifiers. These limitations are attributed to the inherent characteristics of the transistorized differential amplifier. For example, the temperature sensitivity of the amplifier is proportional to the value of the input and feedback resistors. This means that smaller resistances should be used and therefore larger capacitances to obtain the same dynamic performance.

QUADRATURE COMPONENT OF THE CONSTRUCTED BENDING MODE SIGNAL

The ATN filter attenuates a bending mode signal by generating a reversed phase bending signal which, when added to the control sensor output signal, will suppress the amplitude of the bending mode component. Complete suppression cannot be realized because the generated signal does not have an exact 180-degree phase relationship with the input signal. Based on the transfer function of the commutated network defined and discussed in the next section, the frequency response locus in the complex plane is approximately a circle as shown in Figures 6A and 6B. The input to the commutated network is the vector $x(\omega_n)$, and the output component at the same frequency as the input is $Ky(\omega_n)$, where n = 0 and 1 ($\omega_1 < \omega_0$) ... and K is the feedback potentiometer setting or the gain adjustment. In Figure 6A, ω_0 is the commutating frequency. The angle δ is greatly exaggerated to show clearly the presence of a quadrature component $Ky(\omega_0)_q$ of the bending mode signal at ω_0.

The notch filter output $R(\omega_n)$ is obtained by the vector addition of $x(\omega_n)$ and $Ky(\omega_n)$. Figure 6B shows that the notch will always occur below the commutating frequency ω_0, or at the frequency ω_1 as shown. Also, the smaller the angle δ, the smaller the quadrature

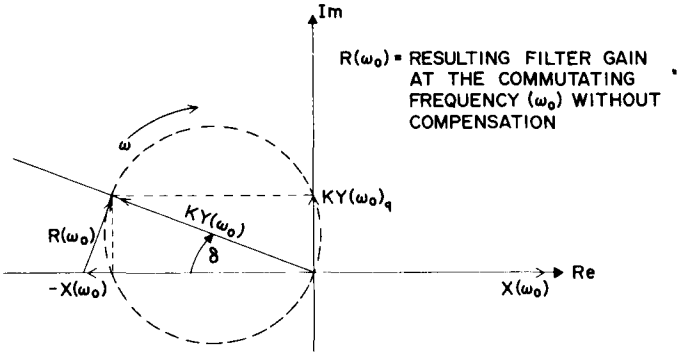

FIGURE 6A. VECTOR DIAGRAM AT THE COMMUTATING FREQUENCY ω_0.

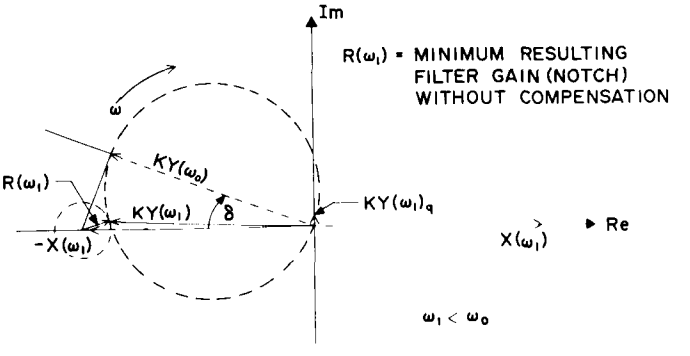

FIGURE 6B. VECTOR DIAGRAM AT THE FREQUENCY OF THE NOTCH ω_1

component will be and the deeper the notch. If $\delta = 0$, the notch depth would be infinite, where the notch depth is defined as the reciprocal of the normalized gain at the notch frequency. The factor K, the feedback potentiometer setting, is adjusted to minimize the resulting vector $R(\omega_0)$. The minimum value of vector $R(\omega_0)$ occurs when $R(\omega_0)$ is perpendicular to the $Ky(\omega_0)$ vector and will yield its minimum at the commutating frequency ω_0.

One technique successfully employed in reducing the effects of the quadrature is a phase lead network in the path containing the commutated network as shown in Figure 7A (or equivalently, to include a phase lag circuit in the unity gain path, Figure 7B). The phase shift rotates the vector $Ky(\omega_0)$ toward the negative real axis, thereby reducing the phase angle δ. The angle δ is small enough at the commutating frequency ω_0 that the phase shift network does not appreciably alter the length of the vector, but does provide the proper phase. Once the amount of phase shift has been determined, it is always possible to change the commutated network gain slightly, if necessary, to yield the maximum notch depth. When the angle δ is small (5 degrees), the compensated phase shift will vary only slightly throughout the first bending mode frequency range. This characteristic provides good improvement to the notch depth throughout the desired tracking range.

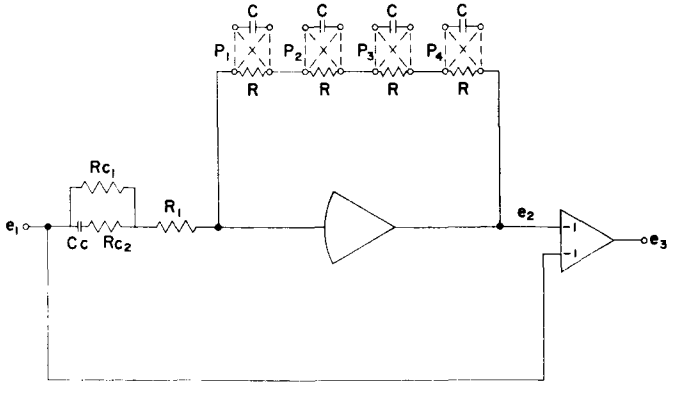

FIGURE 7A. UNCOUPLED ATN FILTER WITH LEAD QUADRATURE COMPENSATION

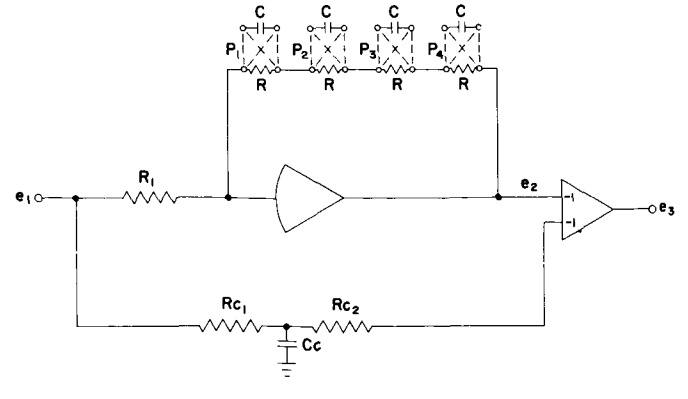

FIGURE 7B. UNCOUPLED ATN FILTER WITH LAG QUADRATURE COMPENSATION

Two RC commutated network configurations, coupled and uncoupled (Ref. 1), have been studied and their equivalent circuits are shown in Figures 8A and 8B, respectively. For the uncoupled case, an analytical expression for the quadrature shows it to be entirely dependent on the RC time constant and the commutating frequency. This can be established by first deriving the fundamental output of a four capacitor uncoupled case. For a sine wave input of frequency ω_0

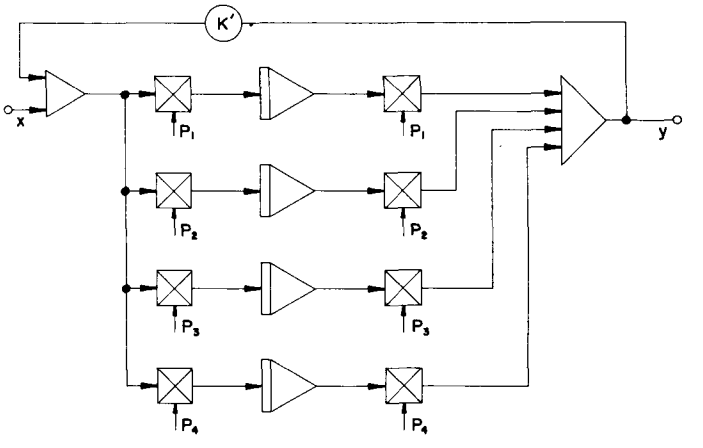

FIGURE 8A. EQUIVALENT DIAGRAM FOR COUPLED RC COMMUTATED NETWORK

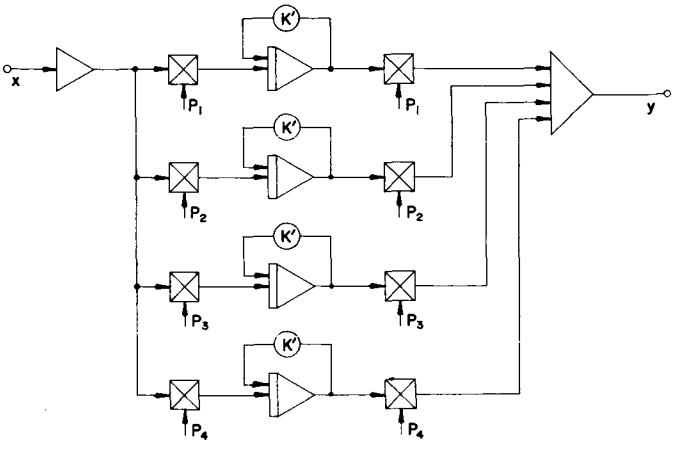

FIGURE 8B. EQUIVALENT DIAGRAM FOR UNCOUPLED RC COMMUTATED NETWORK

and maximum amplitude x_0, the fundamental output can be shown to be

$$\frac{y(t)}{x_0} = \frac{-8k_0}{\pi^2}\left[1 + \sum_{k=1}^{\infty} \frac{2(4k^2+1)\,A_{2k}\cos\phi_{2k}}{(4k^2-1)^2}\right] \sin\omega_0 t + \frac{8k_0}{\pi^2}\left[\sum_{k=1}^{\infty} \frac{8k\,A_{2k}\sin\phi_{2k}}{(4k^2-1)^2}\right]\cos\omega_0 t \quad (13)$$

where

$$A_{2k} = \frac{1}{\sqrt{1 + 4k^2(RC)^2\omega_0^2}}$$

ϕ_{2k} = arc tan $2kRC\omega_0$

k_0 = dc gain of smoothing filter (first order)

ω_0 = commutating frequency.

A_{2k} and ϕ_{2k} are the attenuation and phase of the integrator of Figure 8B with the negative resistive feedback that acts as a first order smoothing filter measured at frequency $\omega = 2k\omega_0$ (only even harmonics of ω_0 are present at the smoothing filter because of demodulation by the first multiplier). The magnitude of the quadrature component is the coefficient of the cosine term and the magnitude of the in-phase component is the coefficient of the sine term. The signs associated with equation 13 verify that the vector representing y(t) will be as indicated in Figure 6. The angle δ can be computed by taking the inverse tangent of the ratio of the magnitudes of the quadrature to in-phase component. The two infinite series can be expressed in closed form (Ref. 3) after substituting for A_{2k} and ϕ_{2k}. The final result is

$$\delta = \tan^{-1}\left\{\frac{\gamma\left[\pi(\gamma^2+1) - 4\gamma\coth\frac{\pi}{2\gamma}\right]}{\pi(\gamma^2+1) + 2\gamma(\gamma^2-1)\coth\frac{\pi}{2\gamma}}\right\} \quad (14)$$

where $\gamma = RC\omega_0 = \tau\omega_0$.

If the commutating frequency is much greater than the break frequency of the first order smoothing filter, i.e., $\tau\omega_0 >> 1$, a good approximation to equation 14 is

$$\delta \cong \tan^{-1}\frac{0.188\gamma}{1 + 0.405\gamma^2} . \quad (15)$$

For $\gamma = 1$, $\delta = 17$ degrees; for $\gamma = 2\pi$, $\delta = 4.2$ degrees. This shows that if the break frequency is decreased from ω_0 to $\frac{\omega_0}{2\pi}$ the angle δ is reduced from 17 degrees to 4 degrees. The above results indicate how the notch frequency depends on the RC time constant through the magnitude of the phase angle δ.

Although equation 14 was derived for four capacitors, it can be shown (Ref. 4) that the equation holds true regardless of how many resistor-capacitor pairs are employed, provided the RC values are the same. In contrast, for the coupled configuration, the angle δ becomes smaller as the number of capacitors is increased. As stated previously, δ must be reasonably small to obtain a good notch depth. The reason a correction circuit is required in the uncoupled case to reduce the quadrature component as opposed to using a large time constant is that the larger time constant yields a notch too narrow to satisfactorily suppress the bending mode signal. The effects of the time constant on the notch filter frequency response are shown in Figures 9A and 9B for the coupled case. For a

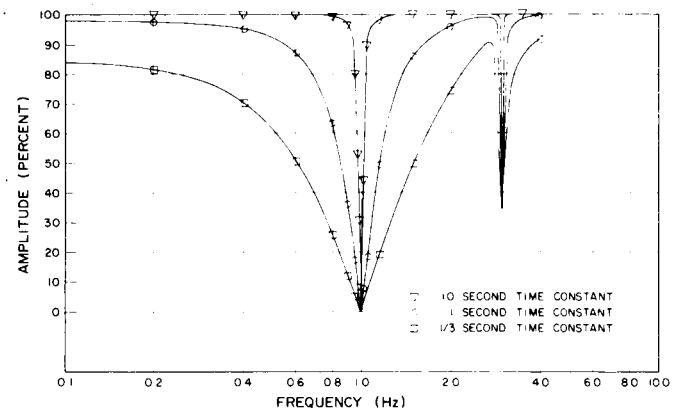

FIGURE 9A. ATN FREQUENCY RESPONSE, AMPLITUDE –THEORETICAL

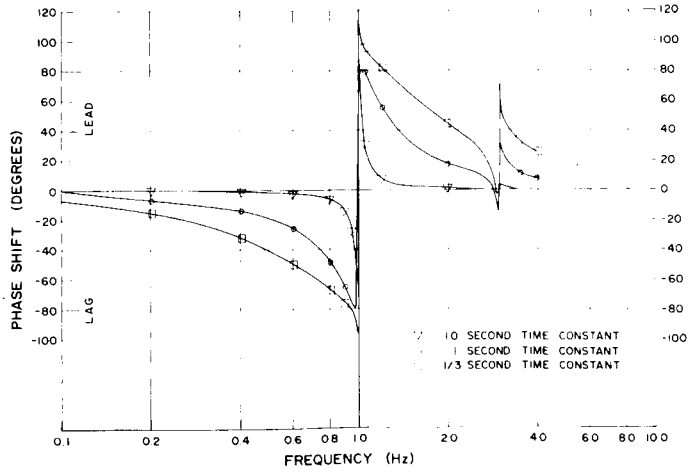

FIGURE 9B. ATN FREQUENCY RESPONSE, PHASE –THEORETICAL

large time constant, it was found that the response of the uncoupled case is approximately the same as that of the coupled case.

The quadrature signal in the coupled configuration is much smaller than in the uncoupled configuration. This is attributed to the cross-coupling terms appearing in the equations as a result of the feedback loop with gain K'. The block diagram of the coupled case can be represented as the product of the uncoupled case and a network containing only the cross-coupling terms. Based on this equivalent block diagram, it is concluded that the cross-coupling terms tend to reinforce the in-phase component and attenuate the quadrature component. Although a general expression for δ has not been derived for the coupled case (similar to equation 14), it is possible to calculate the value of δ from the transfer function (equation 16) for given values of RC, K', and ω_0. In the present design of the coupled ATN filter, the angle δ has been calculated to be less than one degree.

ANALYTICAL STUDIES OF RC COMMUTATED NETWORKS

This section reviews three important characteristics of RC commutated networks as applicable to the ATN filter. First, the transfer function and the sideband spectrum for the commutated network in the ATN filter are discussed. Second, it is shown that the sideband frequencies depend only on the number of commutated capacitors employed and the phasing between the commutating driving functions. Third, a derivation for the optimum value of the feedback gain is given.

Transfer Function For The Coupled Case

If the RC commutated network in the ATN filter is subjected to a single-frequency input, the total output signal is comprised of a primary frequency component plus certain sideband, or complementary, frequency components. The primary frequency is the same as the input frequency; the sideband frequencies occur at multiples of eight times the commutating frequency plus and minus the primary frequency for four commutated capacitors. An analytical expression has been derived (Ref. 4) for the output frequency spectrum of the commutated network. The term "transfer function" is used here to denote the ratio of the output component at the primary frequency to that of the input driving signal. Using this definition, the output spectrum can be written as the sum of the transfer function and the spectrum of the sideband frequencies.

The transfer function for the circuit shown in Figure 10 is given by equation 16 (Ref. 4).

$$\frac{Y_0(s)}{X(s)} \triangleq G(s)$$

$$= \frac{-\alpha_0\left(1 - \frac{\tan\beta}{\beta}\right) + \alpha_0 D \frac{\tan\beta}{\beta}}{s + K'\alpha_0\left(1 - \frac{\tan\beta}{\beta}\right) - (s + K'\alpha_0)\, D \frac{\tan\beta}{\beta}} \qquad (16)$$

where

$$D = \frac{K'\alpha_0}{s + K'\alpha_0}\left\{-\frac{\pi s\,(s + K'\alpha_0)}{8K'\alpha_0\omega_0}\left[\coth\frac{\pi s}{8\omega_0} - \coth\frac{\pi(s + K'\alpha_0)}{8\omega_0}\right] - 1\right\}$$

$$\tau = R_1 C$$

$$\alpha_0 = \frac{4}{\tau}$$

$$\beta = \frac{\pi}{2}\, j\, \frac{s}{\omega_0}$$

K = potentiometer setting

K' = feedback gain, $\frac{R_1}{R_f}$ K

ω_0 = commutating frequency

Y_0 = primary frequency component.

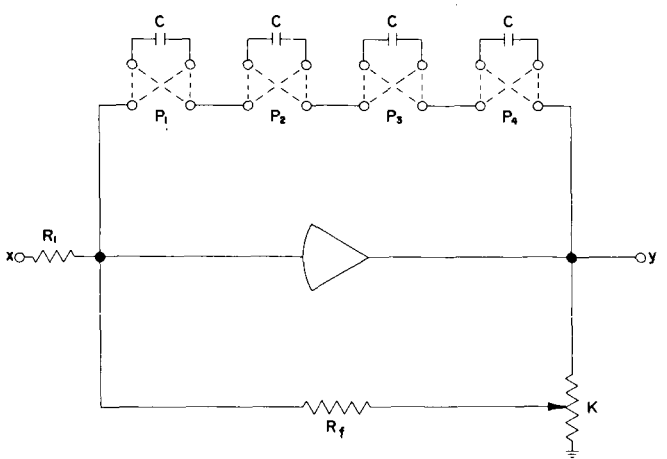

FIGURE 10. FOUR CAPACITOR COMMUTATED NETWORK

The equation relating the sideband amplitudes to the input is

$$\frac{Y_q(j\omega + jq8\omega_0)}{X(j\omega)}$$

$$= \frac{(j\omega + jq\,8\omega_0 + K'\,\alpha_0)\; G(j\omega + jq\,8\omega_0) + \alpha_0}{j\omega + K'\,\alpha_0} \qquad (17)$$

where q is all integers except zero, $G(j\omega + jq\,8\omega_0)$ is the value of the transfer function (equation 16) evaluated at frequency $(\omega + 8q\,\omega_0)$, and $Y_q(j\omega + jq8\omega_0)$ is the sideband component at frequency $(\omega + 8q\omega_0)$.

The term D in equation 16 is present because the sideband frequencies in the output are fed back through K', which results in an output component at the primary frequency. For frequencies between zero and 2.5 ω_0, D can be neglected without introducing more than approximately five percent error (Ref. 5).

A comparison between the theoretical and experimental frequency responses for the notch filter is shown in Figure 11. There are two important parameters in the notch filter: the RC time constant and the feedback gain K'. The time constant is used to control the width of the notch, as shown in Figures 9A and 9B. The time constant also slightly affects the frequency at which the minimum gain value (notch) will occur as previously discussed. Variations in the feedback gain K' about its nominal value have negligible effect on the notch width, but mainly determine the minimum gain value at the notch frequency.

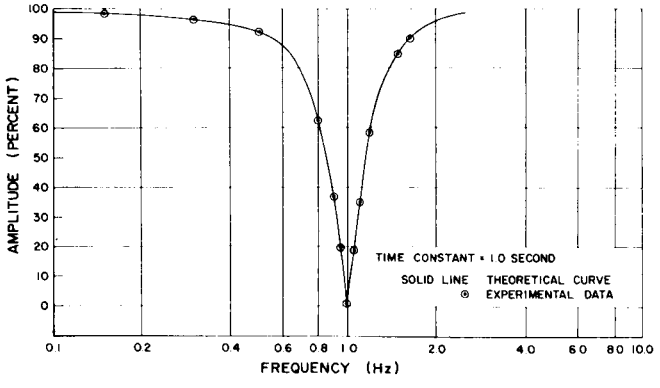

FIGURE 11. ATN FREQUENCY RESPONSE, AMPLITUDE –THEORETICAL AND EXPERIMENTAL

Determination of Sideband Frequencies

As indicated in equation 17 the sideband frequencies depend on the term $q8\omega_0$ where the number eight results from two factors: the number of capacitors utilized and the respective phasing between the commutating driving functions. The dependence of the sideband frequencies on these two factors can be seen by investigating the fundamental equation describing the N capacitor configuration shown in Figure 12. For N = 4, the circuits in Figures 10 and 12 are equivalent. This equation (Refs. 4 and 6) is

$$-Y(s) = \sum_{m=-\infty}^{\infty} \sum_{k=-\infty}^{\infty} \left(\sum_{n=1}^{N} e^{-j\omega_0\lambda\,(n-1)\,(k+m)} \right)$$

$$P_m\, P_k H(s-j\omega_0 k) \left[X(s-j\omega_0 k - j\omega_0 m) + K'Y(s-j\omega_0 k - j\omega_0 m) \right] \qquad (18)$$

where

P_m, P_k = Fourier coefficients of the square wave commutating functions

$H(s) = \frac{-1}{\tau s}$

T_0 = period of commutating functions

N = number of commutated capacitors

$\lambda = \frac{T_0}{aN}$

a = phasing parameter (equal to 1 or 2).

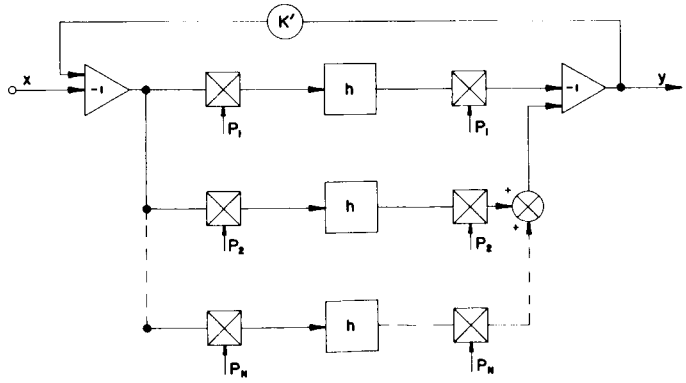

FIGURE 12. EQUIVALENT CIRCUIT FOR N COMMUTATED CAPACITORS

The exponential factor occurs in equation 18 because the nth commutating function is shifted by $\lambda(n-1)$ seconds relative to $P_1(t)$, i.e. $P_n(t) = P_1[t-\lambda(n-1)]$. The significance of the frequency shift in the argument of the input term, X, in equation 16 is that the sideband frequencies will be at $\omega + \omega_0(k+m)$. It will be shown that equation 18 is identically zero unless $(k+m)$ is a multiple of aN, thereby establishing the dependence of the sideband frequencies on the phasing parameter and the number of commutated capacitors.

The summation over n is seen to be a geometric series. Since

$$\omega_0\lambda = \frac{2\pi}{aN}, \text{ then}$$

$$\sum_{n=1}^{N} e^{-j\frac{2\pi}{aN}(n-1)(k+m)} = 1 + e^{-j\frac{2\pi}{aN}(k+m)}$$

$$+ e^{-j\frac{2\pi}{aN}(k+m)2} + \ldots + e^{-j\frac{2\pi}{aN}(k+m)(N-1)}. \quad (19a)$$

For $k+m = q(aN)$, where q assumes certain integral values, each of the N terms in the series is unity. If $k+m \neq q(aN)$, the series can be expressed in closed form as

$$\sum_{n=1}^{N} e^{-j\frac{2\pi}{aN}(n-1)(k+m)} = \frac{1 - e^{-j2\pi\frac{(k+m)}{a}}}{1 - e^{-j2\pi\frac{(k+m)}{aN}}}. \quad (19b)$$

Because $\frac{k+m}{aN}$ was assumed not to be an integer in equation 19b, the denominator is non-zero. In contrast, the numerator is identically zero since $\frac{k+m}{a}$ is always an integer.

Therefore

$$\sum_{n=1}^{N} e^{-j\frac{2\pi}{aN}(k+m)(n-1)} = N \text{ for } k+m = q(aN) \quad (19c)$$

$$= 0 \text{ otherwise.}$$

With the constraint $k+m = q(aN)$, and replacing s by $j\omega$ in equation 18, it is seen that the sideband frequencies will be at $\omega + q(aN)\omega_0$. The two values, 1 and 2, of the phasing parameter "a" corresponds to using a complete circle (2π radians) or a half circle (π radians) for phasing the commutating functions. The admissible values of q depend upon whether N is even or odd and the two possible values of "a." Because the commutating functions are square waves, $k+m$ is always an even number; thus the number q(aN) must also be even. If N is even, then either value of the phasing parameter "a" results in all integers for q being admissible. Likewise, all values of q are admissible if "a" is even and N is odd. However, when both N and "a" are odd, then q must assume only even values. The final result is that for odd N the sideband frequencies will be at $\omega + q(2N)$, and for even N the sideband frequencies will be at $\omega + q(aN)$, $q = 0, \pm1, \pm2, \ldots$. For the ATN filter, $a = 2$ was chosen because it was desired to eliminate as many low sideband frequencies as possible.

Optimum Value of Feedback Gain K'

It was stated in a previous section that the phase angle δ (Fig. 6) is approximately zero for the coupled configuration of the commutated network. If this angle is assumed to be zero, it is apparent that exact cancellation between the bending mode component contained in the sensor signal and the reversed phase signal depends only on the feedback gain K'. Using steady state analysis, an expression for the optimum K' can be derived and is seen to depend only on the order of harmonics in the commutated network output.

With reference to Figure 13, the average value of the input to each of the four integrators must be zero

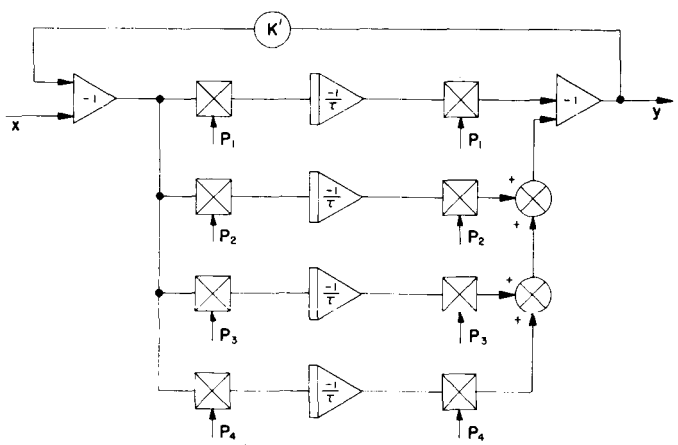

FIGURE 13. EQUIVALENT CIRCUIT FOR FOUR COMMUTATED CAPACITORS

in a steady state condition. The path containing the first integrator will be considered since $P_1(t)$ is in phase with the input signal. The Fourier series for $P_1(t)$ is

$$P_1(t) = \frac{4}{\pi} \sum_{n=0}^{\infty} \frac{\sin (2n+1)\omega_0 t}{2n+1} . \quad (20)$$

The input and output signals are given as

$$x(t) = x_0 \sin \omega_0 t \quad (21)$$

$$y(t) = \sum_{k=0}^{\infty} (a_k \cos k\omega_0 t + b_k \sin k\omega_0 t). \quad (22)$$

The average value of the signal into the first integrator will be the dc component that results from multiplying $P_1(t)$ by $x(t) + K'y(t)$. Since the product of a sine and a cosine term contributes no dc component, the net dc component results from multiplying the corresponding sine terms of like frequencies. It is seen that the total dc is

$$dc = \frac{2x_0}{\pi} + \frac{2K'}{\pi} \sum_{n=0}^{\infty} \frac{b_{2n+1}}{2n+1} , \quad (23)$$

or since equation 23 must be zero,

$$K' = \frac{-x_0}{\sum_{n=0}^{\infty} \frac{b_{2n+1}}{2n+1}} . \quad (24)$$

Using equations 16 and 17, for $s = j\omega_0$, and assuming $x_0 = -b_1$ to have exact cancellation, it can be shown that the amplitudes of the harmonic components are

$$Y_q\left[\omega_0 (1-8q)\right] = x_0 \left[\frac{\alpha_0 (1 - K') - j\omega_0}{K'\alpha_0 + j\omega_0 (1-8q)}\right] . \quad (25)$$

If the time-constant is sufficiently large that $\alpha_0 K'$ can be neglected relative to $\omega_0 (1-8q)$, and by knowing that K' is close to unity, then equation 25 can be approximated by

$$\frac{Y_q[\omega_0(1-8q)]}{x_0} \cong \frac{1}{8q-1} , \quad q = \pm 1, \pm 2, \ldots \quad (26)$$

The amplitude of the harmonic components given by equation 25 corresponds to the Fourier coefficients "b" in equations 22 and 24. Equation 26 implies that $b_3, b_5, b_{11}, b_{13}, \ldots$ are zero since the third, fifth, ... harmonics are not present. Also, the amplitude of the seventh, ninth, ... harmonics are proportional to 1/7, 1/9, ..., respectively. Because the output is 180 degrees out of phase with the input, each of the Fourier coefficients, b_{2n+1}, in equation 24 is negative as shown in Reference 4. Using equation 26 in equation 24 gives, for the four capacitor case,

$$K' = \frac{1}{1 + \frac{1}{7^2} + \frac{1}{9^2} + \frac{1}{15^2} + \frac{1}{17^2} + \ldots} \cong 0.95. \quad (27)$$

In general, if $\tau\omega_0 >> 1$, a good approximation for the feedback gain is

$$K' = \frac{1}{\sum_{n=1} \frac{1}{n^2}} \quad (28)$$

where the index n corresponds to the order of harmonics which are present in the output. For the two capacitor case, all odd harmonics are present and equation 28 yields

$$K' = \frac{1}{\sum_{n=0}^{\infty} \frac{1}{(2n+1)^2}} = \frac{8}{\pi^2} . \quad (29)$$

Equations 27 and 29 are in excellent agreement with experimental results.

CONCLUSIONS

The results obtained from these investigations have (1) permitted a simplification of the mechanization of the ATN filter for some applications, (2) improved the performance of the ATN filter, and (3) achieved an improved understanding of the operation of RC commutated networks. The derivation of the transfer function for the RC commutated networks is a definite extension of the state of the art for this type of circuit. The use of this new analytical tool will be

reflected in a considerable reduction in the required experimental efforts in further development work.

Future development efforts will include replacing the present mechanical relays for the commutated elements with electronic switches. Investigations will also be made to improve the identification function or the tracker system of the ATN filter.

REFERENCES

1. Hosenthien, Hans H., and Borelli, Michael T.; An Adaptive Tracking Notch Filter for Suppression of Structural Bending Signals of Large Space Vehicles. Astrionics Research and Development Report No. 1, NASA TM X-53000, October 1, 1963, Huntsville, Alabama.

2. Hosenthien, Hans H., and Borelli, Michael T.; Adaptive Phase Stabilization of Bending for Large Aerospace Vehicle Booster. Astrionics Research and Development Report No. 2, NASA TM X-53044, May 1, 1964, Huntsville, Alabama.

3. Ryshik, I. M, and Gradstein, I.-S.; Tables of Series, Products, and Integrals. VEB Deutscher Verlag Der Wissenchaften, Berlin, 1963.

4. Carroll, S. N.; Analytical Determination of Transfer Function for RC Commutated Networks. NASA Technical Note, 1965.

5. Auburn Research Foundation, Auburn University; July 1964 Progress Report. Contract NAS8-11116, Auburn, Alabama.

6. Franks, L. E., and Sandberg, I. W.; An Alternative Approach to the Realization of Network Transfer Functions: The N-Path Filter. The Bell System Technical Journal, September 1960.

E. REAL TIME ANALOG COMPUTER SIMULATION OF THE ELASTIC SPACE VEHICLE INVOLVING BEAM CELL TRANSMISSION MATRICES by George L. von Pragenau

A flying space vehicle behaves like a freely moving beam responding with translation, rotation, and oscillations to external forces. The latter especially complicates the analysis and design of a control system used to stabilize the attitude of a space vehicle. Certain measures yield a stable operating control system; however, its design requires a good knowledge of the bending modes of the space vehicle.

The electronic model described is one method to obtain such knowledge or to simulate the space vehicle's response in real time on an analog computer, together with actual control system hardware. The method allows observation of traveling waves; e.g., a disturbance travels in approximately one half of a second from the tail to the nose of the Saturn V space vehicle. Unlike other methods, this process considers the effect of distributed damping of the vehicle's structure and therefore represents more realistically the dynamic effects of elastic vehicles. An electronic model of the Saturn V vehicle was successfully operated together with a control loop to stabilize the vehicle's attitude. The lateral deflection of the beam was displayed by the lateral acceleration at nine stations. Three bending modes or the standing waves resulting from sinusoidal excitation, a traveling wave resulting from unit step excitation, and a reaction of the Saturn V vehicle in the controlled operation mode when excited by a unit step wind force are shown. The frequency response of the model is plotted for sinusoidal excitation at the tail of the vehicle for the frequency range of 0.5 to 10 Hz. A block diagram of the vehicle model and its matrix formulation are included.

Author

INTRODUCTION

The dynamic behavior of a flexing beam can be described by partial differential equations. Partial differential equations approximated by finite difference equations can be solved by analog computers as shown by several authors. The method treated in this article differs from these solutions by applying a matrix formulation not directly related to the partial differential equation. The concept was developed by the Astrionics Laboratory to simulate flexible space vehicles while maintaining good physical insight.

The simulation utilizes standard analog computer equipment to form an electronic model of a space vehicle and allows real time simulation including the hardware of the flight control system. This method simulates transmission characteristics, distributed structural damping, distributed wind forces, and multiple sensor locations. Transfer functions and bending modes are readily obtainable and parameter studies are possible without difficulty. The flexibility of the method will save time and cost in developing control systems and in studying control concepts which are rather complex.

The control system contains attitude sensors, signal conditioners and filters, amplifiers, and a thrust vector actuator system. Attitude sensors are usually placed at accessible locations in a vehicle and detect local attitudes which contain the attitude of the whole vehicle plus the undesirable effect of the vehicle's flexibility. The latter needs special attention and if not properly processed could result in wild oscillations finally leading to failure. The vehicle and the control system compose a feedback loop; if the loop gain is larger than one, instability is possible. Signal conditioners are utilized to shift the phase angle of the sensor signals to damp oscillations artificially, and filters are used to attenuate the gains at the resonance frequencies of the space vehicle.

Commonly the methods of Rayleigh-Ritz or Stodola (Refs. 1, 2, and 3) are employed to determine bending mode shapes and bending frequencies, thus describing the dynamic characteristics of a flexible space vehicle. Structural gains at bending resonances are obtained to design the control system by assuming a certain overall damping. The flexible space vehicle is simply replaced by damped mass-spring resonators for each natural frequency.

Another way to find dynamic vehicle characteristics is ground vibration tests (Ref. 4) on a full size space vehicle. By suspending it as softly as possible to simulate free flight conditions, valuable data can be gained, e.g., damping coefficients and transfer functions at different sensor locations. The test object is vibrated sinusoidally at different frequencies

by a shaker device. Since this method is a test on the actual vehicle, it has a certain value, especially in producing damping data. Checking on local resonance effects is another advantage of ground vibration tests; for very complex systems such as clustered space vehicles, it is probably the only way to obtain a true picture of dynamic effects. However, such tests are costly and difficult to schedule.

Data obtained by these conventional methods are utilized in an analog computer setup. The computer reproduces resonance effects to check out control hardware under simulated dynamic conditions. This is a less direct approach than using an electronic model of the space vehicle. The term model applies here more to analog copying than to a less accurately general representation of dynamic qualities. The model directly simulates the space vehicle based only on mass, stiffness, and damping information; the electrical signals of the model can be fed directly to the control hardware in checkout. With respect to the number of amplifiers of the conventional and the proposed analog computer arrangement for a similar task (six resonances and deflections at six different stations of the vehicle), no difference of computer volume is required; the volume for each case is approximately 32 amplifiers and 12 integrators. However, for special applications where fewer resonances and deflections are required, the conventional analog computer setup employs a smaller computer volume (for 4 resonances and 1 deflection, only 13 amplifiers and 8 integrators), while the electronic model must still maintain a larger volume to avoid inaccuracy.

A possible classification of dynamic data producing methods appears as follows. The ground vibration test represents the empirical method, the electronic model represents the semi-empirical, and the bending mode technique represents the purely analytical method. The electronic model has a dual function; it produces dynamic data and can be used to simulate the overall dynamic behavior of the control system. The method does not require elaborate means to produce data needed for a conventional analog computer simulation.

Stiffness, damping, and mass distributions are essentially all that is needed to generate certain matrix expressions used for the electronic model programing. From all the data, damping is the least well defined information; equivalent viscous damping is employed to approximate dynamic test results. However, it is anticipated that damping-oriented tests will clarify the damping characteristics much better in the near future. By dividing the beam-like object into cells that are represented by matrices, transmission characteristics are preserved. The idealization of the classical methods (Refs. 2 and 3) that consider only "conservative" systems in resonant modes was avoided. A good physical insight was obtained without too much abstraction, thus aiding the usage of the electronic model. Therefore, the direct approach of modeling electronically results in good adaptability. Mass, elasticity, and damping data can be changed readily by potentiometers, and the results are obtained at analog computer computing rates. Scheduling is not difficult and expenses seem to be much lower than for any of the other methods.

The electronic model was tried at first as a rather crude representation of the Saturn V space vehicle by lumping the mass characteristic of each stage about its particular center of gravity. The space vehicle was divided into four mass fields and three interconnecting flexibility fields. Each mass field contained information about mass, moment of inertia, and center of gravity. Each flexibility field described the flexibility contributions of elongation, bending, and shear stiffness. This lumped mechanical model was then described by matrix equations (Ref. 1) which were further used for programing an analog computer. Because the variables were available at the bounds of each field, boundary conditions were easily satisfied.

Other electronic model techniques of elastic beams and partial differential equations are found in the literature (Refs. 5 through 9). These techniques are based on the approximation of partial differential equations by finite differences which make boundary conditions difficult to apply.

The work of Charles Elms (Ref. 10), who built the signal conditioner to show the mode shapes, is gratefully acknowledged, as is the encouragement of my colleagues.

NOMENCLATURE

A	cross section of beam structure
a_0	dc gain of ϕ filter of control loop (Fig. 7)

a_1	dc gain of $\dot{\phi}$ filter of control loop (Fig. 7)
D_i	flexibility matrix of the beam structure between stations i and i + 1 (equation 12)
D_i^{-1}	inversed matrix of D_i
E	modulus of elasticity
F_i	generalized force on flexibility segment at station i, Laplace transformed
$\overline{F}_i$	same force not transformed (equations 2 and 3)
G	modules of rigidity (equation 12)
G_i	mass matrix at station i (equation 4)
G_i^{-1}	inversed matrix G_i
g	center of gravity eccentricity of mass m from a station (Fig. 1)
g_2	dc gain of $\ddot{\gamma}$ filter of control loop (Fig. 7)
I	moment of inertia of lumped mass
J	cross-sectional moment of inertia of beam structure
k	rigidity efficiency of cylindrical shell (equation 12)
L	field length of beam cell (equation 5)
L_i	lever arm matrix from station i to i + 1 (equation 5)
L_i^{-1}	inversed lever arm matrix (equation 5)
$\tilde{L}_i$	transposed lever arm matrix
$\tilde{L}_i^{-1}$	inverse of transposed lever arm matrix
$\overline{M}$	moment, component of generalized force (equations 2 and 3 and Fig. 1)
m	mass of lumped mass at a station (equation 4)
p	Laplace's differential operator
s	variable station on vehicle axis (equation 12)
$\overline{T}$	longitudinal force, component of generalized force (equations 2 and 3)
T_c	controlled thrust force (Fig. 7)
U_i	Laplace transformed deformation of flexing beam cell at stations i (equations 10 and 11)
$\overline{V}$	lateral force or shear force, component of generalized force (equations 2 and 3)
W_i	generalized wind force vector attacking mass G_i at station i
$\ddot{\overline{X}}_i$	space-fixed acceleration vector at station i (equation 1)
$\overline{x}$	space-fixed position component (equation 1)
$\overline{y}$	space-fixed position component (equation 1)
Z_i	body-oriented position vector at station i, Laplace transformed
$\ddot{\overline{Z}}_i$	body-oriented acceleration vector at station i (equation 8)
β	gimbal angle of controlled rocket motors (Fig. 7)
$\ddot{\gamma}$	body-oriented acceleration signal for accelerometer control loop (Fig. 7)
$\overline{\delta}$	space-fixed rotation angle, component of position vector (equations 1 and 7)
δ_i	rotation angle, a component of body-oriented position vector Z_i, Laplace transformed (Figs. 3, 4, and 5)
η_i	lateral deflection, a component of body-oriented position (Figs. 3, 4, and 5)
ϕ	angular control signal of space vehicle's angular position (Fig. 7)

FORMULATION

Generally, rotations of a space vehicle are relatively slow; therefore, it is sufficient to consider only planar motions for the design of the attitude stabilization. Consequently, only these motions will be treated here, while the circumstance is appreciated that the resulting equations are much simpler than those of a three dimensional formulation.

First, equations will be derived relating the space-fixed planar accelerations (two translatory, one angular) of a rigid mass (Fig. 1) to external forces (two normal forces, one moment). As indicated, acceleration is represented by a vector consisting of three components; one in the x direction, one in the y direction, and one being the angular acceleration (equation 1). The force is also a vector composed of three components; one in the longitudinal direction, one normal to the longitudinal axis, and one being the moment (equation 2). As defined, the terms acceleration and force are applied generally to simplify the terminology in connection with the vector equations. The first equation relates the vectors of the forces and accelerations appearing on a rigid body (Fig. 1). The equation can be considered a dynamic equilibrium condition between the external forces $\overline{F}_1$ and $\overline{F}_2$ and the D'Alembert's forces of the mass (equation 6).

A detailed derivation of the equations is beyond the scope of this article; therefore, only the essential equations and steps are shown. Equations of a flexible but massless beam will follow the equations of the massy but rigid beam.

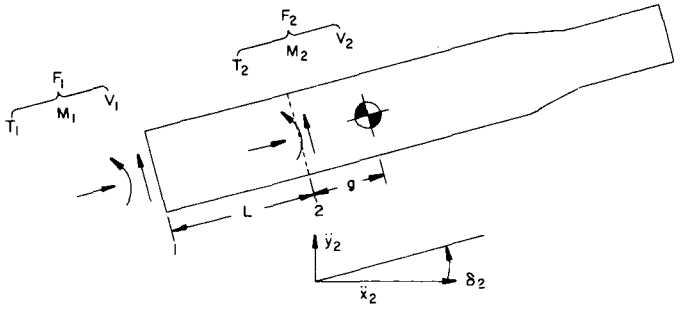

FIGURE 1. FORCES AND DISPLACEMENTS ON THE ELONGATED RIGID BODY

The acceleration vector is defined by

$$\ddot{\overline{X}}_2 = \frac{d^2}{dt^2} \cdot \begin{pmatrix} \overline{x} \\ \overline{y} \\ \overline{\delta} \end{pmatrix}_2 . \tag{1}$$

The force vectors are defined by

$$\overline{F}_1 = \begin{pmatrix} \overline{T} \\ \overline{V} \\ \overline{M} \end{pmatrix}_1 \tag{2}$$

$$\overline{F}_2 = \begin{pmatrix} \overline{T} \\ \overline{V} \\ \overline{M} \end{pmatrix}_2 \tag{3}$$

The effect of the D'Alembert forces is the product of the acceleration of equation 1 projected into body-oriented coordinates and a mass matrix G_2.

$$\dot{G}_2 = \begin{pmatrix} m & 0 & 0 \\ 0 & m & mg \\ 0 & mg & I + mg^2 \end{pmatrix}_2 \tag{4}$$

The components of G_2 contain the mass m of the body, the static moment mg about point 2 (Fig. 1), and the moment of inertia $I + mg^2$ about point 2.

The beam functions also as a lever arm of length L, thus relating the forces $\overline{F}_1$ and $\overline{F}_2$. This is expressed by the lever arm matrix

$$L_1^{-1} = \begin{pmatrix} 1 & 0 & 0 \\ 0 & 1 & 0 \\ 0 & -L & 1 \end{pmatrix}_1 . \tag{5}$$

For very slow motion, the equilibrium condition $\overline{F}_2 = L_1^{-1}\ \overline{F}_1$ is valid; for faster motions this relation must be modified by subtracting D'Alembert's forces $(G_2\Omega_2\ddot{\overline{X}}_2)$.

$$\overline{F}_2 = L_1^{-1}\,\overline{F}_1 - G_2\Omega_2\ddot{\overline{X}}_2 . \tag{6}$$

The matrix Ω_2 projects the space-fixed accelerations $\ddot{\bar{X}}_2$ into body-oriented coordinates.

$$\Omega_2 = \begin{pmatrix} \cos\bar{\delta} & \sin\bar{\delta} & 0 \\ -\sin\bar{\delta} & \cos\bar{\delta} & 0 \\ 0 & 0 & 1 \end{pmatrix}_2 . \qquad (7)$$

Defining a body-oriented acceleration $\ddot{\bar{Z}}_2$ as sensed possible by accelerometers

$$\ddot{\bar{Z}}_2 = \Omega_2 \ddot{\bar{X}}_2 , \qquad (8)$$

and applying Laplace transform to a system initially at rest, equation 6 can be reduced to

$$F_2 = L_1^{-1} F_1 - G_2 p^2 Z_2 . \qquad (9)$$

Next, the deformation of a massless but flexible beam shall be expressed. For small deformations, nonlinear terms such as Coriolis force and centrifugal force are negligible, and the difference between an acceleration at one beam end and the acceleration of the opposite beam end multiplied by the lever arm matrix $\tilde{L}_2$ can be used to formulate a body-fixed acceleration $p^2 U_3$ which is equivalent to deformation.

$$p^2 U_3 = p^2 Z_3 - \tilde{L}_2 p^2 Z_2 . \qquad (10)$$

The deformation U_3 is the deflection of the right beam end measured against the left beam end and thus can be related to the deformation of a cantilever beam. For certain frequency and amplitude ranges, the structural damping can be approximated by viscous damping. Applying this method, the deflection of a beam with damping can be derived from the deflection of a spring-like beam by dividing the deflection of the latter by $1 + p\tau$ where τ is the quotient of a dashpot constant and a spring constant.

$$p^2 U_3 = - \frac{p^2}{1 + p\tau_2} \tilde{L}_2 D_2 F_2 . \qquad (11)$$

The matrix D_2 represents the flexibility of a cantilever beam clamped at the right end and deflected at the left by a force F_2.

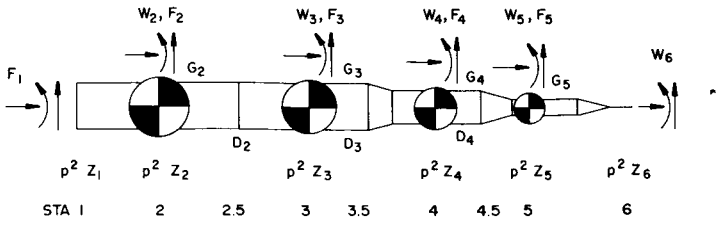

FIGURE 2. LUMPED MODEL OF A SATURN V SPACE VEHICLE

The flexibility matrix D_2 is defined by

$$D_2 = \int_o^L ds \cdot \begin{pmatrix} \frac{1}{EA} & 0 & 0 \\ 0 & \frac{1}{kGA} + \frac{s^2}{EJ} & \frac{-s}{EJ} \\ 0 & -\frac{s}{EJ} & \frac{1}{EJ} \end{pmatrix}_2 . \qquad (12)$$

This concludes the formulation relating the forces and accelerations of the mass cell (stations 1 to 2.5) and the flexibility cell (stations 2 to 3). This is repeated for all the mass cells (stations 2.5 to 3.5, 3.5 to 4.5, and 4.5 to 6) and all the flexibility cells (stations 3 to 4 and 4 to 5) (Fig. 2). Wind forces will be considered by essentially adding a force W_2 to the right half of equation 9.

PROGRAMING

As mentioned previously, the space vehicle was divided into four lumped mass fields (G_2, G_3, G_4, G_5), the S-IC stage, S-II stage, S-IVB stage, and the Apollo spacecraft. Three flexibility fields (D_2, D_3, D_4) were interconnecting the four masses as shown in Figure 2. As displayed in Figure 2 the variables are available at six different stations along the longitudinal axis. External forces are the tail force F_1 and the distributed wind forces W_2 through W_6. Internal forces are the forces F_2 through F_5. For simplicity it is assumed that the forces F_1 and W_6 will not appreciably deform the structure between stations 1 and 2 and between 5 and 6. Now the equations of the lumped model can be arranged.

$$p^2Z_1 = \tilde{L}_1^{-1}\, p^2Z_2 \qquad \text{Lever arm effect} \qquad (13)$$

$$p^2Z_2 = G_2^{-1}(L_1^{-1}F_1 + W_2 - F_2) \qquad \text{Mass effect} \qquad (14)$$

Flexibility effect

$$F_2 = (1/p^2)(1 + p\tau_2)\, D_2^{-1}(p^2Z_2 - \tilde{L}_2^{-1}\, p^2Z_3) \qquad (15)$$

$$p^2Z_i = G_i^{-1}(L_{i-1}^{-1}F_{i-1} + W_i - F_i) \qquad \text{Mass effect} \qquad (16)$$

Flexibility effect

$$F_i = (1/p^2)(1 + p\tau_i)\, D_i^{-1}(p^2Z_i - \tilde{L}_i^{-1}\, p^2Z_{i+1}) \qquad (17)$$

$$p^2Z_5 = G_5^{-1}(L_4^{-1}F_4 + W_5 - F_5) \qquad \text{Mass effect} \qquad (18)$$

$$F_5 = L_5\, W_6 \qquad \text{Lever arm effect} \qquad (19)$$

$$p^2Z_6 = \tilde{L}_5\, p^2Z_5 \qquad \text{Lever arm effect} \qquad (20)$$

Equations 13 through 20 describe completely the lumped model of Figure 2 by expressing all accelerations and internal forces dependent on external forces, thus satisfying the boundary conditions of a free body.

Since all the matrices G, D, and L (equations 4, 5, and 12) can be partitioned into similar diagonal matrices, the longitudinal components may be separated from the remaining components of the vectors F, W, and Z. The remaining components are of special interest and only these components will be simulated here because they contain the information (lateral and angular accelerations) utilized by the control system.

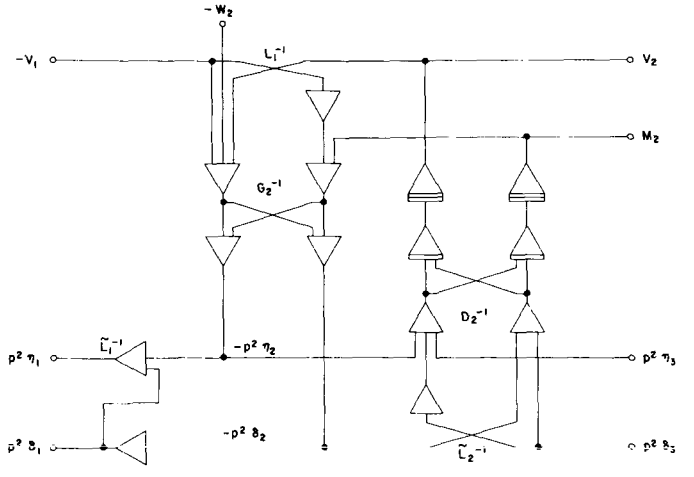

FIGURE 3. ANALOG COMPUTER DIAGRAM FOR STATIONS 1 THROUGH 3, EXCLUDING POTENTIOMETERS

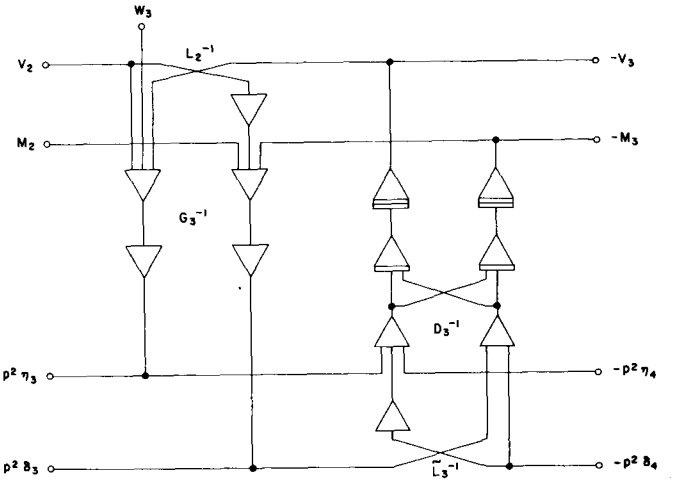

FIGURE 4. ANALOG COMPUTER DIAGRAM FOR STATIONS 2 THROUGH 4, EXCLUDING POTENTIOMETERS

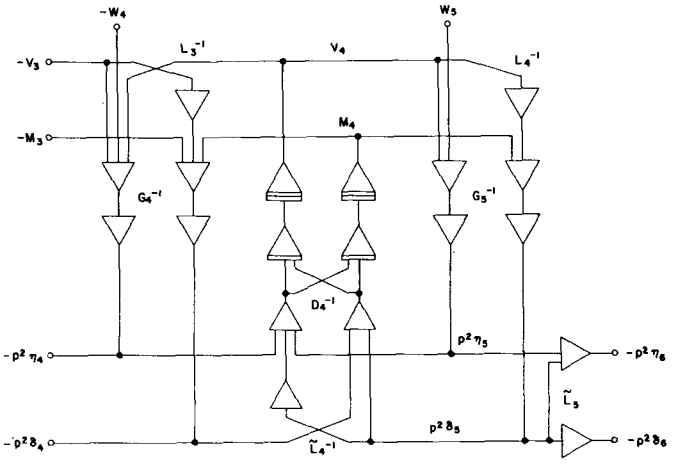

FIGURE 5. ANALOG COMPUTER DIAGRAM FOR STATIONS 3 THROUGH 6, EXCLUDING POTENTIOMETERS

Figures 3, 4, and 5 depict the arrangement of operational amplifiers and integrators programed to model the dynamic behavior of the Saturn V space vehicle. The integrators with the triple lines deviate from the usual integrator setup to include the time constant τ in their transfer function, $(1 + p\tau)/p$.

SIMULATION

The model program was realized on one analog computer AD-2-64-PBC. The variables were scaled properly to keep the amplifier gains between one and ten. Figure 6 shows how the cells were connected and where the signal generator was attached to simulate a shaker on the tail of the Saturn V vehicle. Figure 7 illustrates the arrangement of the electronic model together with the control system. Also indicated are interpolators to generate the lateral acceleration signals between the station pairs 2-3, 3-4, and 4-5, thus increasing the number of stations to 9. Nine acceleration signals and one force signal were displayed on an oscilloscope (Ref. 10) and recorded on Brush recorders. Photographs were made from the displayed mode shapes and traveling waves shown in Figures 8 through 11. The transfer function of the model (Figs. 12 and 13) was recorded by a frequency response analyzer (Industrial Measurement Corp.).

The photographs are self-explanatory. The mode shapes can be seen in Figure 8; however, for modes higher than the third, more points have to be used.

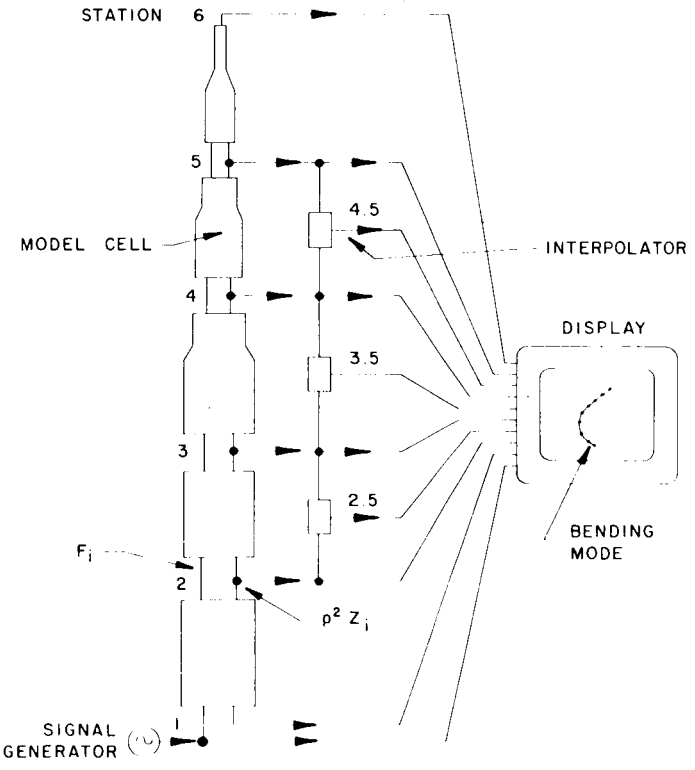

FIGURE 6. SIMULATION OF SATURN V MODEL WITH SIGNAL GENERATOR SIMULATING A SHAKER

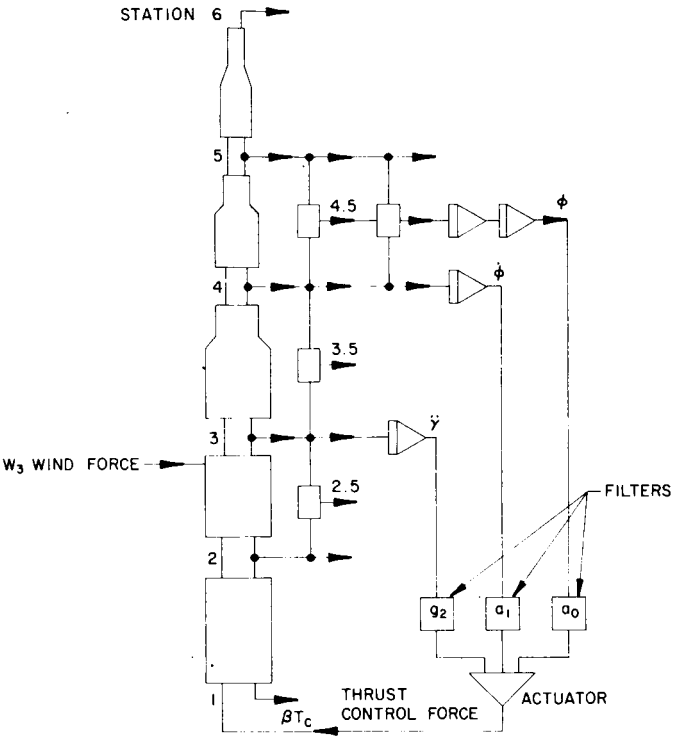

FIGURE 7. SIMULATION OF SATURN V MODEL WITH ATTITUDE STABILIZATION LOOP CLOSED -- EXCITED BY UNIT STEP WIND

The "0" mode is the acceleration distribution for a steady force at the tail (it has one node, which is the center of rotation). All photographs were taken for a vehicle at 40 seconds flight time and the bending mode frequencies were 1.08, 2.06, and 3.05 Hz, thus being 4.5, 8, and 4 percent above the values of officially available digital data (Ref. 11).

Of special interest is Figure 9, which shows a disturbance traveling through the 105 m length of the Saturn V vehicle. The velocity is apparently 210 ms^{-1} and agrees well with the first bending mode resonance considerations. About half the time is required for a disturbance starting at the center of pressure (Fig. 10).

The photographs shown in Figures 10 and 11 are the traveling waves excited by a unit step wind force at the center of pressure while the attitude of the whole vehicle model is stabilized by a control loop (Fig. 7). Here it is obvious that the disturbance rings out faster, indicating the damping of the first bending mode by the control system. The photograph at 10 seconds after the excitation at the center of pressure

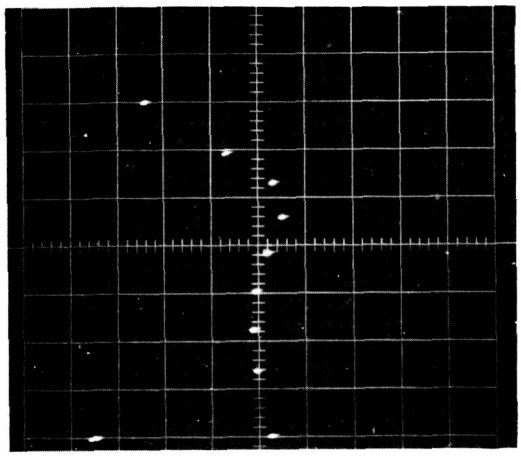

2ND MODE ACCELERATION EXCITED BY SINUSOIDAL FORCE OF 2×10^5 N_{pp} AT THE TAIL .

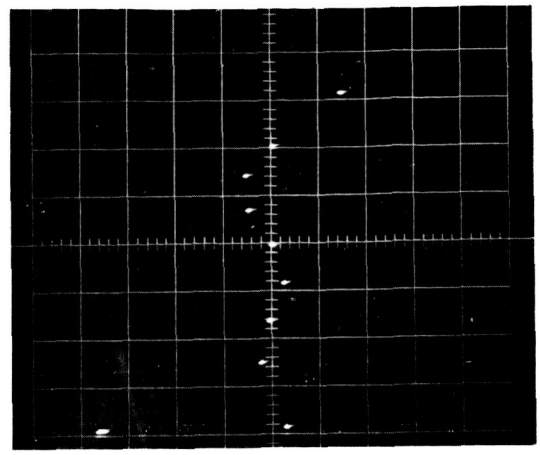

3RD MODE ACCELERATION EXCITED BY SINUSOIDAL FORCE OF 4×10^5 N_{pp} AT THE TAIL.

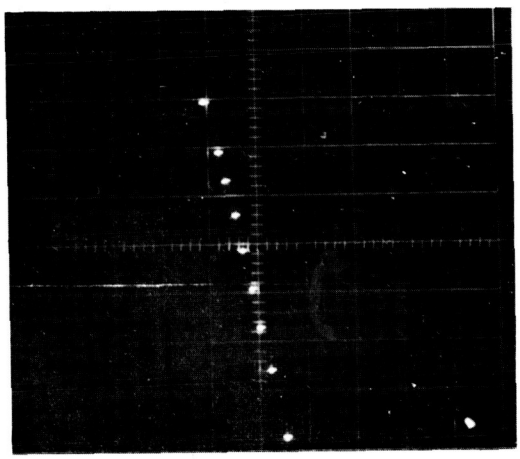

"0" MODE ACCELERATION EXCITED BY UNIT STEP FORCE OF 2.2×10^6 N AT THE TAIL PUSHING TO RIGHT AND TAKEN 70 s AFTER STEP STARTED.

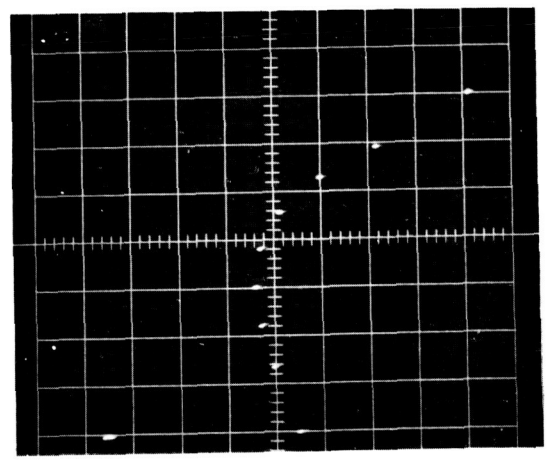

1ST MODE ACCELERATION EXCITED BY SINUSOIDAL FORCE OF $2 \times 10^5 N_{pp}$ AT THE TAIL OF SA–V MODEL.

FIGURE 8. MODE SHAPES OF ACCELERATIONS PERPENDICULAR TO AXIS OF SATURN V MODEL. UNITS: VERTICAL, 15 m/div; HORIZONTAL, 5 m/s^2/div.

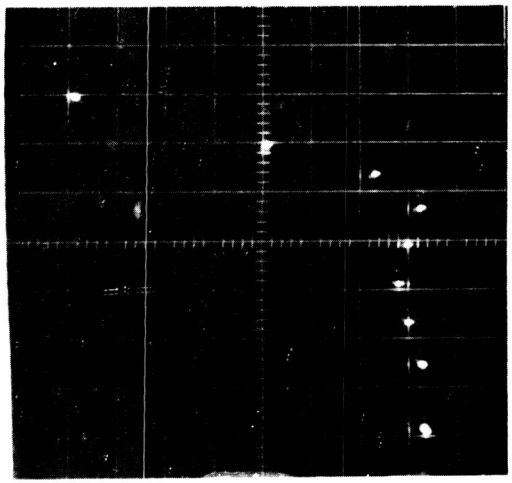

500 ms ▲

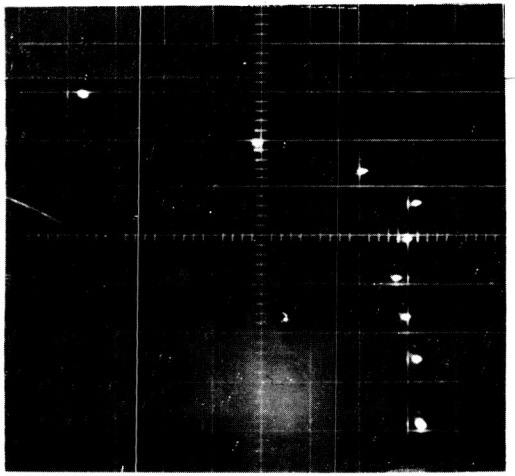

450 ms ▲

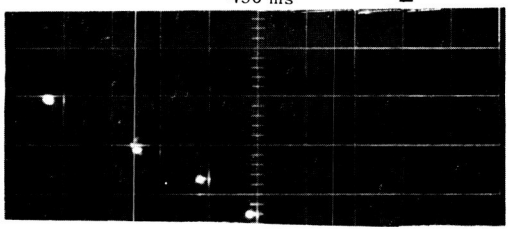

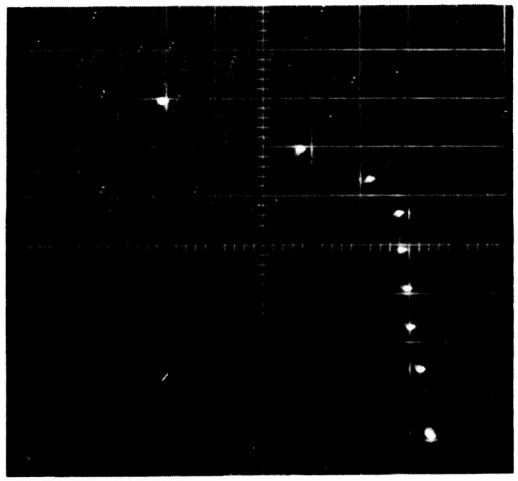

550 ms ▲

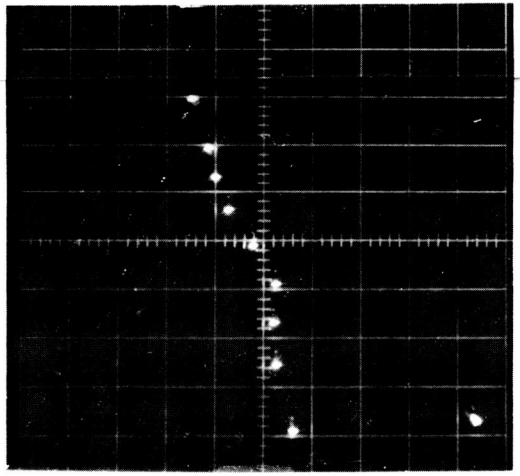

600 ms

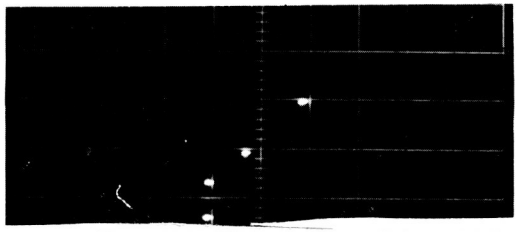

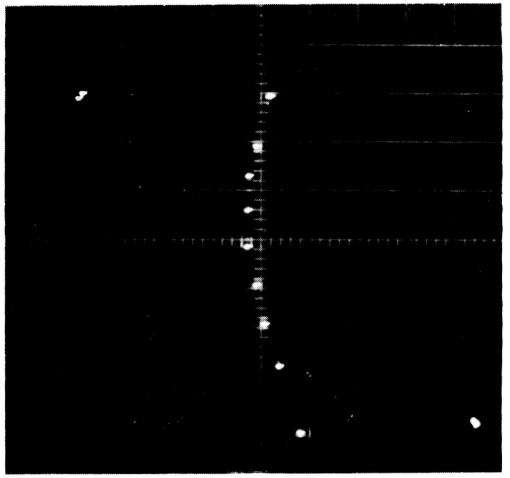

10 s

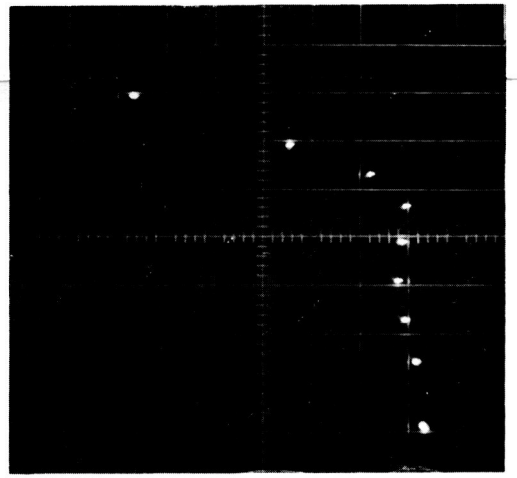

1450 ms ▲

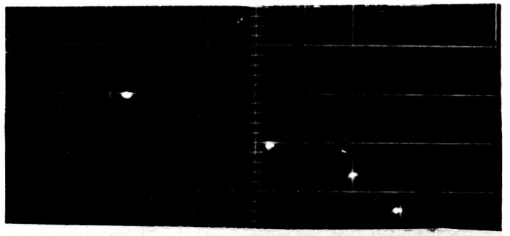

52-2

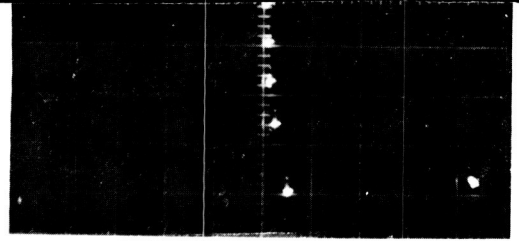

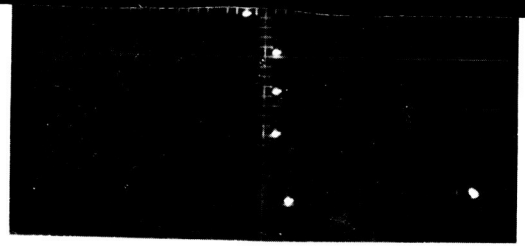

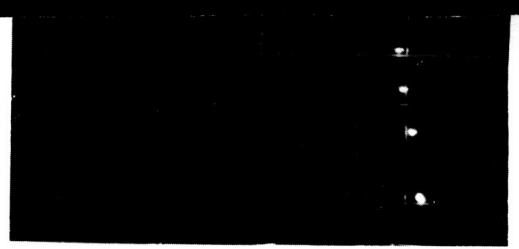

400 ms

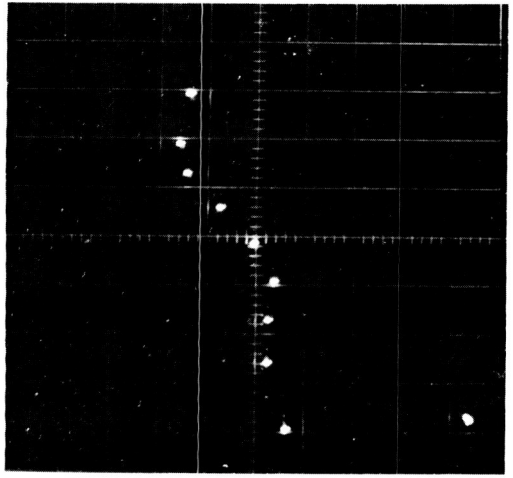

650 ms

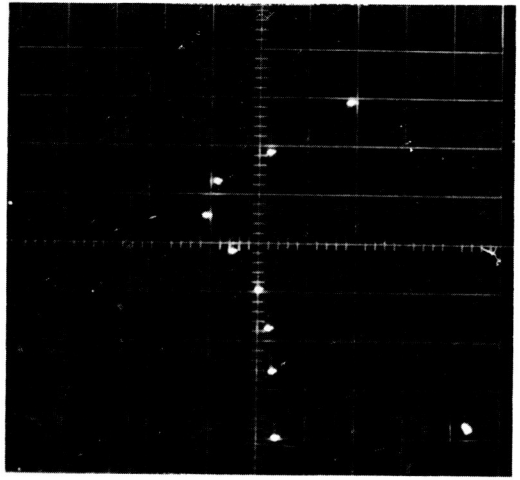

1400 ms

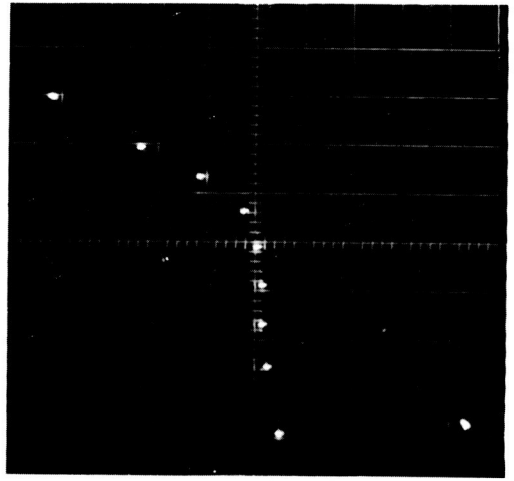

350 ms

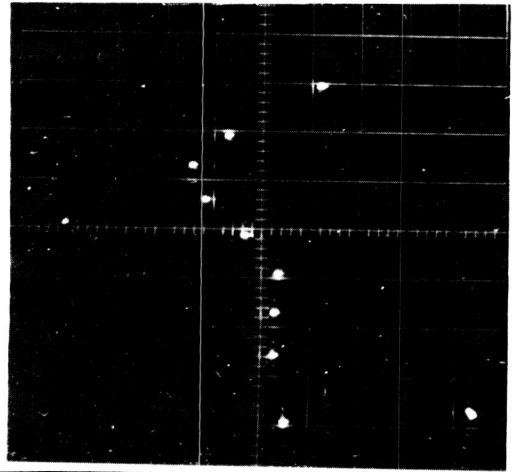

700 ms

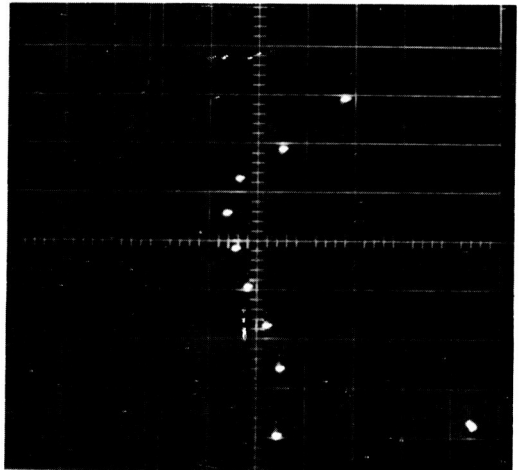

1350 ms

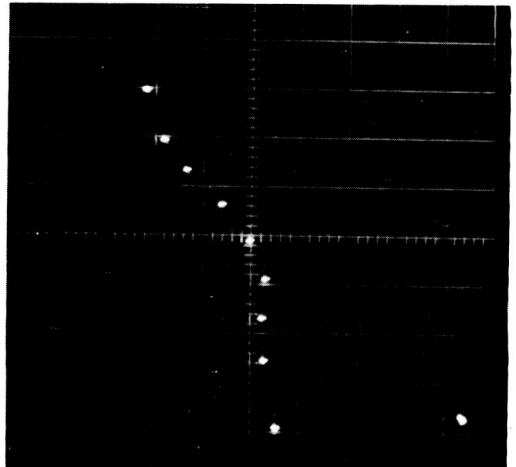

50-3

300 ms

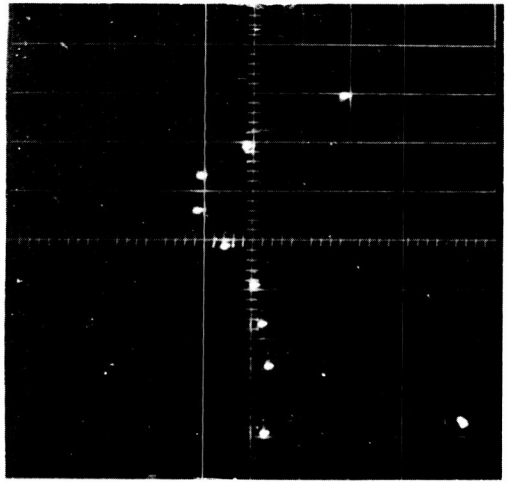

750 ms

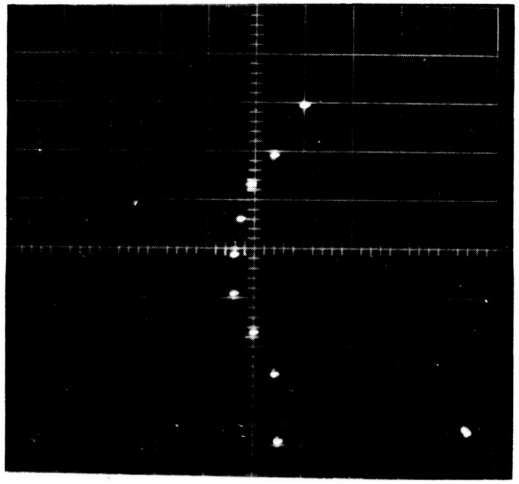

1300 ms

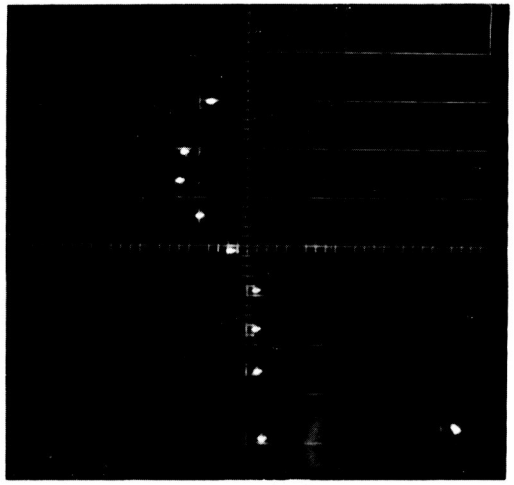

250 ms

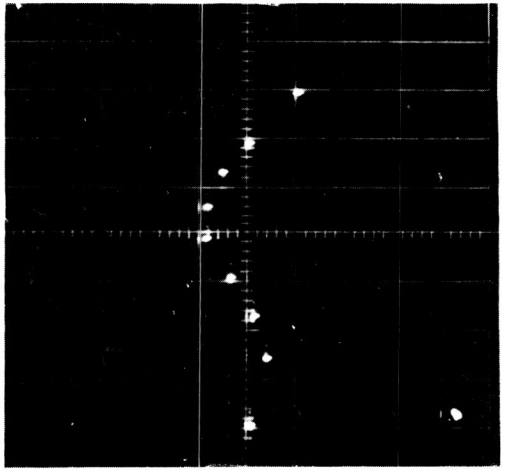

800 ms

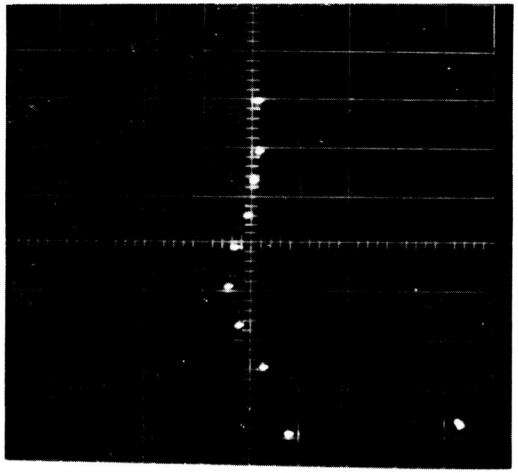

1250 ms

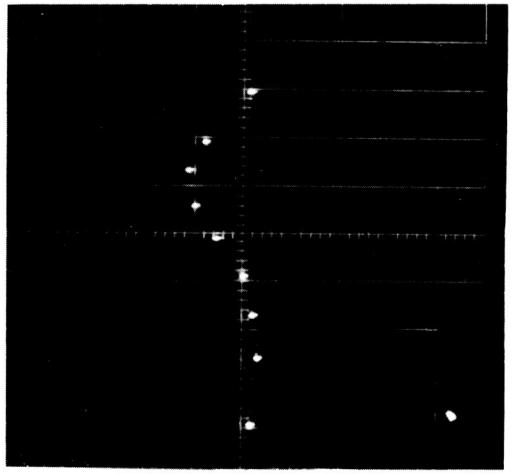

200 ms

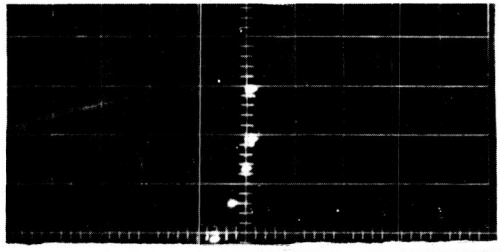

850 ms

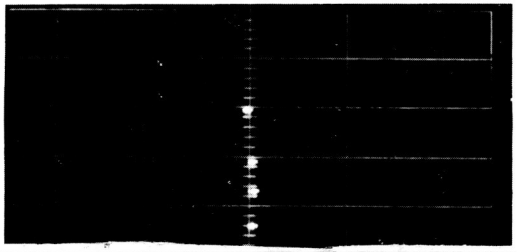

1200 ms

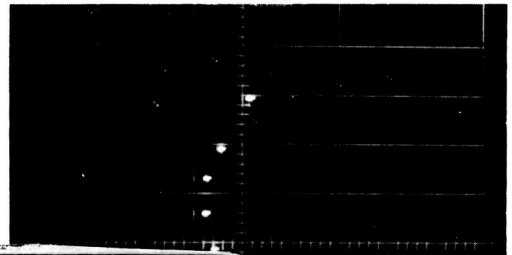

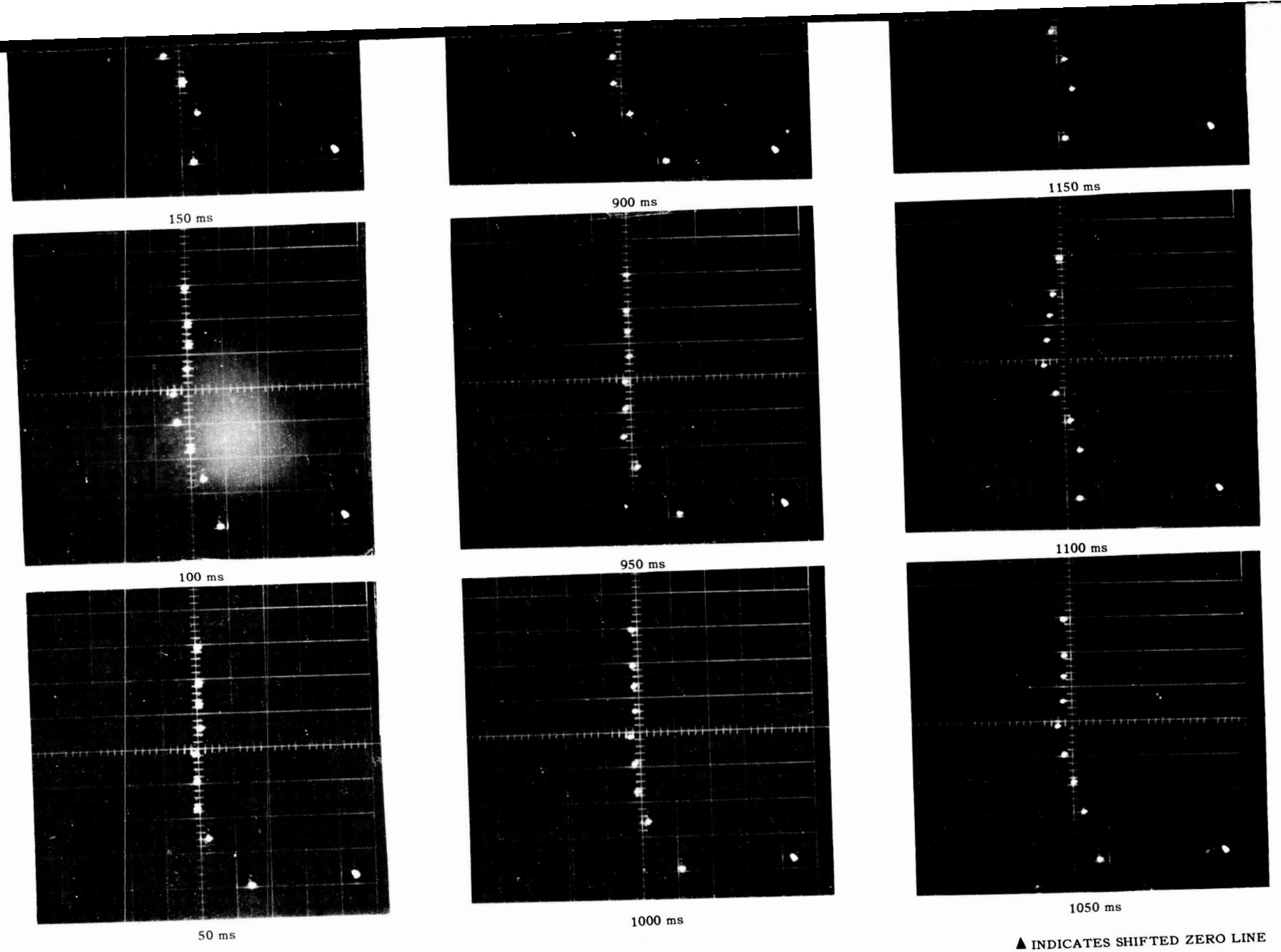

FIGURE 9. TRAVELING WAVE EXCITED BY A UNIT STEP FORCE AT THE TAIL OF SA–V MODEL. UNITS: VERTICAL, 15 m/div; HORIZONTAL, 5 m/s^2/div; LATERAL TAIL FORCE, 5 x 10^5 N/div.

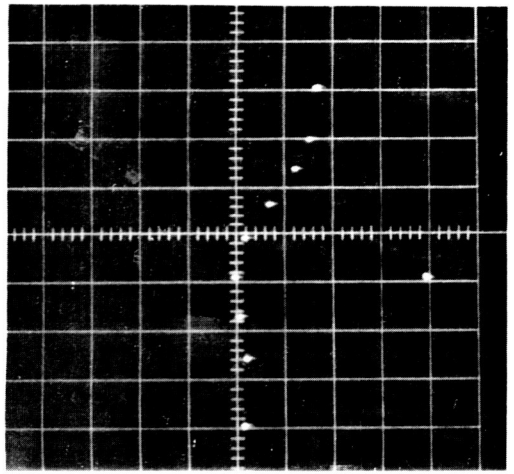

500 ms

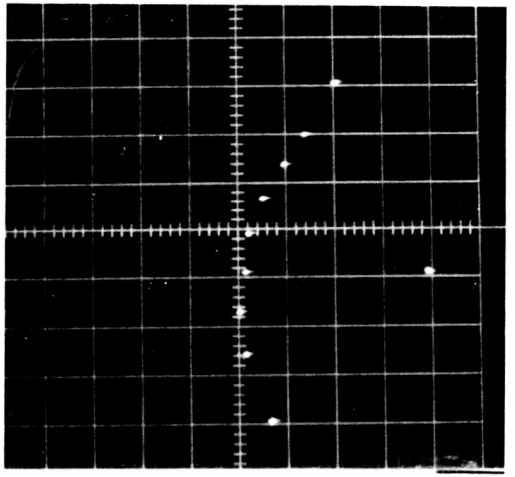

550 ms

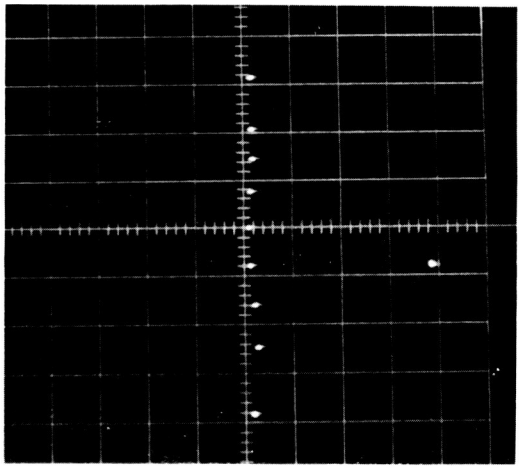

1500 ms

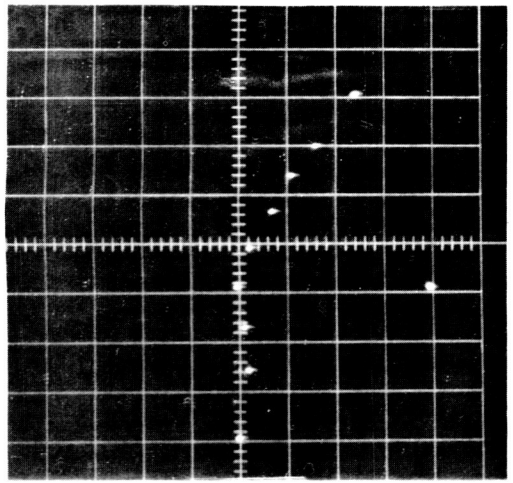

450 ms

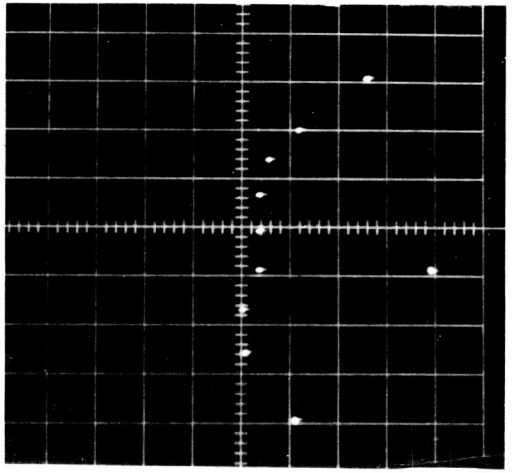

600 ms

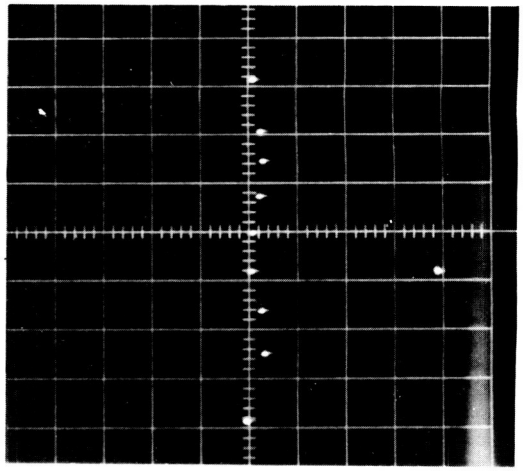

1450 ms

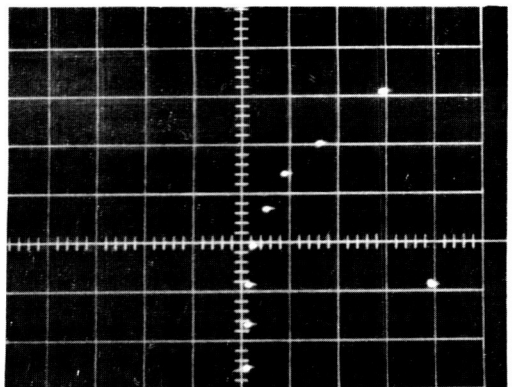

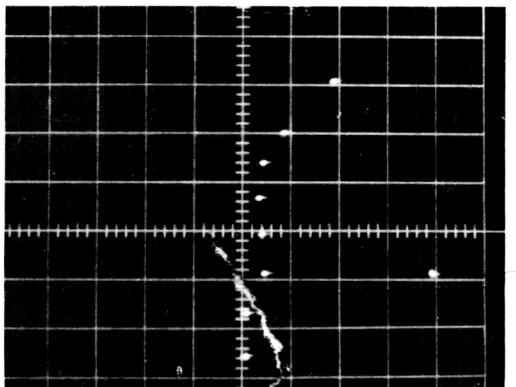

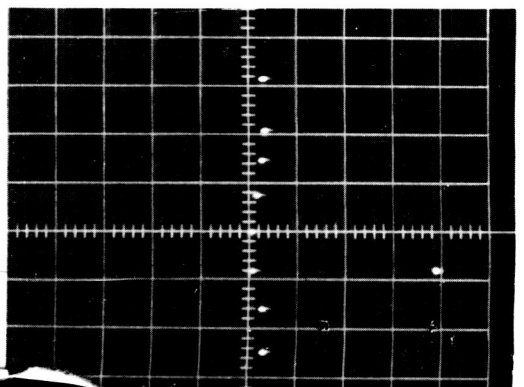

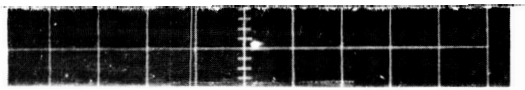

400 ms

650 ms

1400 ms

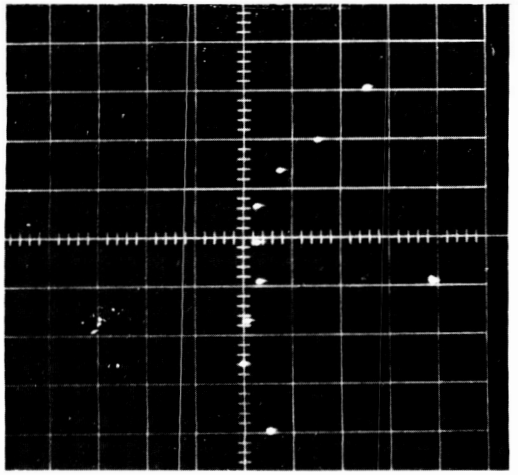

350 ms

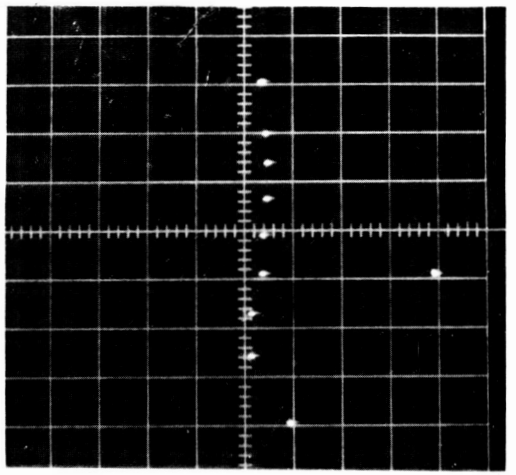

700 ms

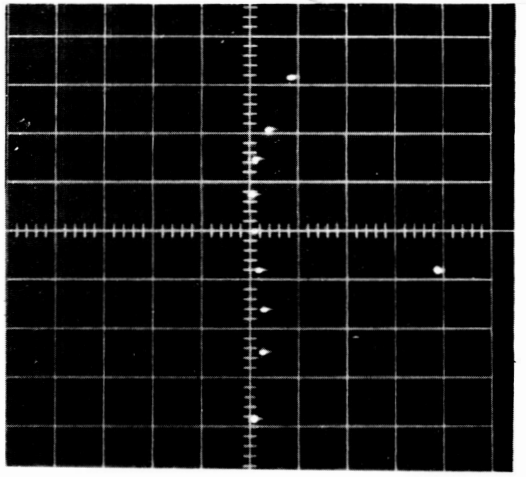

1350 ms

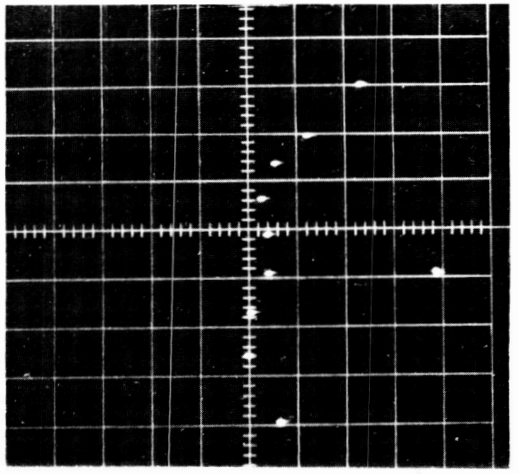

300 ms

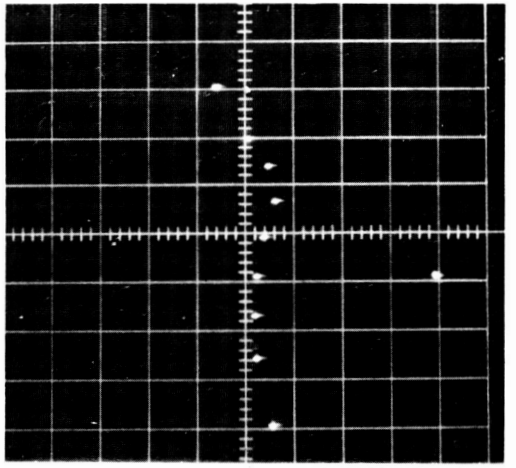

750 ms

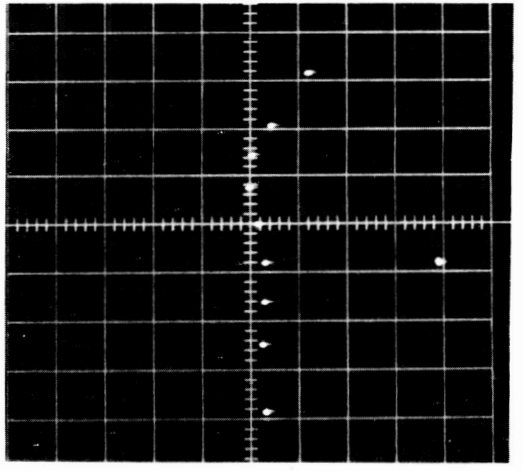

1300 ms

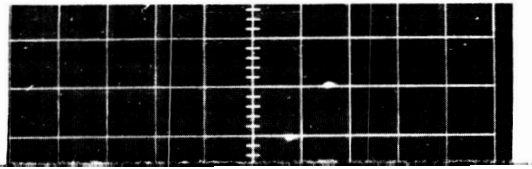

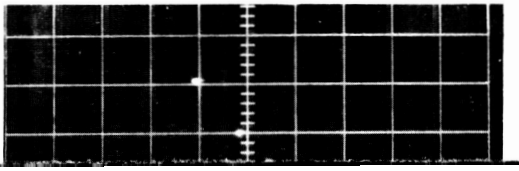

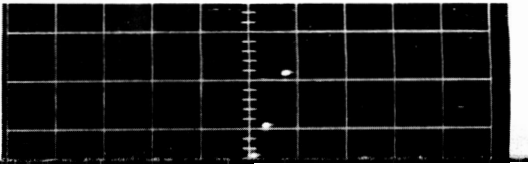

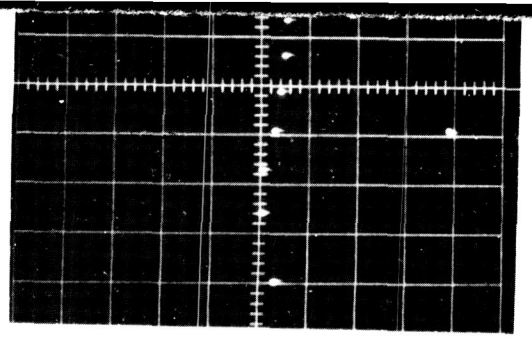

250 ms

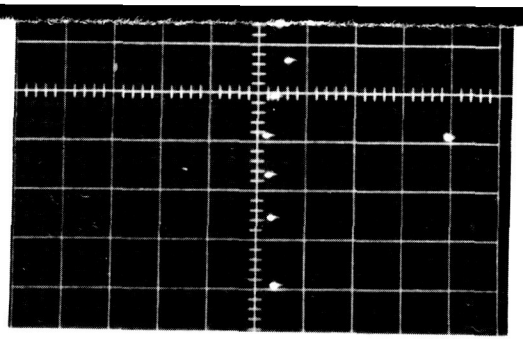

800 ms

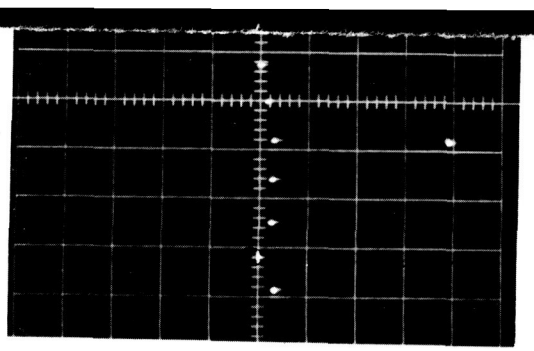

1250 ms

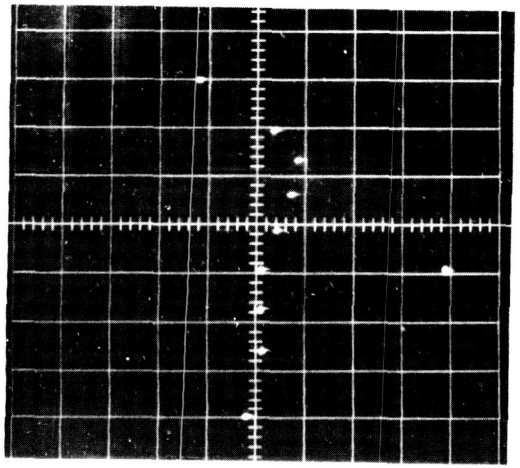

200 ms

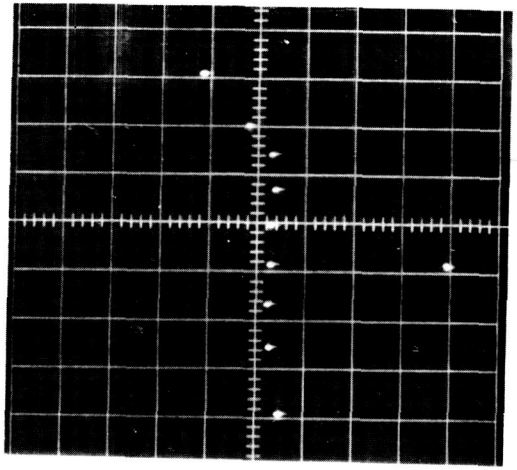

850 ms

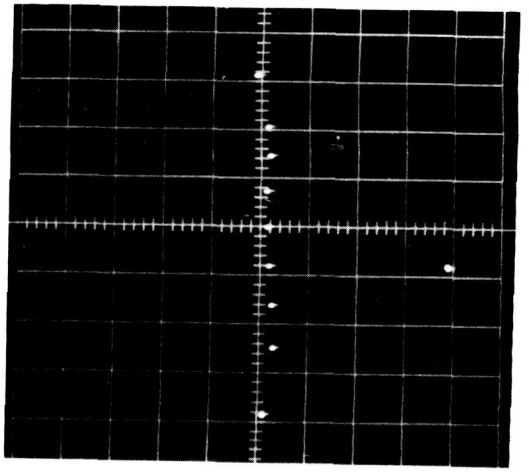

1200 ms

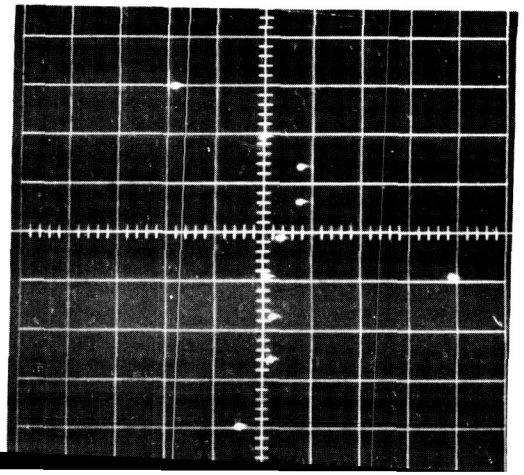

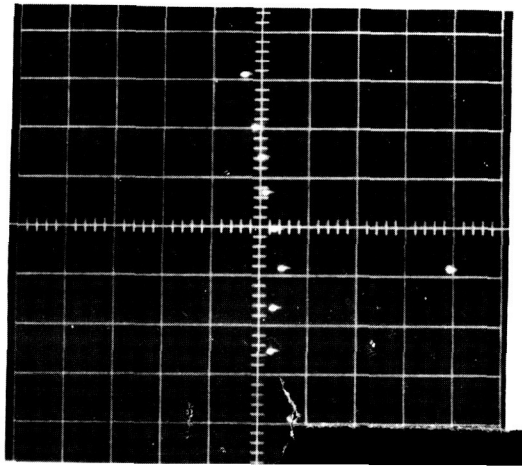

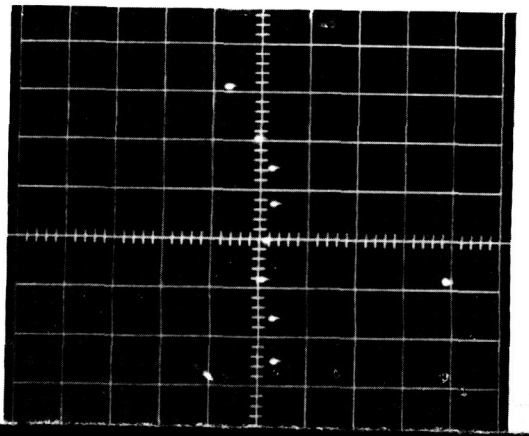

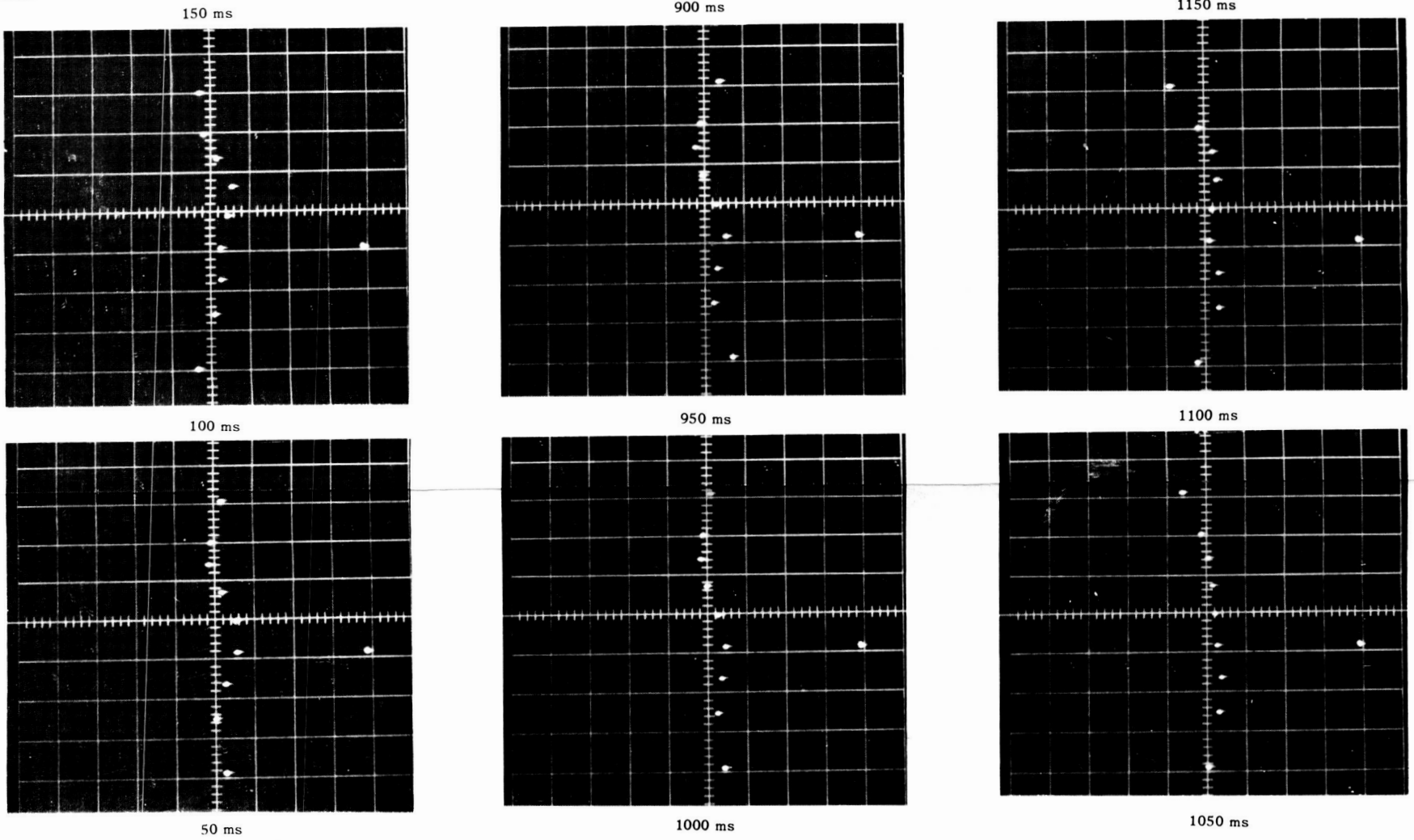

FIGURE 10. TRAVELING WAVE EXCITED BY A UNIT STEP FORCE NEAR CENTER OF PRESSURE (FOURTH POINT UP INCLUDING THE TAIL POINT) OF THE SA–V MODEL. UNITS: VERTICAL, 15 m/div; HORIZONTAL, 5 m/s^2/div; LATERAL STEP FORCE, 5 x 10^5 N/div.

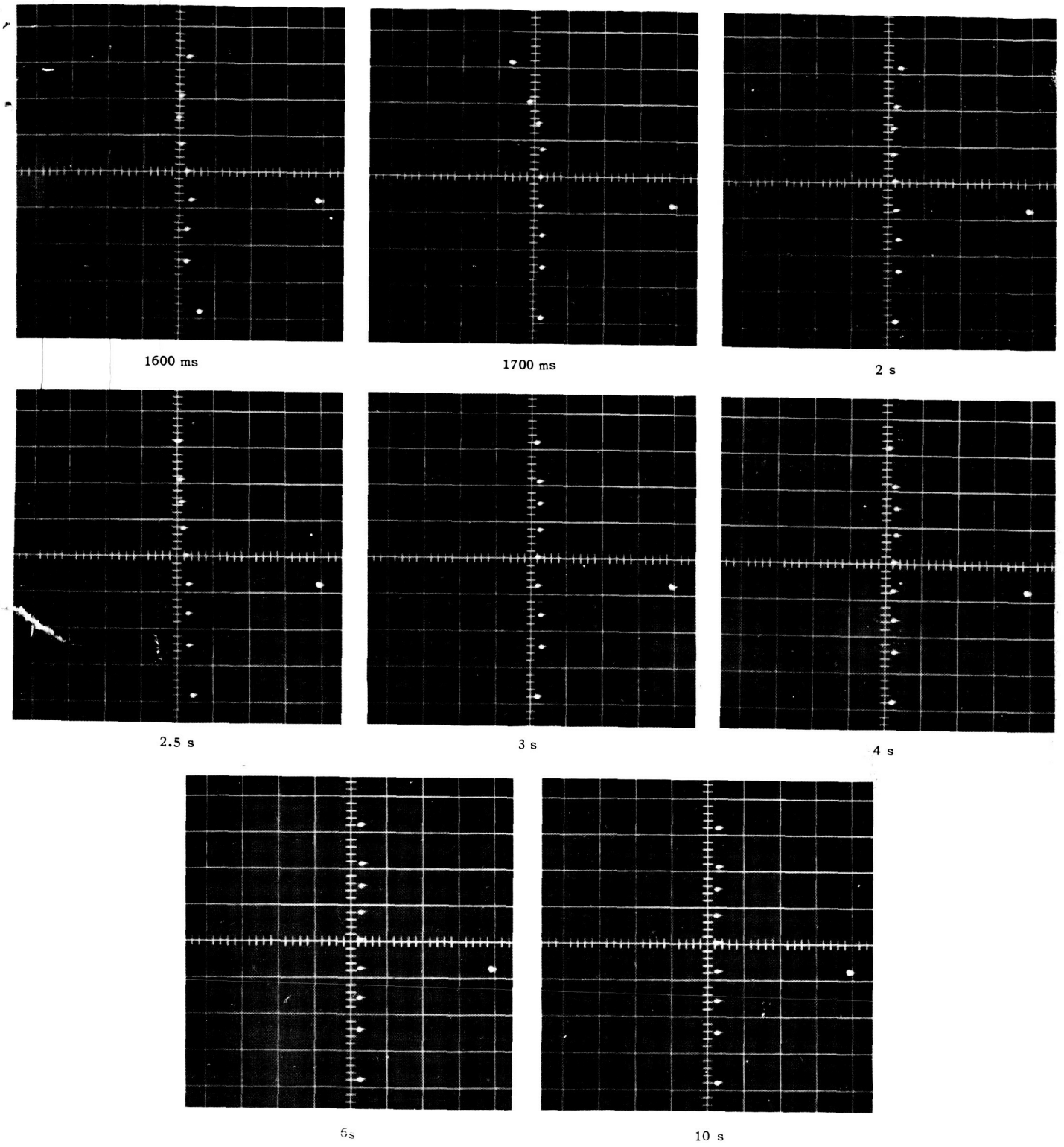

FIGURE 11. TRAVELING WAVE EXCITED BY A UNIT STEP FORCE NEAR CENTER OF PRESSURE (FOURTH POINT UP INCLUDING THE TAIL POINT) OF SA–V MODEL. UNITS: VERTICAL, 15 m/div; HORIZONTAL, 5m/s^2/div; LATERAL STEP FORCE, 5 x 10^5 N/div. MAX. DELAY TIME 10 s.

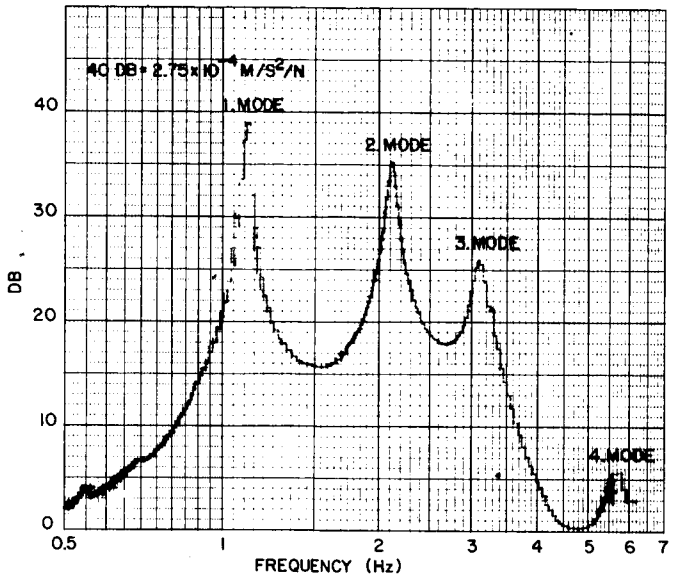

FIGURE 12. FREQUENCY RESPONSE OF THE RATIO: NOSE ACCELERATION TO TAIL FORCE OF SATURN V MODEL AT 40 SECONDS FLIGHT TIME

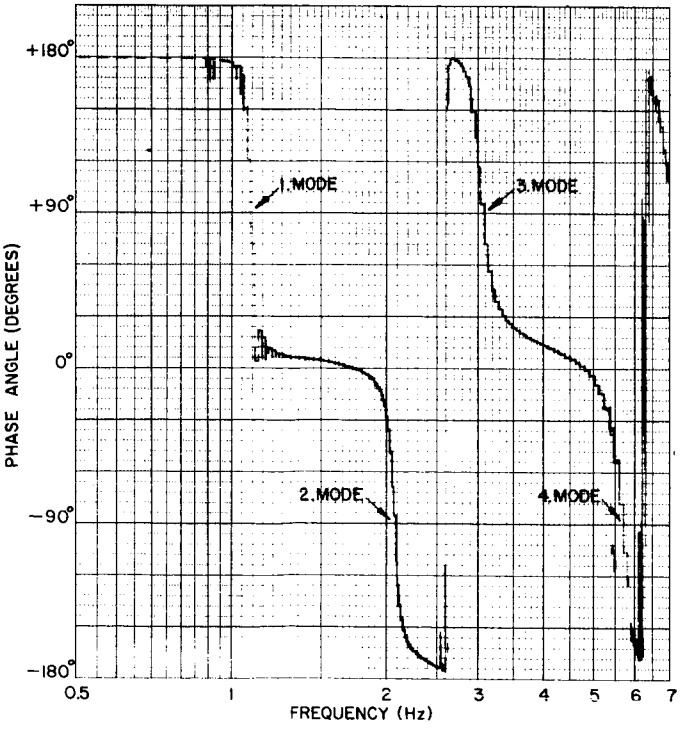

FIGURE 13. FREQUENCY RESPONSE OF THE PHASE ANGLE: NOSE ACCELERATION TO TAIL FORCE OF SATURN V MODEL AT 40 SECONDS FLIGHT TIME

clearly shows how the vehicle accelerates to the right, pushed by the wind and the attitude stabilizing component of the thrust. At 10 seconds the rotation of the vehicle has completely stopped and only a lateral drifting prevails.

The recordings in Figures 12 and 13 show the transfer function of the model for the signal ratio of nose acceleration to the tail excitation force. Note the four resonances with increasing damping towards the higher frequencies. The critical damping factors were approximately 1, 2, 3, and 6 percent.

CONCLUSIONS

An electronic model of a flexible space vehicle was successfully used for simulation of traveling wave effects, bending modes, rigid body motions, and transfer functions. It promises to be a good tool to gain better insight in the dynamic behavior of flexible space vehicles. It is a very efficient method to simulate with real hardware, especially if it is necessary to vary structural vehicle parameters. Available analog computers can be used, thus demonstrating the great versatility of the model.

REFERENCES

1. Pipes, Louis A.; Applied Mathematics for Engineers and Physicists, McGraw-Hill Book Co., Inc., pp. 76-100, 217-238, 266-272, 1958.

2. Timoshenko, S.; Vibration Problems in Engineering, D. Van Nostrand Co., Inc., pp. 24-40, 380-385, 1961.

3. Rheinfurth, Mario H.; Modified Stodola Method Including Rotating Inertia and Shear Flexibility, DA Technical Report No. 4-59, ABMA Redstone Arsenal, Alabama, April 8, 1959.

4. Ernsberger, Gale R.; Dynamic Test Results of SAD-6, NASA TM X-53029, Huntsville, Alabama, April 6, 1964.

5. Howe, R. M. and Haneman, V. S., Jr.; The Solution of Partial Differential Equations by Difference Methods Using the Electronic Differential Analyzer, Proceedings of the IRE, pp. 1497-1508, October 1953.

6. Hughes, W. G. and Squires, M.; An Electronic Analogue for Investigating Structural Vibrations in Unsupported Elastic Beams, Technical Note No. G. W. 537, Royal Aircraft Establishment, Farnborough, England, U. D. C. No. 534.131: 531.224.8:5.001.58: 681.3.02, March 1960.

7. Greenwood, D. T.; The Use of Higher-Order Difference Methods in Beam Vibration Analysis, NASA TN D-964, University of Michigan, Ann Arbor, December 1961.

8. MacKay, D. M. and Fisher, M. E.; Analogue Computing at Ultra-High Speed, John Wiley and Sons, Inc., New York, 1962.

9. MacNeal, R. H.; Electric Circuit Analogies for Elastic Structures, Vol. 2, John Wiley and Sons, Inc., New York, 1962.

10. Elms, Charles; Signal Conditioning Circuit For An Oscilloscope Display of Bending, contained in this report.

11. Pack, Homer; Vibration Analysis of Saturn V LOR, MSFC Internal Note R-AERO-1-64, Huntsville, Alabama, January 6, 1964.

F. CONSTRUCTION OF ELASTIC BODY MODELS FROM SATURN DYNAMIC TEST RESULTS

by John H. George and Maurice E. Singley

ABST

This article presents a mathematical procedure for obtaining mathematical models for dynamic systems. This procedure was used to obtain mathematical models of the elastic body dynamics for Saturn cluster mode vehicles.

Theoretical procedures were not available for adequately describing the elastic body dynamics. For this reason, it was necessary to utilize this procedure for obtaining mathematical models directly from test data. Examples were taken from flight vehicle dynamic testing.

AUTHOR

INTRODUCTION

During the early days of Saturn research and development, it was necessary to supplement the theoretical elastic body data by a dynamic test program. The dynamic test results were to determine local effects, non-planar coupling, and structural damping that were not given or explained by theoretical considerations. A method was needed that would convert dynamic test data into a mathematical model of the flexible vehicle dynamics, including the complicated multiple tank behavior of the Saturn vehicle.

The procedure described in this article was devised to convert empirical frequency response data obtained from the Saturn dynamic test program into a mathematical model describing elastic body behavior. The technique was derived in general and is valid for any station of the vehicle, with the accuracy depending only upon the input data. The resulting mathematical model includes all local effects, coupling, damping, and the effects of multiple tank behavior. The mathematical models obtained by this procedure were used in the design, synthesis, analysis, and final checkout of control systems of the Saturn SA-5, SA-6, and SA-7 flight vehicles.

NOMENCLATURE

φ_x	angular deflection at station x, deg
F	force input, N
φ_{iu}	angular deflection at station x caused by the u^{th} bending component, deg
M_u	gain term obtained by partial fraction expansion of the u^{th} bending component, deg/s^2-N
N_u	lead term obtained by the partial fraction expansion of the u^{th} bending component, deg/s-N
ζ_u	damping ratio associated with the u^{th} bending component
ω_u	circular frequency of u^{th} bending component, 1/s
$\dot{\varphi}_{ia}$	amplitude of angular velocity at station x, deg/s
$\dot{\varphi}_{ip}$	phase of angular velocity at station x referenced to the oscillator, deg
F_a	amplitude of load cell force, N
F_p	phase of load cell referenced to the oscillator, deg

MATHEMATICAL MODEL CONCEPT

In general, any transfer function may be written as a ratio of polynomials,

$$\frac{\varphi_i(s)}{F(s)} = \frac{a_o + a_1 s + \ldots + a_n s^n}{b_o + b_1 s + \ldots + b_{2m} s^{2m}} \qquad n \le 2m \qquad (1)$$

where the exponents of the polynomials, n and m, are determined by the order and the coupling of the physical system. Expanding equation 1 by a standard partial fraction expansion and assuming only complex zeros in the denominator yield the normal mode form of the transfer function as

$$\frac{\varphi_i(s)}{F(s)} = \sum_{u=1}^{m} \frac{M_u + N_u s}{s^2 + 2\zeta_u \omega_u s + \omega_u^2}. \quad (2)$$

The second order ordinary differential equation of the elastic body behavior caused by the first m bending modes may be obtained from equation 2 by taking the inverse Laplace transformation,

$$\ddot{\varphi}_{iu} + 2\zeta_u \omega_u \dot{\varphi}_{iu} + \omega_u^2 \varphi_{iu} = M_u F + N_u \dot{F} \quad (3)$$

$$u = 1, 2, \ldots, m.$$

The coefficients of equations 2 and 3 are constructed from the dynamic test frequency response data using the following method.

The input force, measured by a load cell, is recorded as an amplitude F_a and a phase F_p. The output $\dot{\varphi}_i$ of a rate gyro at station i has an amplitude $\dot{\varphi}_{ia}$ and $\dot{\varphi}_{ip}$. The amplitude function is calculated from the dynamic test data as

$$\left(\frac{\varphi_i}{F}\right)_a = \frac{\dot{\varphi}_{ia}}{F_a \omega}, \quad (4)$$

where $\omega = 2\pi f$ and f is the frequency of the forcing function. The phase relationship is obtained from the expression

$$\left(\frac{\varphi_i}{F}\right)_p = \dot{\varphi}_{ip} - (F_p + 90°). \quad (5)$$

This numerical transfer function is used as an input to Levy's curve fit routine (Refs. 1 and 2) which has as an output a ratio of polynomials, or a transfer function, in the form of equation 1. This is expanded by a partial fraction expansion method to produce equation 2.

SATURN DYNAMIC TEST

A typical dynamic test vehicle with test instrumentation is shown in Figure 1. The vehicle is suspended in the dynamic test tower by a network of cables attached to the fins at one end and to the test tower through a spring package at the other. The number of springs in each package may be varied for different suspension effects for each simulated time of flight. Currently two different spring configurations are being used for each simulated time of flight.

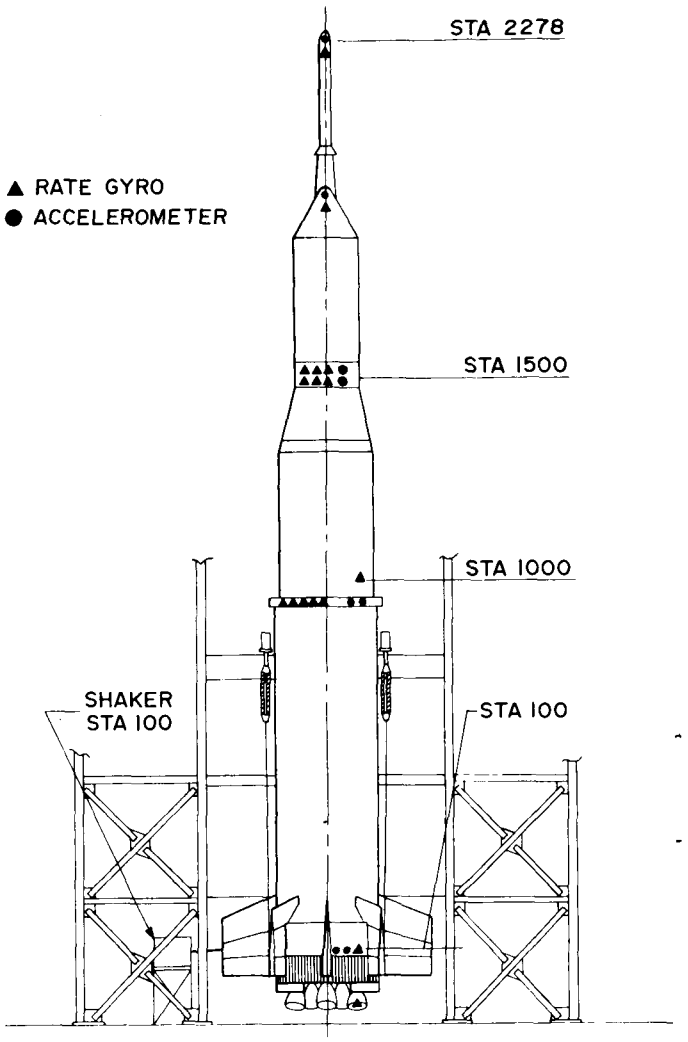

FIGURE 1. DYNAMIC TEST SETUP

The input force is applied at the engine swivel point (Fig. 1) and is sinusoidal with a frequency that is controlled by a crystal oscillator (Ref. 3).

The flow of data from the dynamic test to a form that is usable by the control system design and synthesis group is shown in Figure 2. The output of the load cell, the oscillator, and each of the sensors on the dynamic test vehicle is recorded on digital tape and strip charts. A primary reduction is performed on the digital tape and the printout is compared with the strip charts for determining unusual wave shapes, proper instrument polarity, and correct calibration. The results of this comparison are reported to the operations group, who make the appropriate changes.

A secondary reduction is performed on the digital

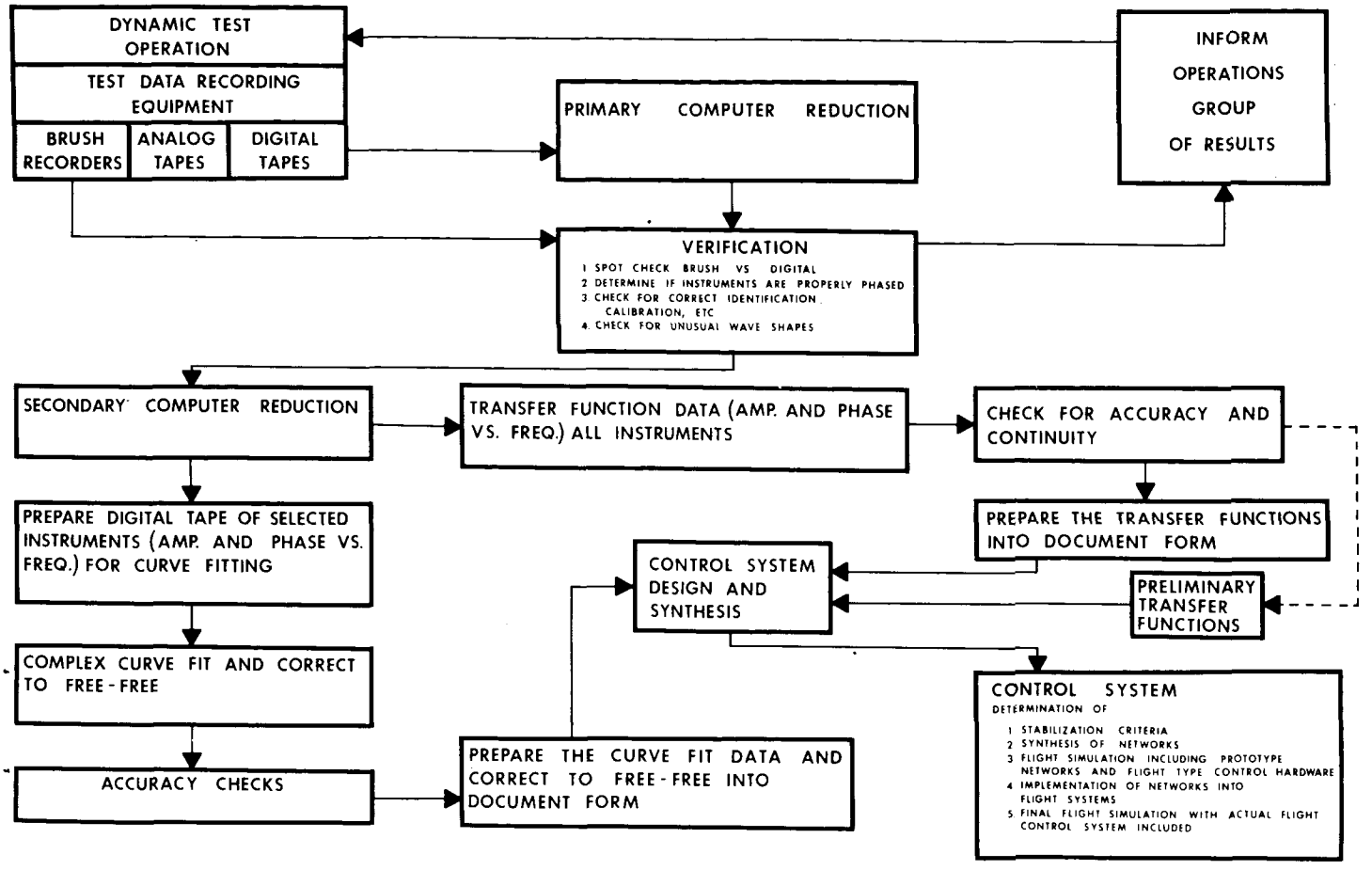

FIGURE 2. DYNAMIC TEST DATA FLOW DIAGRAM

tape yielding; (a) frequency response data of the form of equations 4 and 5, and (b) computer tape of the frequency response of certain selected instruments. The frequency response data from (a) are documented. The tape from (b) is used as an input to Levy's curve fit routine and expanded by the partial fraction method, thereby yielding a mathematical model matching the amplitude and phase of the elastic vehicle response in the sense of least squares (Fig. 3).

A linear extrapolation is performed by considering the bending model coefficients versus the number of springs in the two different suspension systems for each simulated time of flight. The bending model coefficients found by extrapolation characterize a suspensionless vehicle which approximates a free-free system.

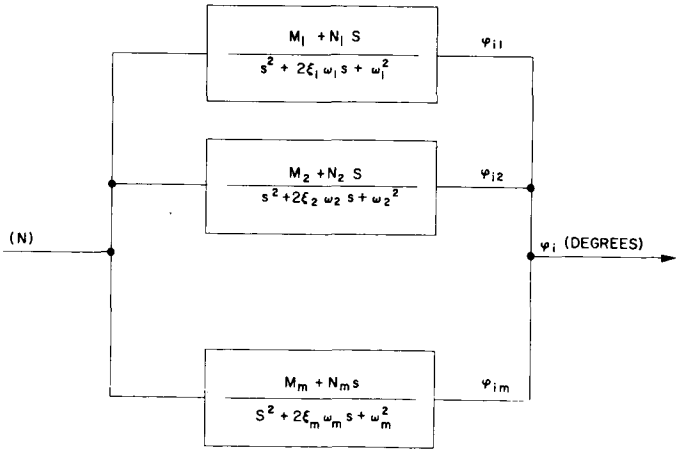

FIGURE 3. MATHEMATICAL MODEL

APPLICATION TO SATURN DYNAMIC TEST

Tables 1, 2, and 3 and Figures 4 through 9 typify results obtained during dynamic testing of the Saturn dynamic test vehicle. The coefficients (Tables 1, 2, and 3) were computed using the procedure outlined in the preceding section. They describe the first four modes, as measured from the exciting force at the tail to a rate gyro mounted in the instrument compartment. Table 1 shows the computed coefficients for the test using 8 supporting cables and 12 springs. Table 2 shows the computed coefficients for the test case using 8 supporting cables and 8 springs. Table 3 shows the coefficients obtained by linear extrapolation to the free-free case. Figures 4 through 7 are comparisons of the frequency response functions computed from the

TABLE 1. BENDING MODEL COEFFICIENTS USED IN FIGURES 4 AND 5.

f	ξ	M	N
1.73	0.0104	8.69	-0.0459
3.27	0.0080	1.75	0.0142
4.64	0.0065	-7.37	0.0063
5.31	0.0045	2.39	0.0396

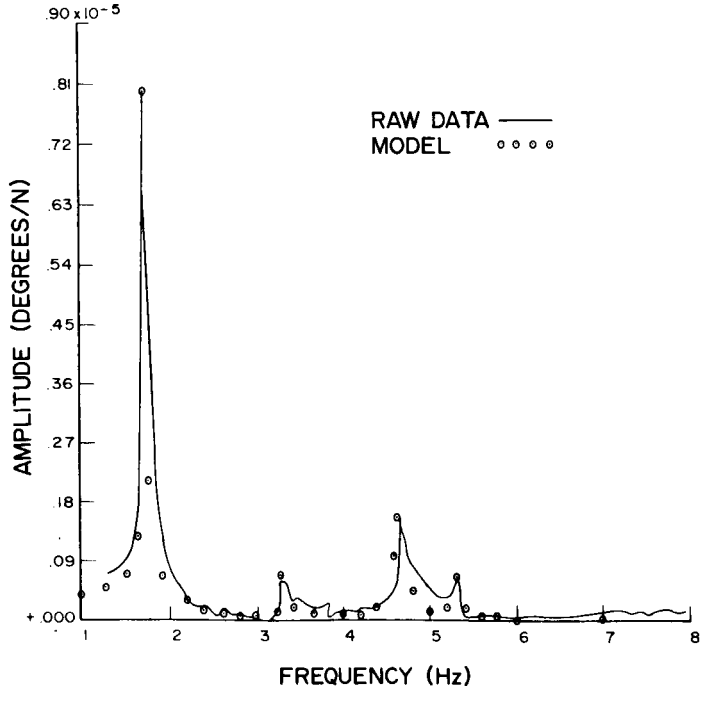

FIGURE 4. AMPLITUDE FUNCTION COMPARISON, HARD SUSPENSION

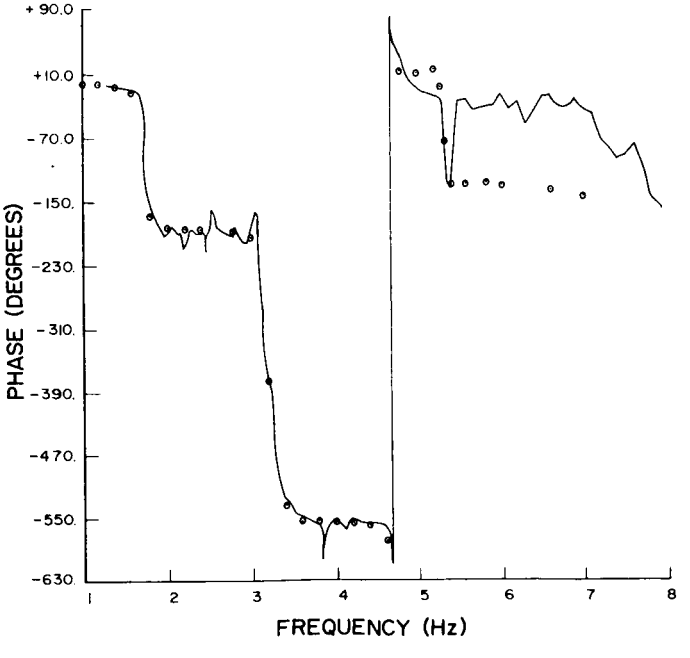

FIGURE 5. PHASE FUNCTION COMPARISON, HARD SUSPENSION

models of Tables 1 and 2 with respect to the original measured data. Figures 8 and 9 are frequency response functions of the model given in Table 3.

Extrapolation from a vehicle with soft suspension to a suspensionless vehicle resulted in an average modal frequency shift of less than 1 percent. The resulting change of the gain associated with each modal frequency averaged less than 30 percent. The example cited from the Saturn SA-6 dynamic test had an average frequency shift of .74 percent and gain change of 15.1 percent.

TABLE 2. BENDING MODEL COEFFICIENTS USED IN FIGURES 6 AND 7.

f	ξ	M	N
1.74	0.0101	9.13	-0.0351
3.28	0.0070	1.68	0.0073
4.65	0.0063	-7.81	0.0386
5.30	0.0045	2.21	0.0199

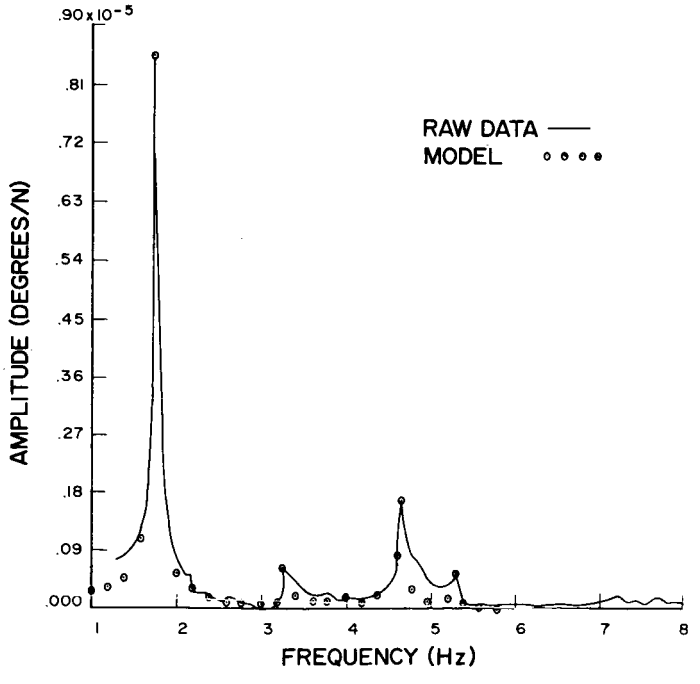

FIGURE 6. AMPLITUDE FUNCTION COMPARISON, SOFT SUSPENSION

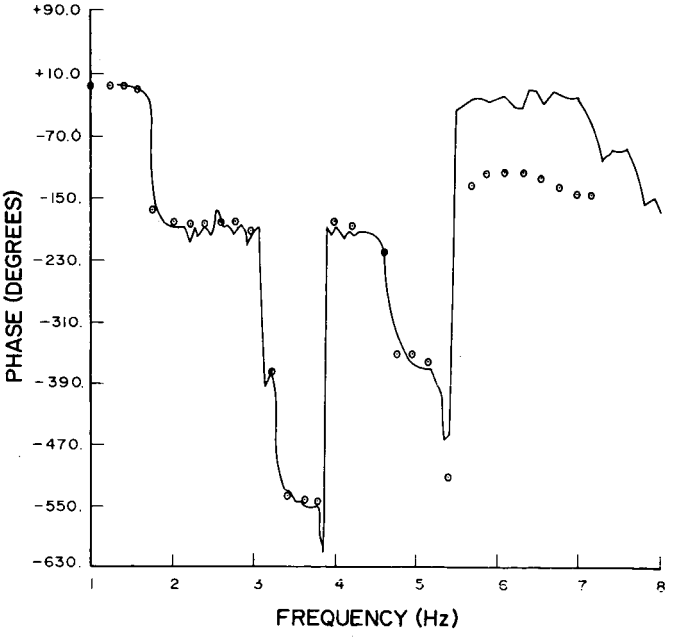

FIGURE 7. PHASE FUNCTION COMPARISON, SOFT SUSPENSION

TABLE 3. BENDING MODEL COEFFICIENTS USED IN FIGURES 8 AND 9.

f	ξ	M	N
1.76	0.0101	10.01	-0.0135
3.30	0.0070	1.54	-0.0065
4.67	0.0063	-8.69	0.1032
5.28	0.0045	1.85	-0.0195

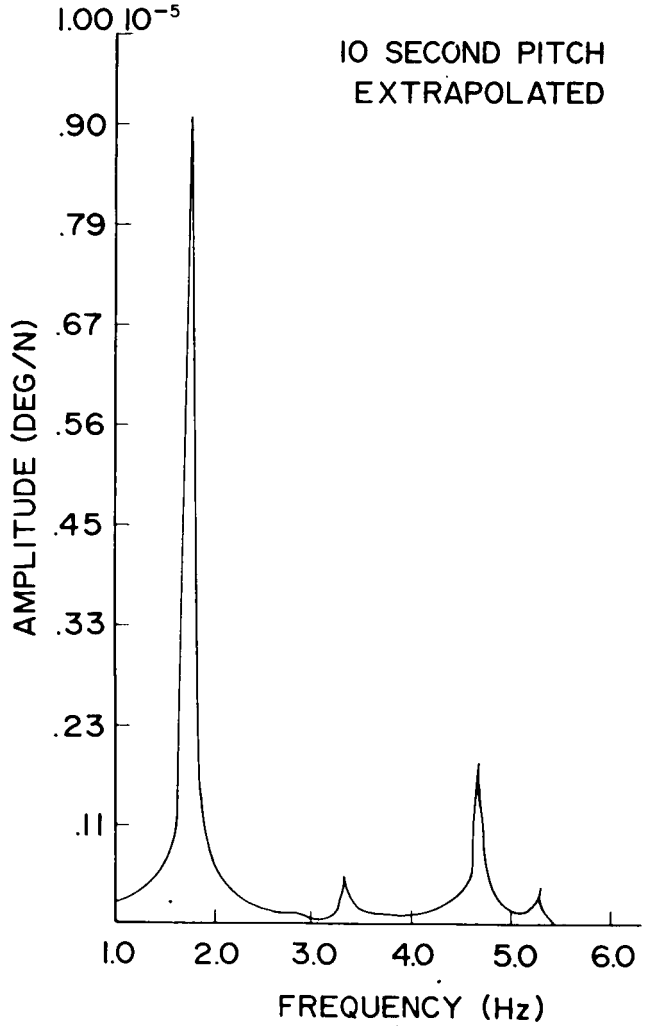

FIGURE 8. EXTRAPOLATED AMPLITUDE FUNCTION, SUSPENSIONLESS

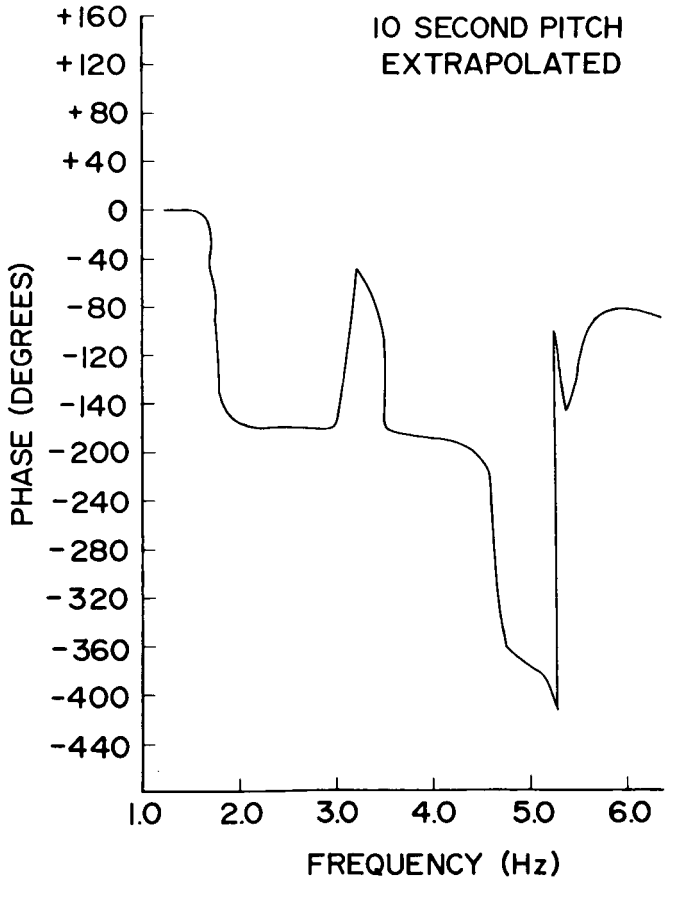

FIGURE 9. EXTRAPOLATED PHASE FUNCTION, SUSPENSIONLESS

REFERENCES

1. Levy, E. C.; Complex Curve Fitting, IRE, Professional Group Transactions on Automatic Control, May 1959.

2. Sanathanan, C. K., and Kaenuer, J.; Transfer Function Synthesis as a Ratio of Two Complex Polynomials, IEEE Transactions on Automatic Control, January 1963.

3. Hay, Frank; "A System for Acquisition and Reduction of Dynamic Test Data of Large Aerospace Vehicles," Astrionics Research and Development Report No. 2, NASA TM X-53044, May 1, 1964, Huntsville, Ala.

G. SIGNAL CONDITIONING CIRCUIT FOR AN OSCILLOSCOPE DISPLAY OF BENDING by Charles P. Elms

The problem of displaying the bending action of a space vehicle or a structural beam is treated by employing a switching circuit that samples the outputs of accelerometers fixed to the frame of a vehicle and displays them on the screen of an oscilloscope. The sampled data are displayed as a vertical column of points representing the sensors. Vertical spacing is proportionate to the spacing of the sensors on the vehicle. The bending motion is represented by horizontal motion of the points proportionate to the bending motion sensed.

A formula for calculating the minimum required sampling rate for an input of chosen maximum frequency is derived, based on the amount of maximum tolerable horizontal display error.

The circuit can be used with any single beam oscilloscope having external intensity modulation capability. It is of simple design and is useful in applications other than bending where more than one variable is to be displayed on one instrument.

The circuit has been built and used to display the bending motions of the Saturn V vehicle simulated by an electronic elastic beam model.

INTRODUCTION

In the simulation of the bending or actual dynamic testing of the vehicle, it is advantageous if one can actually see the movements taking place.

This article describes a technique for the nearly simultaneous display of accelerometer outputs as a function of their vertical location on the vehicle.

By generating a dot corresponding to each location of an accelerometer and having its movement horizontally displayed on the screen proportional to the accelerometer outputs, one can actually see the bending of the vehicle. For this case, ten such dots are generated; nine are accelerometer outputs and one displays the driving force. This is achieved by time sharing the vertical and horizontal inputs of the oscilloscope (Ref. 1). The time sharing is done at such a rate that all the dots seem to appear on the screen at the same time, and time shift between points is negligible compared to the shortest expected period of bending oscillation to be displayed.

NOMENCLATURE

A	amplitude of sine wave input
$B(t)$	blanking signal
d	maximum horizontal deflection error between points $n = 1$ and $n = N_p$ where $t = 0$
$E_n(t)$	n^{th} switching pulse
f_c	clock rate
f_i	frequency of sine wave input
H_n	horizontal deflection at location n for sine wave input
$\overline{H}_n$	H_n when $t = 0$
n	(1, ... 10) index of ring counter stages
N_p	number of points displayed (also number of ring counter stages)
t	time
V_n	vertical dot position bias
Δt	time shift between points n_a and n_{a+1}
$\ddot{\gamma}_n$	acceleration

SYSTEM DESCRIPTION

The system contains a clock generator (Ref. 2), a ten-stage ring counter (Ref. 3) with buffers, 20 gate circuits, and a blanking pulse circuit.

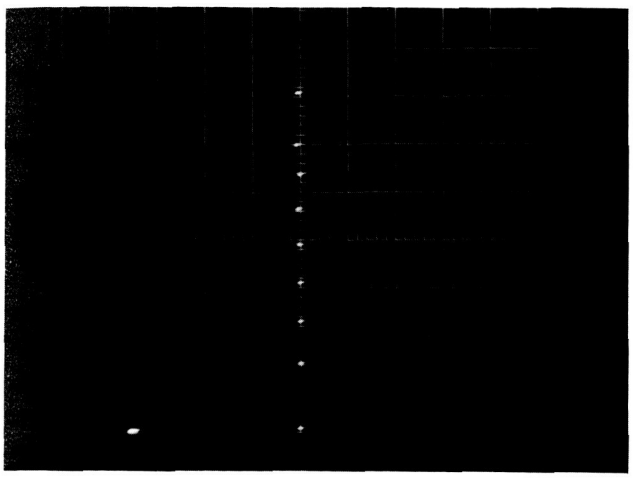

FIGURE 1. VEHICLE AT REST

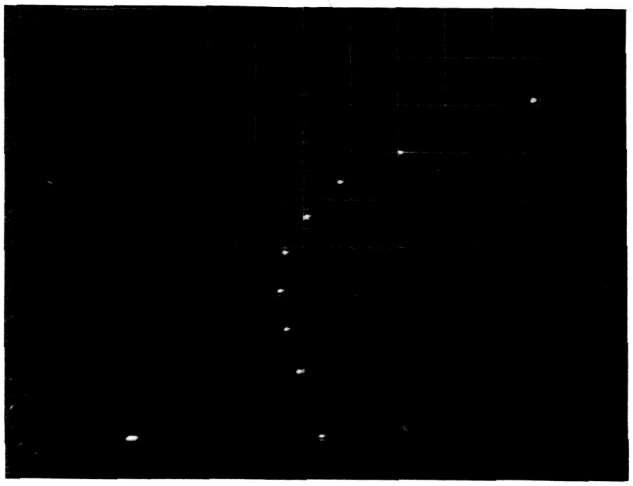

FIGURE 3. SECOND BENDING MODE

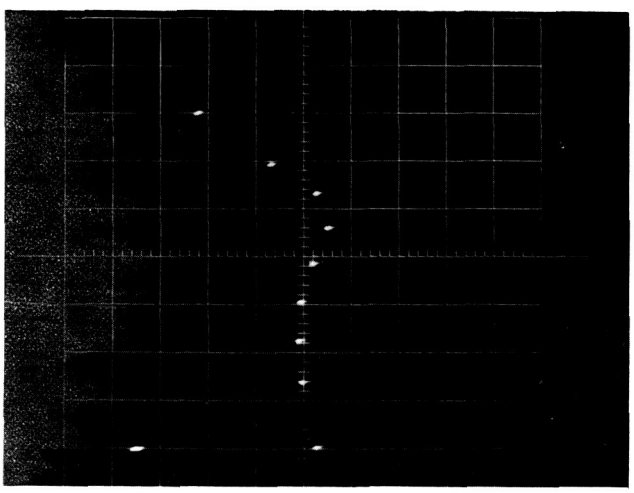

FIGURE 2. FIRST BENDING MODE

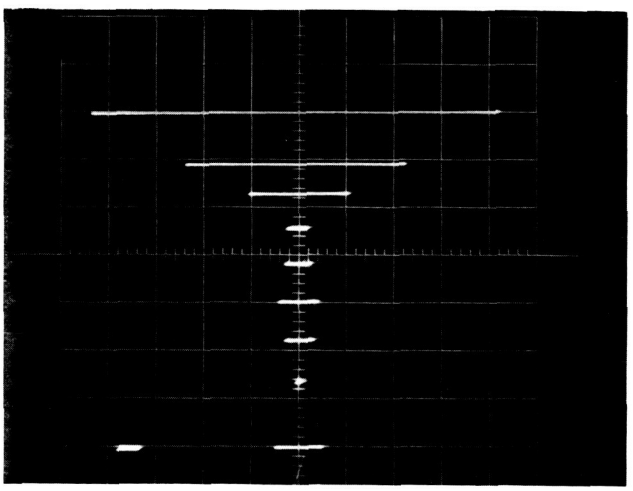

FIGURE 4. ENVELOPE OF FIRST BENDING MODE

Figure 1 depicts the display as seen on the oscilloscope when the vehicle is at rest. Figure 2 shows the vehicle in the first bending mode, and Figure 3 shows the second bending mode. Figure 4 is a time exposure of the first bending mode, thus showing its envelope.

A block diagram of the circuit is presented in Figure 5. The clock is stepping a ten-stage ring counter. Each stage of the ring counter in succession turns on a set of gates. The horizontal gates (the a-gates) accept the acceleration signals and produce time sharing of the horizontal deflection of the oscilloscope. The vertical gates (the b-gates) set up the vertical bias levels corresponding to the location of the accelerometers along the vehicle axis and effect time sharing of the vertical deflection of the oscilloscope. Potentiometers for zero setting, amplitude scaling, and vertical bias level are integral parts of the gate circuits.

The sequential switching from gate to gate must be done fast enough that there is virtually no time delay between samples. When this is done, an undesirable spike occurs. The spike is eliminated by a blanking pulse generated by differentiating the clock generator output which modulates the cathode of a Tektronix RM 561 A Oscilloscope (Ref. 4).

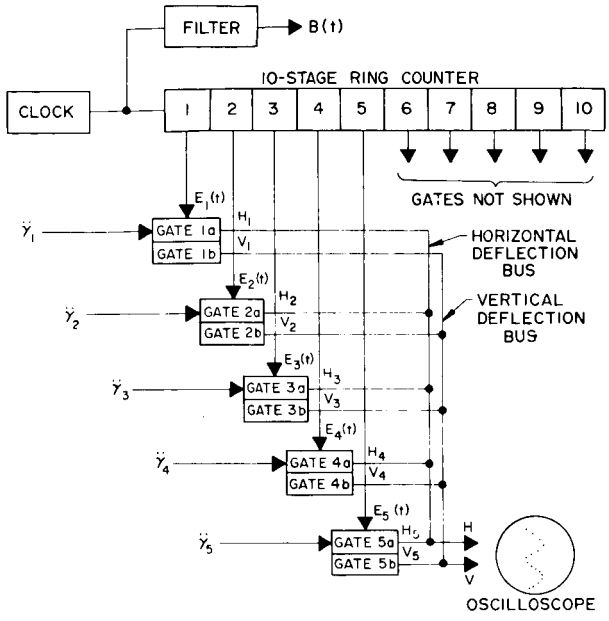

FIGURE 5. SYSTEM BLOCK DIAGRAM

Selection of the sampling rate (clock rate) is based on two considerations. First, the clock rate must be so fast that the eye cannot detect the sampling. Second, the rate must be fast enough to make the error between samples, caused by time shift, negligible. It is shown that the first requirement is fulfilled by the necessarily high rate specified by the second consideration.

Consider the horizontal deflection for sine inputs of frequency $f_{i\,max}$ at locations n as

$$H_n = A_{max} \sin \left[2\pi f_{imax} (t + \Delta t\, n) \right] . \qquad (1)$$

The worst case condition will be when t = 0, the steepest slope of the sine wave.

$$\bar{H}_n = A_{max} \sin \left[2\pi f_{imax} \Delta t\, n \right] , \qquad (2)$$

but

$$\Delta t = 1/f_c . \qquad (3)$$

Then equation 2 becomes

$$\bar{H}_n = A_{max} \sin \left[2\pi \frac{f_i}{f_c} n \right] . \qquad (4)$$

When $2\pi \frac{f_i}{f_c}$ n is small,

$$\bar{H}_n = A_{max}\, 2\pi \frac{f_i}{f_c}\, n . \qquad (5)$$

To find the error caused by time shift between points n_a and n_b ,

$$(\bar{H}_{n_b} - \bar{H}_{n_a}) = A_{max}\, 2\pi \frac{f_i}{f_c} (n_b - n_a) . \qquad (6)$$

If $n_b = N_p$ and $n_a = 1$, then equation 6 yields the horizontal display error d .

$$d = (H_{N_p} - H_1) = A_{max}\, 2\pi \frac{f_i}{f_c} (N_p - 1) \qquad (7)$$

From equation 7, a clock rate f_c may be computed to satisfy a maximum input frequency $f_{i\,max}$ to minimize the maximum horizontal display error resulting from time shift.

For example, let $A_{max} = 4$ cm, $N_p = 10$, $f_{i\,max} = 10$ Hz, and d = .2 cm. Then from equation 7, $f_c = 22{,}608$ Hz.

CONCLUSIONS

The circuit has been installed and is functioning very satisfactorily. Some results of its use can be found in Reference 5.

The main advantages are its compatibility with any standard laboratory oscilloscope having external intensity modulation capability, the simplicity of the circuits involved, and its usefulness in dynamically displaying the bending of a space vehicle.

The discontinuous line (or array of dots) is the main disadvantage. It would be more desirable to have a continuous line to display the bending. Consideration of this is presently being given and development work is being done to implement it.

REFERENCES

1. Elms, Charles P.; Signal Conditioning Circuit for Displaying Pitch, Roll, and Yaw on an Oscilloscope. Astrionics Research and Development Report No. 2, NASA TM X-53044, May 1, 1964.

2. Hurley, Richard B.; Asymmetrical Free-Running Multivibrator, Junction Transistor Electronics, p. 421, John Wiley and Sons, Inc., New York, N.Y. 1960.

3. Marcus, Ira R.; Design Procedure for a Transistor Ring Counter. TR-1154, United States Army Material Command, Harry Diamond Laboratories, Washington 25, D. C., October 15, 1963.

4. Instruction Manual; Tektronic, Inc., P. O. Box 500, Beaverton, Oregon.

5. von Pragenau, George L.; Real Time Analog Computer Simulation of the Elastic Space Vehicle Involving Beam Cell Transmission Matrices. Published in this report.

H. SIMULATION OF FLEXIBLE BODY DYNAMICS BEHAVIOR by Glen D. Ritter

A method for computing flexible body natural frequencies, mode shapes and slopes, and generalized mass during the real time simulation of large launch vehicle flight dynamics is discussed. Derivation of the equations and evaluation of the proposed method through comparison of results with existing theoretical data computed by conventional techniques are described.

Although the method was derived for the real time simulation application, it could be used in the routine computation of elastic body data. The method is useful because it avoids the inherent cumulative errors and the difficulties of high ordered determinant manipulation of more conventional approaches.

INTRODUCTION

In the treatment of large flexible launch vehicle control problems, a recurring question is asked by the control system engineer: Could an analog computer be adapted to the solution of the flexible vehicle dynamics in such a way that it would yield the significant modes quickly enough for a real time simulation? The method discussed here answers this question affirmatively. The approach used extends the result of Mori (Ref. 1) by providing a method, based on well known principles of ordinary differential equations, for quickly determining the proper end conditions. This method could be extended to a "branched" beam structure such as the Saturn I and I-B multiple beam structure. This method could also be used, for example, in the problem discussed by Fettis (Ref. 2) of a two beam structure.

In obtaining equations of lateral vehicle motion, it has been established (Refs. 3 and 4) that structures the size of a space vehicle must be assumed nonuniform, and the effects of shear and rotary inertia must be included. These effects are included in a procedure that should be easily adapted to an analog simulation of the flexible vehicle dynamics. The procedure is evaluated by comparison with data generated from an accepted technique in use at NASA's Marshall Space Flight Center.

Although the method was derived for the real time simulation application, it could be used in the routine computation of elastic body data. The method is useful because it avoids the inherent cumulative errors and difficulties of high ordered determinant manipulation of more conventional approaches.

NOMENCLATURE

A	cross-sectional area	m^2
C_1, C_2	constants	
EI	flexural rigidity	N m^2
M	generalized mass	kg
I	cross-sectional moment of inertia	m^4
kAG	shear rigidity	N
L	length of launch vehicle	m
M	bending moment	N m
Q	shear force	N
t	time	s
U	potential energy	N m
x	measure of length along vehicle axis (station)	m
y	lateral deflection	m
γ	mass per unit volume	kg/m^3
Ψ	slope of deflection curve caused by bending, neglecting shear	rad
ω	angular frequency	rad/s
β	slope of deflection curve caused by shear	rad

DESCRIPTION OF FLEXIBLE VEHICLE EQUATIONS

To obtain the equations of motion of a flexible space vehicle, consider a finite element of the vehicle (Fig. 1). The following assumptions are made:

1. The vehicle has an axis of symmetry.
2. The vehicle is not deflecting beyond its elastic limit.
3. All vibrations are in the plane under consideration.
4. At natural modes, the motion is simple and harmonic.

It is assumed that a space launch vehicle can be considered as an infinite set of uniform elements. The equations of motion become partial differential equations by a limit process and are then valid for a non-uniform vehicle.

The equations of lateral motion for a uniform beam section as shown in Figure 1 can now be derived, assuming variable moments and shear forces acting on both ends of this section. These equations in partial differential equation form are given (Ref. 5).

$$\frac{\partial \Psi(x,t)}{\partial x} = -\frac{M(x,t)}{EI(x)} \tag{1}$$

$$\frac{\partial Y(x,t)}{\partial x} = \frac{Q(x,t)}{kAG(x)} + \Psi(x,t) \tag{2}$$

$$\frac{\partial Q(x,t)}{\partial x} = \gamma A(x)\,\frac{\partial^2 Y(x,t)\,dx}{\partial t^2} \tag{3}$$

$$-\frac{\partial M(x,t)}{\partial x}\,dx + Q(x)\,dx = I\gamma(x)\frac{\partial^2 \Psi(x,t)}{\partial t^2}dx. \tag{4}$$

The displacement Y, the slope neglecting shear effects Ψ, moment M, and shear Q must be a function of time and distance along the vehicle axis to satisfy the set of partial differential equations, 1, 2, 3, and 4. In general, any vibration of a system can be resolved into the natural modes of vibration. When a system is vibrating at one of its natural modes, the system experiences simple harmonic motion; therefore, particular solutions of the equations can be found (Ref. 5). Assuming that the vehicle under consideration is vibrating at a natural mode, solutions of the partial differential equations are given as

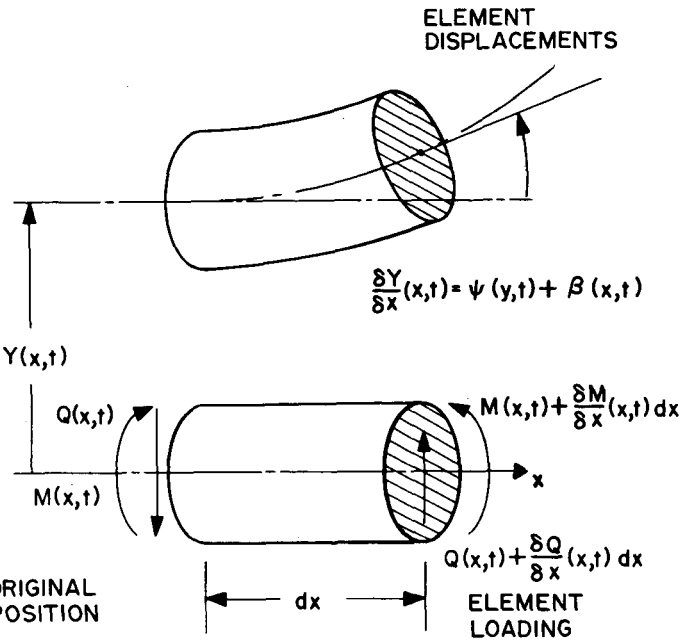

FIGURE 1. ELEMENTS OF A FLEXIBLE VEHICLE

$$Y(x,t) = Y(x)\ \sin\ (\omega t + \varphi) \tag{5}$$
$$\Psi(x,t) = \Psi(x)\ \sin\ (\omega t + \varphi) \tag{6}$$
$$M(x,t) = M(x)\ \sin\ (\omega t + \varphi) \tag{7}$$
$$Q(x,t) = Q(x)\ \sin\ (\omega t + \varphi). \tag{8}$$

Differentiating equations 5 and 6 twice with respect to time,

$$\frac{d^2 Y(x,t)}{dt^2} = -Y(x)\,\omega^2\ \sin\ (\omega t + \varphi) \tag{9}$$

and

$$\frac{d^2 \Psi(x,t)}{dt^2} = -\Psi(x)\,\omega^2\ \sin\ (\omega t + \varphi). \tag{10}$$

Substituting equations 5 through 10 into equations 1 through 4 and factoring out the sin $(\omega t + \varphi)$ terms, the ordinary differential equations are obtained.

$$\frac{d\Psi(x)}{dx} = -\frac{M(x)}{EI(x)} \tag{11}$$

$$\frac{dy(x)}{dx} = \frac{Q(x)}{kAG(x)} + \Psi(x) \tag{12}$$

$$\frac{dQ(x)}{dx} = -\gamma A(x)\ \omega^2 Y(x) \tag{13}$$

$$\frac{dM(x)}{dx} = Q(x) + I\gamma(x)\ \omega^2 \Psi(x). \tag{14}$$

These equations will now yield a solution for any angular frequency ω. However, only the solutions that satisfy certain boundary conditions are of interest.

The ω values for which the particular boundary conditions are satisfied are the natural frequencies of the flexible vehicle described by equations 11 through 14. At these frequencies the natural mode shapes can be obtained from the solution of these equations. This process will now be discussed for a free-free flight vehicle.

For the free-free condition, the moment and shear at both ends are zero. A frequency ω will now be determined that will satisfy the boundary conditions. For a given ω, two solutions will be determined with the following initial conditions:

	Y(0)	Ψ(0)	M(0)	Q(0)
Solution denoted by subscript 1	1	0	0	0
Solution denoted by subscript 2	0	1	0	0

The two sets of solutions are independent solutions of the given differential equations, and the general solution can be written:

$$Y(x) = C_1 Y_1(x,\omega) + C_2 Y_2(x,\omega) \quad (15)$$
$$\Psi(x) = C_1 \Psi_1(x,\omega) + C_2 \Psi_2(x,\omega) \quad (16)$$
$$M(x) = C_1 M_1(x,\omega) + C_2 M_2(x,\omega) \quad (17)$$
$$Q(x) = C_1 Q_1(x,\omega) + C_2 Q_2(x,\omega). \quad (18)$$

This solution has enforced the free-free boundary condition at the end x = 0, by the selection of the initial conditions. The boundary conditions at this end are

$$M(0,t) = M(0) \sin(\omega t + \varphi) = 0.$$
$$Q(0,t) = Q(0) \sin(\omega t + \varphi) = 0.$$

To satisfy the remaining boundary conditions at to other end of the vehicle (x = L), the following equations, from equations 17 and 18, must be satisfied.

$$C_1 M_1(L,\omega) + C_2 M_2(L,\omega) = 0 \quad (19)$$
$$C_1 Q_1(L,\omega) + C_2 Q_2(L,\omega) = 0. \quad (20)$$

The solution to these equations now yields the normal mode frequencies, and this is treated by the usual method of linear equations. The equations have a solution if and only if

$$F(\omega) = \begin{vmatrix} M_1(L,\omega) & M_2(L,\omega) \\ Q_1(L,\omega) & Q_2(L,\omega) \end{vmatrix} = 0, \quad (21)$$

or, expanding the determinant, if

$$F(\omega) = M_1(L,\omega)\, Q_2(L,\omega) - Q_1(L,\omega)\, M_2(L,\omega) = 0. \quad (22)$$

This defines a continuous function of ω. To obtain the normal mode frequencies, it is necessary to determine the zeros of this equation. Several methods could be used: a three point extrapolation method or, as used in this article, Newton's method with the derivative $F'(\omega)$ approximated by the first difference quotient. Equation 22 possesses all of the infinite frequencies associated with this nonuniform beam problem. After a particular frequency ω_1 is determined that satisfies equation 22, it is still necessary to determine the mode shapes. At $\omega = \omega_1$, equation 19 yields

$$\frac{C_2}{C_1} = -\frac{M_1(L,\omega_1)}{M_2(L,\omega_1)} \quad (23)$$

and by choosing

$$C_1 = 1,$$

the mode shapes, slopes, moment, and shear are easily determined from equations 15 through 18 at the frequency $\omega = \omega_1$.

GENERALIZED MASS

While the natural frequencies and mode shapes are important to control system design, the generalized mass, another variable (Ref. 3) needed in control analyses, can be found from the modal solution of the equations of motion.

The differential expression for potential energy of a finite section of the vehicle is

$$dU(x) = \frac{1}{2} M(x) \cdot \frac{\partial \Psi(x)}{\partial x}\, dx + \frac{1}{2} Q(x)\, \beta(x)\, dx.$$

Integrating this equation yields

$$U = \frac{1}{2} \int_0^L M(x) \cdot \frac{\partial \Psi(x)}{\partial x}\, dx + \frac{1}{2} \int_0^L Q(x) \cdot \beta(x)\, dx.$$

Substituting $\frac{\partial \Psi}{dx}$ from equation 11, and since

$\beta(x) = \frac{Q(x)}{kAG(x)}$ (from Fig. 1 and equation 2),

the potential energy equation becomes

$$U = \frac{1}{2} \left[\int_0^L \left(\frac{M^2(x)}{EI(x)} + \frac{Q^2(x)}{kAG(x)} \right) dx \right].$$

The maximum kinetic energy of a conservative system at a particular normal mode frequency ω is defined by

$$T = \frac{1}{2} \overline{M} \omega^2$$

where $\overline{M}$ is the generalized mass of the normal mode frequency ω.

Under the assumption that at a normal mode the maximum potential energy of a system is equal to the maximum kinetic energy,

$$\frac{1}{2}\overline{M}\omega^2 = \frac{1}{2} \left[\int_0^L \left(\frac{M^2(x)}{EI(x)} + \frac{Q^2(x)}{kAG(x)} \right) dx \right]$$

The generalized mass $\overline{M}$ is therefore

$$\overline{M} = \frac{1}{\omega^2} \int_0^L \left(\frac{M^2(x)}{EI(x)} + \frac{Q^2(x)}{kAG(x)} \right) dx. \qquad (24)$$

M(x) and Q(x) are obtained from the preceding sections. Equation 24 can then be solved to yield the generalized mass at any particular natural mode.

CONCLUSIONS

The results of this method compare closely with those of other theoretical methods. The solution of equations by this method, considering the S-IV stage with a Jupiter nose cone, yields a first mode frequency

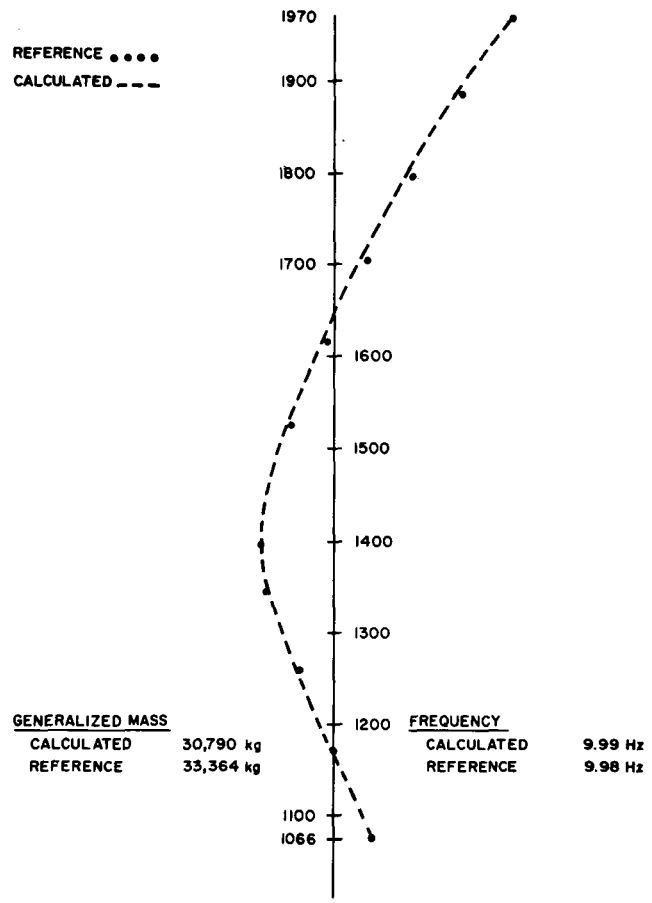

FIGURE 2. S-IV WITH JUPITER NOSE, FIRST MODE

of 9.99 Hz, compared to 9.98 Hz obtained from bending data.* The mode shape obtained was also close to the mode shape obtained from the bending data (Fig. 2). The second mode frequency was calculated to be 21.56 Hz, compared to 24.2 Hz from the reference data. The second mode shape is also close, as can be seen from Figure 3. The first mode generalized mass for the S-IV stage with a Jupiter nose cone payload calculated by this method is 30,790 kg, compared to 33,364 kg of the reference data.

It is concluded that the method described will be an effective normal mode analysis technique for nonuniform space launch vehicles because of its accuracy and the ease of application to relatively complicated problems. One advantage of this method is that the higher modes are not dependent on the solution of the lower modes; therefore error is not accumulated from

* Unpublished Aeroballistic theoretical SA-5 bending data.

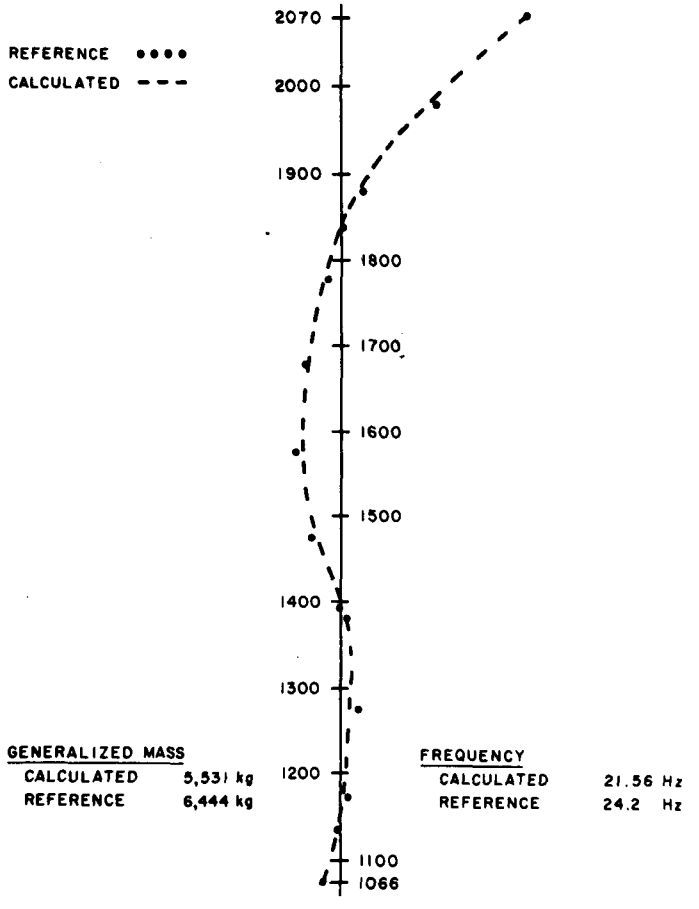

FIGURE 3. S–IV WITH JUPITER NOSE, SECOND MODE

mode to mode as is the case with matrix methods. A disadvantage in using this procedure on a digital computer is the computation time necessary to numerically integrate the system of differential equations.

While the method is completely amenable to digital computation, use of an analog computer to integrate the system of ordinary differential equations 11 through 14 should result in a substantial saving in overall computation time. Use of analog computation, with machine time t representing the variable x, would also permit properties of the vehicle to be stored on either function generators or a cam device, thereby permitting a complete characterization of continuous vehicle properties. An analog block diagram for solution of the system of ordinary differential equations 11 through 14 is shown in Figure 4. Figure 5 is a flow diagram summarizing the overall technique.

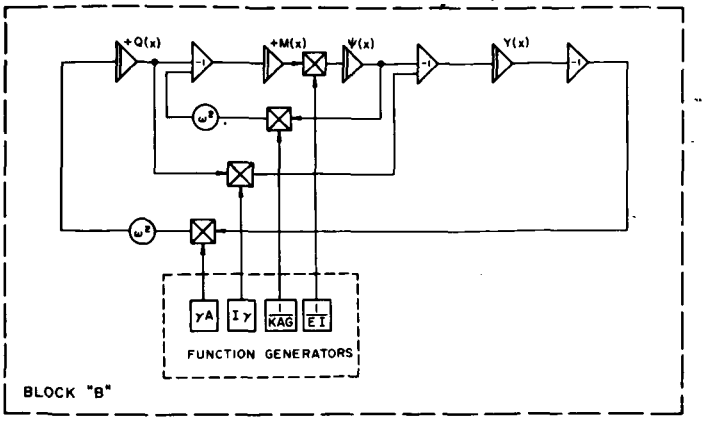

FIGURE 4. ANALOG SCHEMATIC DIAGRAM

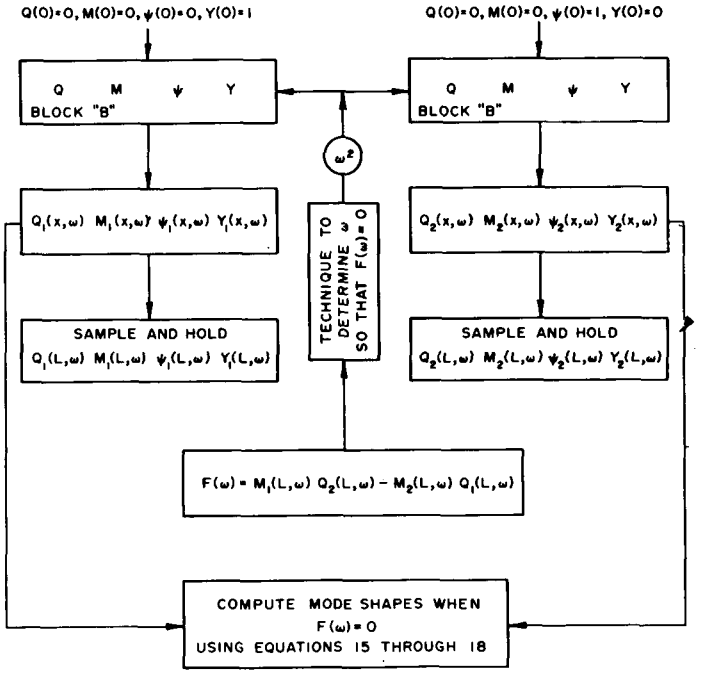

FIGURE 5. SOLUTION FLOW CHART

One possible area of further investigation is the manner in which the zeros of $F(\omega)$ are obtained. Newton's method, replacing the derivative $F'(\omega)$ by the difference quotient, gave entirely satisfactory results in the cases considered. However, it is quite possible that other procedures would be easier to implement and faster on an analog computer simulation. This possibility is also currently under investigation and will be discussed in a future article.

REFERENCES

1. Mori, Daikichiro; "Application of the Analog Computer to Flexural Vibration of Beams." Proceedings of the 7th Japan National Congress for Applied Mechanics, 1957.

2. Fettis, Henry E.; "Vibration Modes of a Two-Beam System by the Holzer Method." Journal of the Aerospace Sciences, November 1962.

3. Rheinfurth, Mario H.; Control-Feedback Stability Analysis, ABMA DA-TR-2-60, Redstone Arsenal, Alabama, January 1960.

4. Traill-Nash, R. W., and Collar, A. R.; "The Effects of Shear Flexibility and Rotatory Inertia of the Bending Vibrations of Beams," Quarterly Journal of Mechanics and Applied Mathematics, Vol. VI, 1953.

5. Timoshenko, S.; Vibration Problems in Engineering, D. Van Nostrand Company, Inc., New York, N. Y., 1955.

6. Scarborough, J. B.; Numerical Mathematical Analysis, the John Hopkins Press, Baltimore, Md., 1955.

II. INSTRUMENTATION SYSTEMS

A. A PROPELLANT SLOSH MEASURING SYSTEM FOR SPACE VEHICLES by B. G. Bynum and John F. Hamlet

A knowledge of the slosh characteristics of liquid propellants in space vehicles is necessary to determine control, structural, and pressurization parameters. This article describes the theory and configuration of a capacitance system that may be used to measure the first mode of propellant slosh. Two pairs of parallel flat-plate capacitance probes extending the length of the propellant tank are connected into two bridge circuits. Difference in liquid height on diametrically opposed probes causes a difference in capacitance between the two probes. This difference unbalances the bridge circuit and causes a voltage output from the electronics package proportional to the height of slosh. The electronic theory of the system is presented with an explanation of the circuit design and operation. The design of the probes is described, and supporting theory is presented. Circuit diagrams and illustrations of the electronics network, probe construction, and vehicle installation are included. Tests proved that the system measured slosh accurately within 1.5 cm.

Author

INTRODUCTION

A knowledge of the slosh characteristics of liquid propellants in space vehicles is necessary to determine control, structural, and pressurization parameters. This report describes a plan whereby capacitance sensors may be used to measure the first mode of propellant slosh.

Slosh is normally measured by differential pressure transducers or computed from liquid level measurement data. The technique presented here utilizes four liquid level measuring sensors mounted on the inside of a circular tank at 90-degree intervals and extending the length of the tank. Differential liquid level between pairs of opposing sensors is computed and transmitted to earth.

The slosh sensors are flat plate capacitors in which the propellant and ullage gas are the dielectrics. The capacitance of a sensor is a function of propellant height and dielectric constant of the media in which the sensor is submerged. Slosh is measured by measuring the difference in capacitance of opposing probes. Figure 1 shows the location of the slosh sensors in a propellant tank. The advantages of this scheme are (1) simplification of data reduction on the ground, (2) conservation of telemetry bandwidth, and (3) reduced circuitry. Two prototype sensors, each 10.16 meters in length, and a breadboard circuit were built and tested.

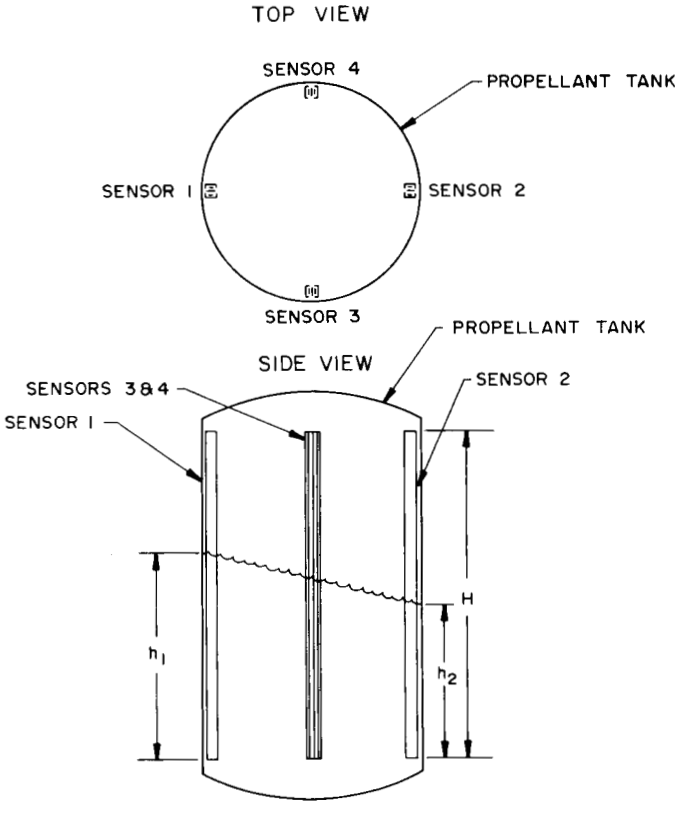

FIGURE 1. TANK INSTALLATION OF RP-1 SLOSH MEASURING PROBE

NOMENCLATURE

C	sensor capacitance
C_s	stray capacitance of sensor
C_a	active capacitance of sensor
h	height of liquid
H	length of sensor
e_L	dielectric constant of liquid
e_G	dielectric constant of gas
ω	angular velocity of excitation vector
E_o	output after amplification
E_i	bridge output voltage
A	amplifier gain
R_1	bridge zero adjust potentiometer
$E_2 E_1$	bridge excitation voltage
k	constant
C_f	full capacitance of a sensor
C_e	empty capacitance of a sensor
a	slope of liquid surface in h-x plane
x z h	tank coordinates
b	slope of liquid surface in h-z plane

ELECTRICAL CHARACTERISTICS

The capacitance of a sensor is given by equation 1; the sensor is assumed to be linear to the required accuracy over its entire length.

$$C = C_S + C_a \left(e_L \frac{h}{H} + e_G \frac{H-h}{H}\right) \quad (1)$$

$$= C_S + C_a \left[e_G + (e_L - e_G) \frac{h}{H}\right].$$

Figure 2 shows a bridge circuit which may be used to translate the capacitance of two sensors into differential liquid height. C_1 and C_2 are the capacitances of two diametrically opposed sensors. C_3, C_4, and C_5 are cable capacitances and sensor capacitances to ground. E_1 and E_2 are bridge voltages for capacitances C_1 and C_2, respectively, of the two sensors. R_1 is a variable resistor used to balance the bridge by adjusting the magnitude of E_1.

If R_1 is chosen small enough that no significant phase difference exists between E_1 and E_2, the following equation defines E_i, the voltage resulting from unbalance of the bridge.

$$E_i = \frac{E_1 j\omega C_1 - E_2 j\omega C_2}{j\omega (C_1 + C_2 + C_3) + \frac{1}{R_2}}.$$

If the conductance $\frac{1}{R_2}$ is much greater than the susceptance $\omega(C_1 + C_2 + C_3)$, the above equation may be simplified to

$$E_i = R_2 (E_1 j\omega C_1 - E_2 j\omega C_2).$$

E_0, the output of the circuit representing a difference in capacitance between the two probes, is obtained by amplification of E_i. The gain of the amplifier is represented by A.

$$E_0 = AE_i = AR_2 (E_1 j\omega C_1 - E_2 j\omega C_2)$$

$$= K (E_1 C_1 - E_2 C_2) \quad (2)$$

where $K = Aj\omega R_2$.

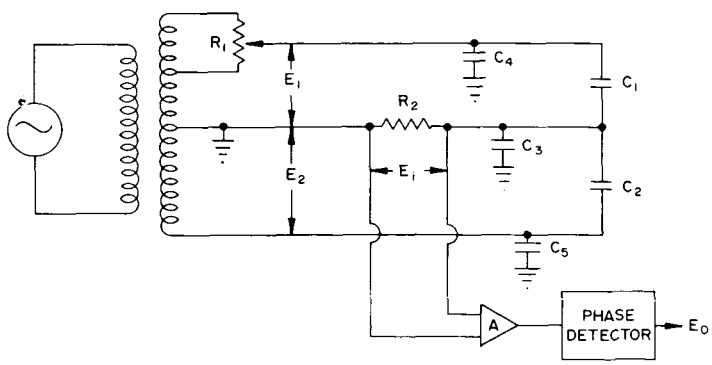

FIGURE 2. SCHEMATIC OF SLOSH SENSOR ELECTRONICS

Substituting equation 1, which represents the capacitance of a probe, for C_1 and C_2 in equation 2 gives the following.

$$E_0 = K \left[E_1 \left\{ C_{s_1} + C_{a_1} \left[e_G + (e_L - e_G) \frac{h_1}{H} \right] \right\} - E_2 \left\{ C_{s_2} + C_{a_2} \left[e_G + (e_L - e_G) \frac{h_2}{H} \right] \right\} \right]$$

$$= K \left[E_1 C_{a_1} \frac{h_1}{H} (e_L - e_G) - E_2 C_{a_2} \frac{h_2}{H} (e_L - e_G) + E_1 (C_{s_1} + C_{a_1} e_G) - E_2 (C_{s_2} + C_{a_2} e_G) \right]. \quad (3)$$

For $h_1 = h_2 = 0$,

$$E_0 = K \left[E_1 (C_{s_1} + C_{a_1} e_G) - E_2 (C_{s_2} + C_{a_2} e_G) \right].$$

If E_1 is adjusted by R_1 so that $E_0 = 0$ when $h_1 = h_2 = 0$,

$$E_1 (C_{s_1} + C_{a_1} e_G) = E_2 (C_{s_2} + C_{a_2} e_G) \quad (4)$$

and equation 3 becomes

$$E_0 = \frac{K}{H} (E_1 C_{a_1} h_1 - E_2 C_{a_2} h_2) (e_L - e_G). \quad (5)$$

The stray capacitance of a sensor is proportional to the sensor active capacitance; the proportionality constant is identical for all sensors of identical construction. This relationship is expressed by the following equations.

$$C_{s_1} = BC_{a_1} \quad (6)$$

$$C_{s_2} = BC_{a_2}. \quad (7)$$

Substituting equations 6 and 7 into equation 4 gives the following.

$$\frac{E_1}{E_2} = \frac{BC_{a_2} + C_{a_2} e_G}{BC_{a_1} + C_{a_1} e_G} = \frac{C_{a_2}}{C_{a_1}}$$

$$E_1 C_{a_1} = E_2 C_{a_2}. \quad (8)$$

Substituting equation 8 into equation 5 gives a final expression of circuit output. The output E_0 may be filtered and biased to obtain the proper telemetry voltage range.

$$E_0 = \frac{K}{H} C_{a_1} E_1 (h_1 - h_2) (e_L - e_G). \quad (9)$$

It can be seen from equation 9 that E_0 will be proportional to $h_1 - h_2$ if $C_{a_1} (e_L - e_G)$ is known.

The effect of the variables e_L and e_G may be eliminated by subtracting the empty capacitance C_e ($C_e = C_s + C_a e_G$) from the full capacitance C_f ($C_f = C_s + C_a e_L$). Thus

$$C_f - C_e = C_a (e_L - e_G),$$

which is the unknown in equation 9. The only variable in equation 9 is, therefore, $(h_1 - h_2)$.

The full capacitance of a sensor may be measured by using the signal conditioning circuit. If a known fixed capacitor is switched into the circuit in place of one of the sensors, the output then indicates the difference between the capacitance of the remaining sensor and that of the known capacitor. The empty capacitance of the sensors is known from previous measurements of the sensor in air. The difference between the dielectric constants of air and ullage gas is not significant for non-cryogenic propellants. For cryogenic propellants, a correction factor should be added to account for this difference.

The slosh measuring system described in this article is a point measuring device; therefore, it can only be used when the shape of the liquid surface is known. The orientation of a planar liquid surface, as when slosh frequency is low relative to the first resonant frequency, is determined as follows (Fig. 3).

$$h - h_0 = ax + bz; \quad (10)$$

h_0 is the average propellant height, a is the slope of the liquid surface in the z plane, and b is the slope of the liquid surface in the x plane. The deviation of any point on the surface from the average propellant height, $h - h_0$, is to be determined.

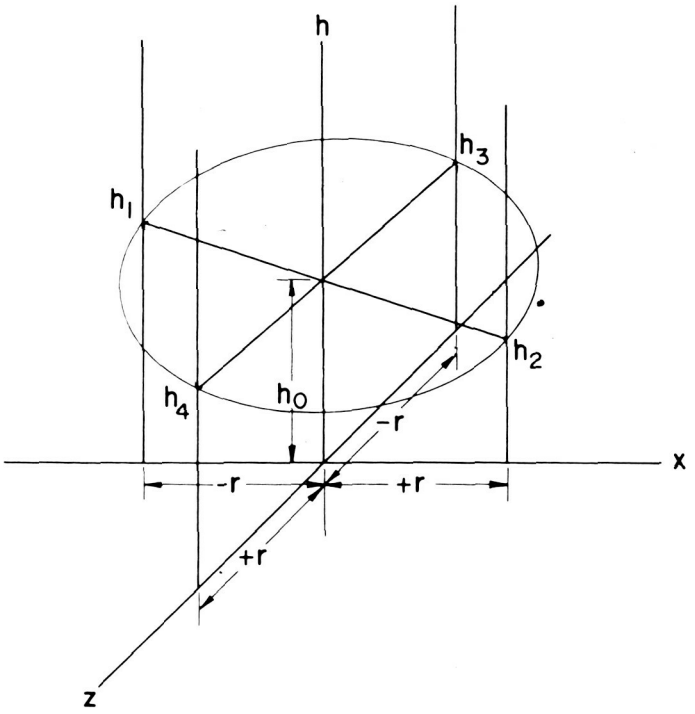

FIGURE 3. THREE-DIMENSIONAL REPRESENTATION OF PLANAR LIQUID SURFACE

The axes x and z in Figure 3 are drawn along the bases of the two planes of liquid slosh measurement. Liquid height data are thus provided by sensors at known distances r along x and z from the origin (center line of the tank); the output of one pair of sensors in one plane is $h_1 - h_2$; the output of the other pair in the other plane is $h_3 - h_4$. With these data, a and b may be determined by the following equations.

For the two sensors located at z = 0, x = +r and -r,

$$a = \frac{h_1 - h_2}{2r}.$$

For the two sensors located at x = 0, z = +r and -r,

$$b = \frac{h_3 - h_4}{2r}.$$

If the motion of the liquid surface is a form of periodic motion such as simple harmonic motion, the outputs of the two pairs of probes readily provide information on slosh frequency, peak amplitude, and orientation.

SENSOR CHARACTERISTICS

The conventional capacitance sensor consists of rigid concentric tubes, open top and bottom, supported and insulated from each other by solid insulators. This is not the optimum design if fast response is required as in slosh measurements.

A parallel plate configuration was selected for the slosh sensor for a practical design to obtain fast response, minimum weight and size, and ease of assembly.

A cross-section of the sensor is shown in Figure 4, and a section of the sensor is shown in Figure 5. The two outer plates are connected as one electrode, and the center plate forms the other electrode. The shields confine the field mainly to the area between the capacitance plates and form a rigid structure for support of the probe. The parameters of the parallel plate construction cannot be accurately defined analytically as can a concentric tube construction; but from the general equation for a parallel plate capacitor, the major problem can be seen to be in maintaining the plate area and spacing constant as a function of sensor length. The unique design of the sensor minimizes all extreme tolerance requirements without sacrificing performance. The use of a center

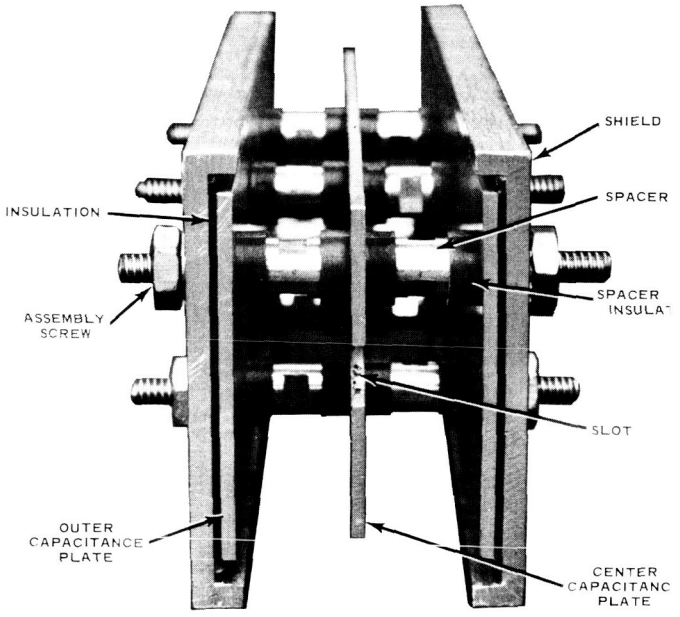

FIGURE 4. CROSS SECTION OF PROBE

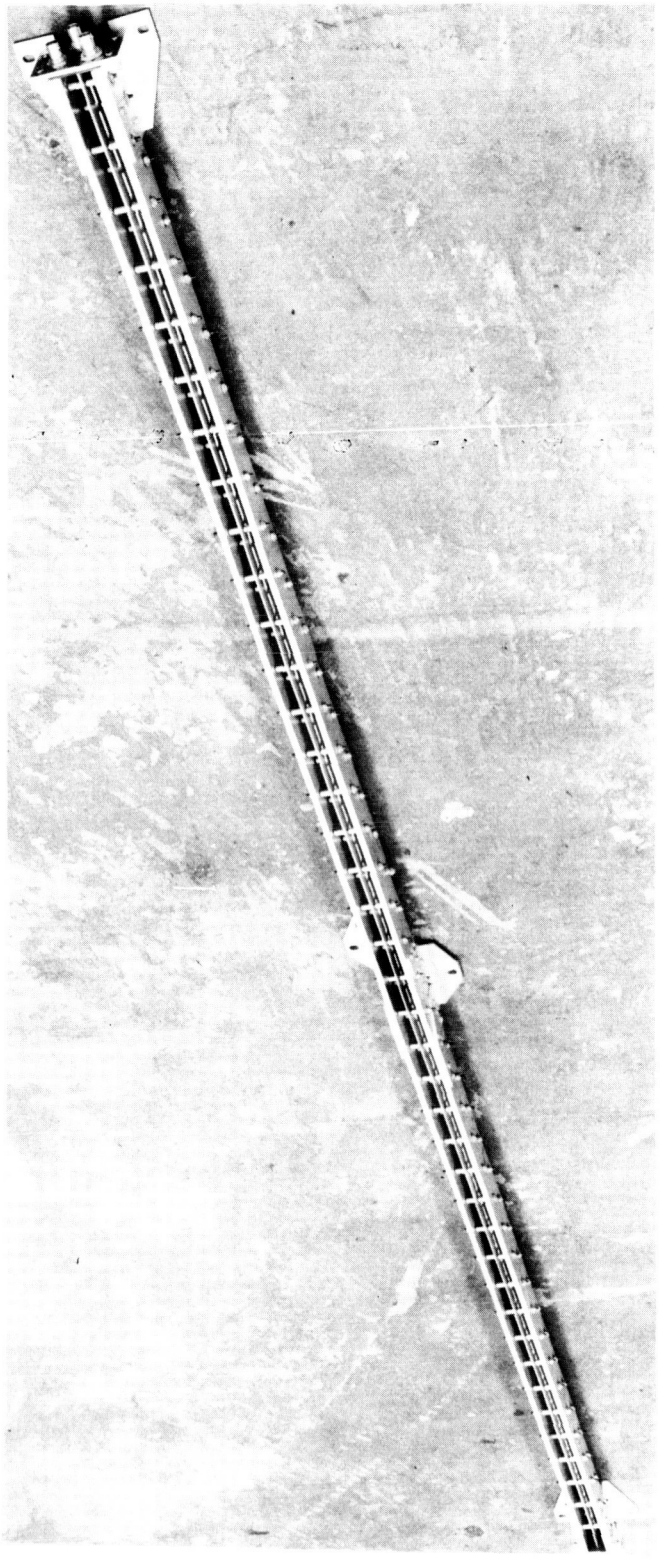

FIGURE 5. OVERALL VIEW OF PROBE

plate doubles the capacitance but requires very little additional weight. The spacing between the outside plates is large (approximately 2.5 cm) and is controlled by molded spacers. The center plate is narrower than the outer plates; this feature minimizes the effect of lateral movement of the center plate in relation to the outer plates. The center plate is slotted to eliminate the effects of spacers on linearity. Relatively large displacements of the center plate toward the outside plates, which could occur under vibration environments, can be tolerated with very small effects on capacitance. This can be seen from the curve of capacitance versus displacement of center plate (Fig. 6). A 5 percent displacement causes only a 0.25 percent change in capacitance. The active capacitance of the probe is approximately 0.4pF/cm. The capacitances to ground of the probe are relatively large, but their effects are eliminated by connecting the sensor as a three-terminal capacitor with the large shunt capacitors placed across very small impedances.

Spacers are located at intervals of 2.5 cm along the probe to maintain adequate spacing and structural integrity. These spacers form conductive paths between the two elements of the capacitor that drastically

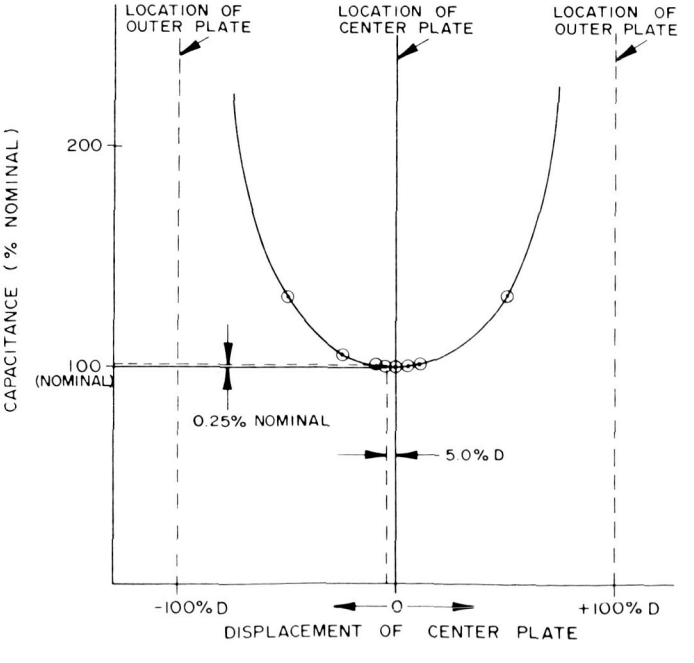

FIGURE 6. SENSOR CAPACITANCE VS DISPLACEMENT OF CENTER PLATE

lower the Q of the sensor. This problem is eliminated by making conductive guards in the center of the spacers. The guards are grounded to the shields by the bolts in the spacers. This technique eliminates the effect of conductive currents by shunting them to the bridge guard point in parallel with very low impedances.

The sensor is designed in segments for easy installation. The segment interconnections are designed so no discontinuities are at segment joints.

Two 10.2 m sensors and a breadboard circuit were built and tested. The tests show that an accuracy of approximately ± 1.5 cm is achieved.

The technique is to be used on the S-IC vehicle to measure fuel slosh.

B. AN EMERGENCY HELIUM BUBBLING CONTROL SYSTEM FOR THE PREVENTION OF GEYSERING IN THE LOX SUCTION LINES OF S-IC

by James A. Power and A. Turel*

ABST:

An emergency helium bubbling system was devised for geyser suppression in the LOX suction lines of S-IC. Flight model pressure and temperature transducers were compared to more accurate transducers to determine the best sensor configuration. Transducers were electronically simulated to calibrate the circuit design. A development system was tested for feasibility on a full-scale LOX flow line test facility.

AUTHOR:

INTRODUCTION

Large space vehicles with long LOX suction lines to the engines have a common danger problem in that vaporization in the bottom of the lines may produce a geyser during the oxidizer loading and prelaunch period. A geyser occurs when the heat input to the bottom of the line causes vapor to form in excess of the normal bubble release. The increased rate of vaporization causes expulsion of the liquid and sudden gravitational refilling of the line from the tank above, resulting in a pressure surge large enough to damage feed lines, valves, and line supports.

A cross-feed circulation technique, thermal self-pumping, is used to prevent geysering in the LOX suction lines of S-IC. The circulation is initiated by bubbling helium into one line only. The colder LOX flows down one line and through interconnect lines to a line with warmer LOX, displacing the warmer LOX upward to be cooled by the large volume of colder LOX in the tank.

If in emergency cases thermal self-pumping is inadequate to prevent geysering conditions, a method is needed to suppress geysering. One technique would be to continuously bubble helium into the lines. Enough helium would have to be injected to cope with the worst possible conditions, which for the entire prelaunch period would require a considerable amount of helium. Helium is in short supply and is considered a critical material.

If a suitable control system could be devised, the helium would only be used in the case of an emergency. Astrionics Laboratory was requested to investigate the feasibility of using a system of flight instrumentation transducers and electronic circuitry to provide the necessary helium bubbling control.

The following goals were established for the system:

a. LOX suction line ambient pressure should be monitored between 22.8 and 51.7 N/cm^2, with maximum accuracy in the range of 34.5 to 51.7 N/cm^2.

b. LOX suction line internal temperature should be monitored between -184.4° and -156.7° C.

c. Helium bubbling should be initiated if the internal temperature of the suction line rises to within 0.56° C of the LOX vaporization temperature. (Since the initiation of this program, tests have indicated that the actual differential temperature used will be greater than 2.78° C.)

The mechanical layout of the system is shown in Figure 1.

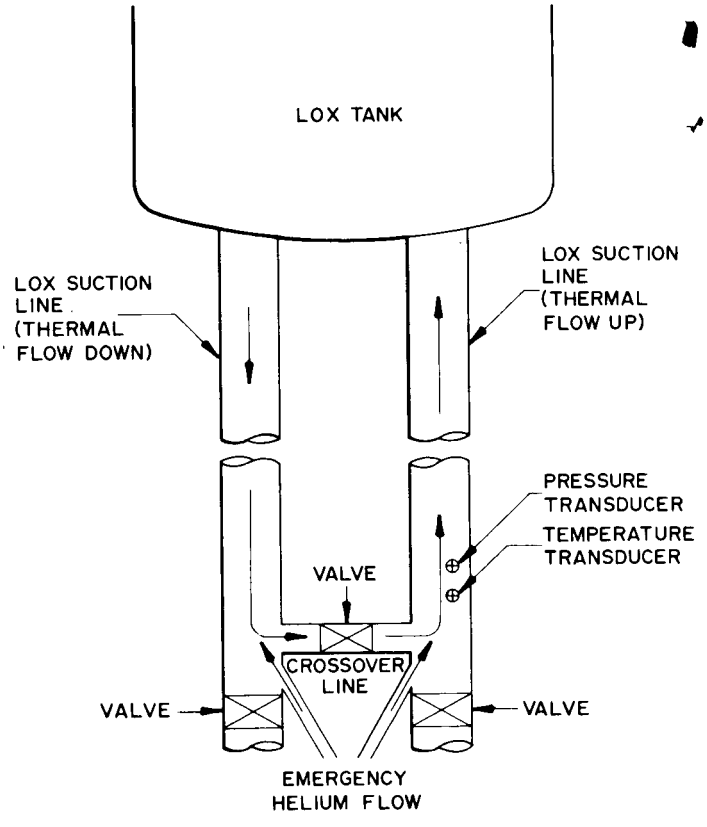

FIGURE 1. MECHANICAL LAYOUT OF HELIUM BUBBLING CONTROL SYSTEM

* Brown Engineering Company

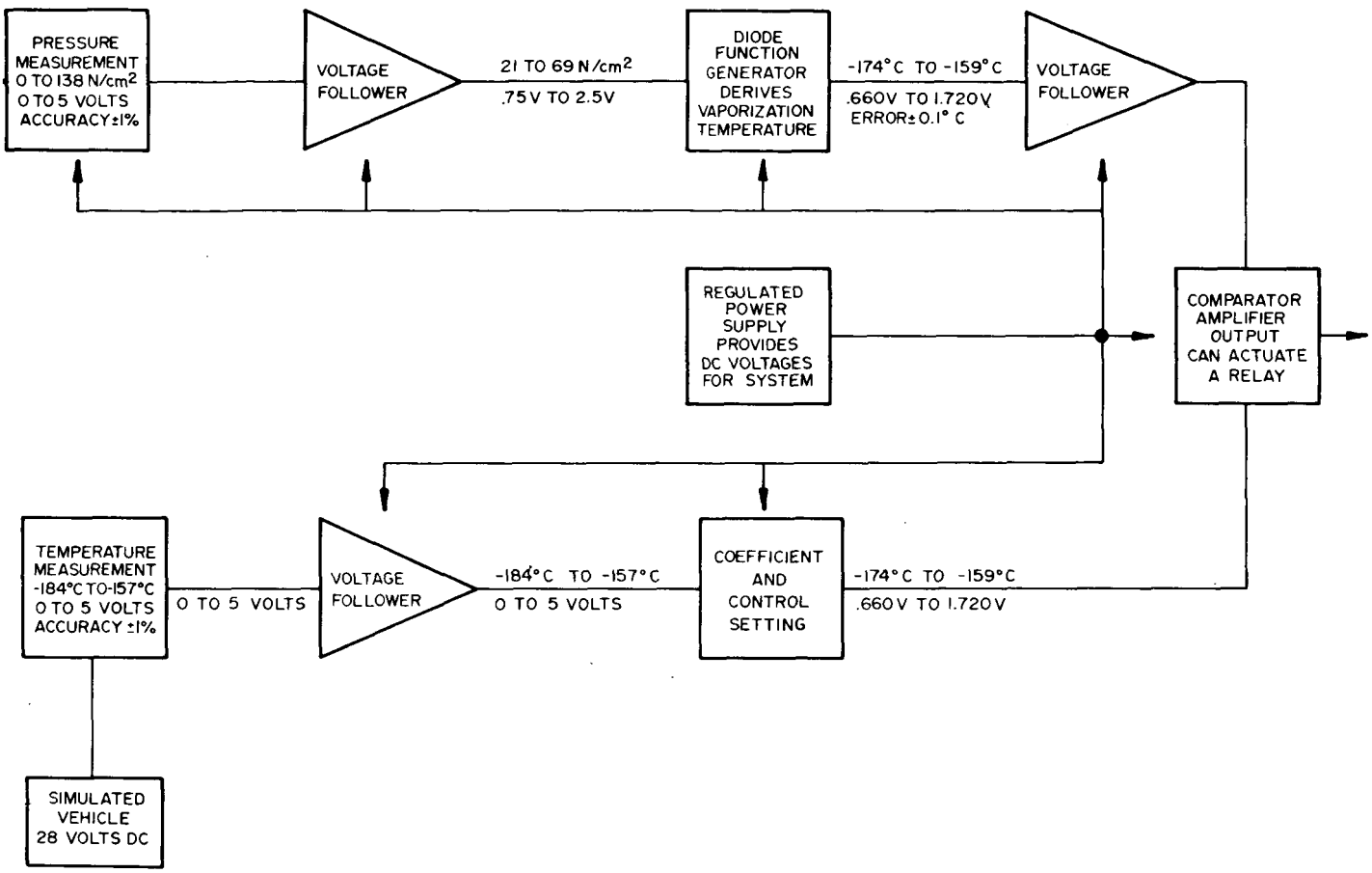

FIGURE 2. BLOCK DIAGRAM OF HELIUM BUBBLING CONTROL SYSTEM

The following method is proposed for sensing the danger of geysering (Fig. 2):

a. Pressure in the LOX suction line would be measured.

b. The LOX vaporization temperature would be derived from the output of the pressure transducer.

c. The temperature of LOX in the suction line would be measured.

d. The internal temperature and the vaporization temperature would be compared. If the difference between the two is small, indicating that vaporization is likely, an alarm signal would be initiated.

SYSTEM DESIGN DETAILS

A study was conducted to determine whether measurements of pressure and temperature inside the LOX suction lines could be obtained with sufficient accuracy, using flight transducers, for use in the helium bubbling control system. A circuit was designed for testing with flight transducers; then performance characteristics of the circuit and flight transducers were determined prior to operational testing.

Pressure Transducer Evaluation. The pressure transducer specified for flight measurements is a bellows/potentiometer sensor with a range of 137.9 N/cm^2 (Fig. 3). The performance characteristics of this model transducer in several ranges are given for comparison in Table 1. Vibration and acceleration will contribute no significant errors during the prelaunch period when helium bubbling control is needed.

A 2.76 N/cm^2 error in the 137.9 N/cm^2 transducer is equivalent to 1.11° C in the derived vaporization temperature. A diode function generator (DFG) is to be used with the pressure transducer to derive the vaporization temperature of LOX at a given pressure.

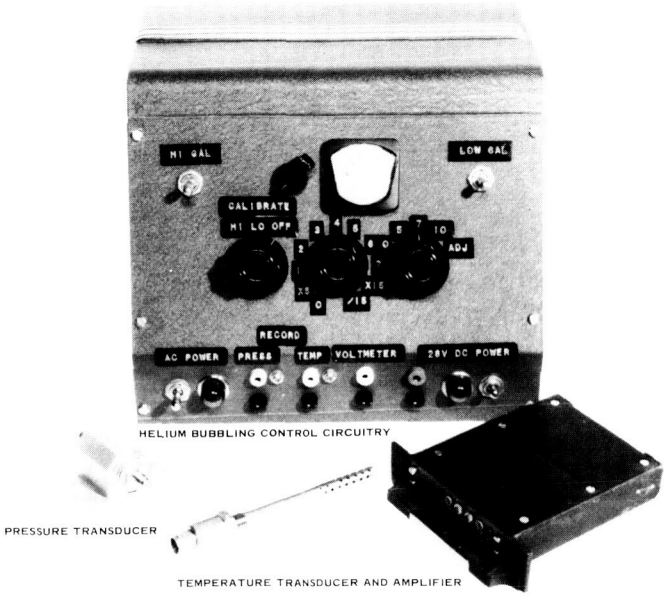

FIGURE 3. COMPONENTS USED IN FEASIBILITY TEST SYSTEM

TABLE 1. PERFORMANCE CHARACTERISTICS OF THE PRESSURE TRANSDUCER DURING SATURN V PRELAUNCH PERIOD

Pressure Range (N/cm^2)	Static Error Band (%)	Static Error Band Plus Temperature Error Band (%)	Error to be Expected (N/cm^2)
1.71	± 1.2	± 2.2	± 1.14
68.95	± 1.0	± 2.0	± 1.38
137.9	± 1.0	± 2.0	± 2.76

This DFG will contribute an error of ± 0.11°C over any 50°C temperature range. Total error of the derived LOX vaporization temperature measurement is, therefore, ±1.22°C. Use of a lower pressure range transducer (Table 2) or use of a strain gauge transducer would improve accuracy.

Temperature Transducer Evaluation. The temperature transducer used for flight measurements is a platinum resistance sensor (Fig. 3). The value of resistance of the unit is specified to be 1400 ohms ±0.5 percent at 0°C; at any temperature, the repeatability of the unit is specified to be within ±0.5 ohm. A dc amplifier assembly is specified for use with this temperature sensor. Amplifier performance specifications for a period of 8 hours are as follows:

Linearity = ± 1%

Gain Stability = ± 1%

Output Drift = ± 0.5%

RSS Error = ± 1.5%.

Present Astrionics procedures allow for the temperature measurement to be obtained in several ways. One method of making the platinum resistance sensor measurements is to use uncalibrated gauges and an associated dc amplifier and to depend upon the above specifications to limit the error to the following expression:

$$\text{Total RSS Temperature Error} = \sqrt{\begin{pmatrix}\text{error}\\ \text{of } R_0\\ \text{at } 0^\circ C\end{pmatrix}^2 + \begin{pmatrix}\text{error}\\ \text{of read-}\\ \text{ing}\end{pmatrix}^2 + \begin{pmatrix}\text{error}\\ \text{of dc}\\ \text{amp}\end{pmatrix}^2 + \begin{pmatrix}\text{wire}\\ \text{leads}\\ \text{error}\end{pmatrix}^2}$$

$$= \sqrt{(0.5)^2 + (0.12)^2 + (1.5)^2 + (\text{wire leads error})^2}$$

$$\approx 2.0\%.$$

The wire leads connecting the platinum resistance element to the bridge produce an error that is difficult to evaluate. A second method of making the temperature measurement is to use a three-wire bridge that puts a signal lead in each side of the bridge and reduces the error effect of the leads. For this discussion, the non-calibrated method using a three-wire bridge will be assumed to produce an accuracy of 1.6 percent.

An improvement in the accuracy of the measurement should be obtained by calibrating the total measurement, both temperature gauge and dc amplifier, and by using a three-wire bridge. The total error for the calibrated temperature measurements would be as follows:

$$\text{Total Temperature Error} = \sqrt{(0.12)^2 + (1.50)^2}$$

$$= 1.5\%.$$

TABLE 2. PRESSURE ACCURACY ATTAINABLE

Range and Type Of Transducer	Total Error (±%)	Total Error (± N/cm²)	Resulting Error in Vaporization Temperature (± °C)	Total Error with DFG (± °C)
137.9 N/cm² potentiometer type	2.0	2.76	1.1	1.2
69 N/cm² potentiometer type	2.0	1.38	0.6	0.7
69 N/cm² strain gauge	1.0	0.69	0.3	0.4

TABLE 3. TEMPERATURE ACCURACY ATTAINABLE

Methods of Measurement	Error (±%)	Total Error for 19.4° C Range (± °C)	Total Error for 27.8° C Range (± °C)
Non-calibrated two-wire bridge	2.0	0.39	0.56
Non-calibrated three-wire bridge	1.6	0.31	0.44
Calibrated two-wire bridge	1.8	0.35	0.50
Calibrated three-wire bridge	1.5	0.29	0.42
Calibrated three-wire with special amplifier	0.5	0.10	0.14

If a separate temperature gauge and a higher quality dc amplifier were used, an accuracy of ±0.5 percent could be obtained.

Effect of Transducer Accuracies on the Control System. The resulting accuracies of the pressure and temperature measurements are tabulated below to study their effect on the sensitivity of the helium bubbling control system.

Note in Table 3 that, by decreasing the temperature measurement range, an accuracy improvement

in terms of degrees is achieved. The resultant error in vaporization temperature in the pressure channel, E_p, is the sum of the pressure transducer error and the DFG error. The error in the LOX temperature measurement, E_t, is the same as the error of the temperature transducer. Total error for the control system would be the sum of the errors of the pressure and temperature channels.

$$\text{Control Error} = E_p + E_t .$$

To prove the feasibility of the system, transducers were selected which would represent those specified in the S-IC-1 measuring program. A 137.9 N/cm^2 pressure transducer and a platinum resistance thermometer using the standard flight model dc amplifier were selected. The control error would be pressure error plus temperature error, or 1.66°C.

It is desired that the suction line temperature be no closer than a certain differential temperature (ΔT) from the vaporization point before helium bubbling is initiated. The ΔT originally selected was 0.56°C. The control set point is the sum of ΔT and the control error, or 2.22°C. Actual initiation of helium bubbling could occur at any point in the alarm range, which is within plus or minus the control error of the control set point (2.22° ± 1.66°C). The straight addition of pressure and temperature errors adds a measure of reliability to the accuracy calculations.

The transducer evaluation indicated that, by using standard instruments while reducing the range of the measurement, an improvement in the control accuracy can be made. By using a 69 N/cm^2 pressure transducer and reducing the range of the temperature measurement to 19.4°C, the control error would be 0.96°C. The control set point would be 1.52°C, and the alarm range would be 1.52° ± 0.96°C. If expenditures were increased for the transducers and signal conditioning equipment, considerable improvement in the accuracies could be obtained. Using a 69 N/cm^2 strain gauge pressure transducer, pressure error would be 0.39°C; and using a special high accuracy amplifier for the temperature transducer, temperature error would be 0.11°C. The control error, obtained by adding pressure error and temperature error, would be 0.5°C. The control set point would be 1.06°C, and the alarm range would be 1.06° ± 0.5°C. This alarm range represents the best accuracy that can be reasonably expected using the proposed design for the helium bubbling control system.

Recent tests have indicated that helium bubbling will be initiated at a differential temperature greater than 2.78°C; therefore, flight measurement transducers will probably be sufficiently accurate to obtain satisfactory results.

Description of the Helium Bubbling Control Circuitry. The helium bubbling control circuitry (Fig. 3) includes the following components (Fig. 2):

Regulated power supply (two)

Voltage follower (three)

Diode function generator

Comparator-amplifier

Coefficient and control setting network

Voltage selection and calibration network

Miscellaneous circuitry

Two identical transistorized regulated power supplies provide positive and negative 15 volts required by voltage followers and the comparator-amplifier; excitation voltage for the pressure transducer; and current for the diode function generator, internal calibration network, and coefficient and control setting circuit.

The three voltage followers used in the circuit are designated A1, A2, and A3 in the schematic (Fig. 4). All three are solid state operational amplifiers and are used in the isolation amplifier (gain =1) configuration to provide very high input and very low output impedances, thus eliminating the effect of loading on the operation. Adjustable resistors R40, R42, and R55 are external offset zero trim potentiometers.

The nonlinear relationship between the pressure and the evaporation temperature is derived by means of a diode function generator formed by resistors R46 through R56 and the two diodes CR10 and CR11. A 10,000 ohm thermistor compensates the ambient temperature variations.

Resistors R15, R28, and zener diode CR9 with amplifier A4 form the comparator-amplifier. A4, like A1, A2, and A3, is an operational amplifier with a gain of approximately 10,000. The theory of operation of the comparator-amplifier is as follows. Assume an open loop gain of 10,000 and ± 12 volts saturation for

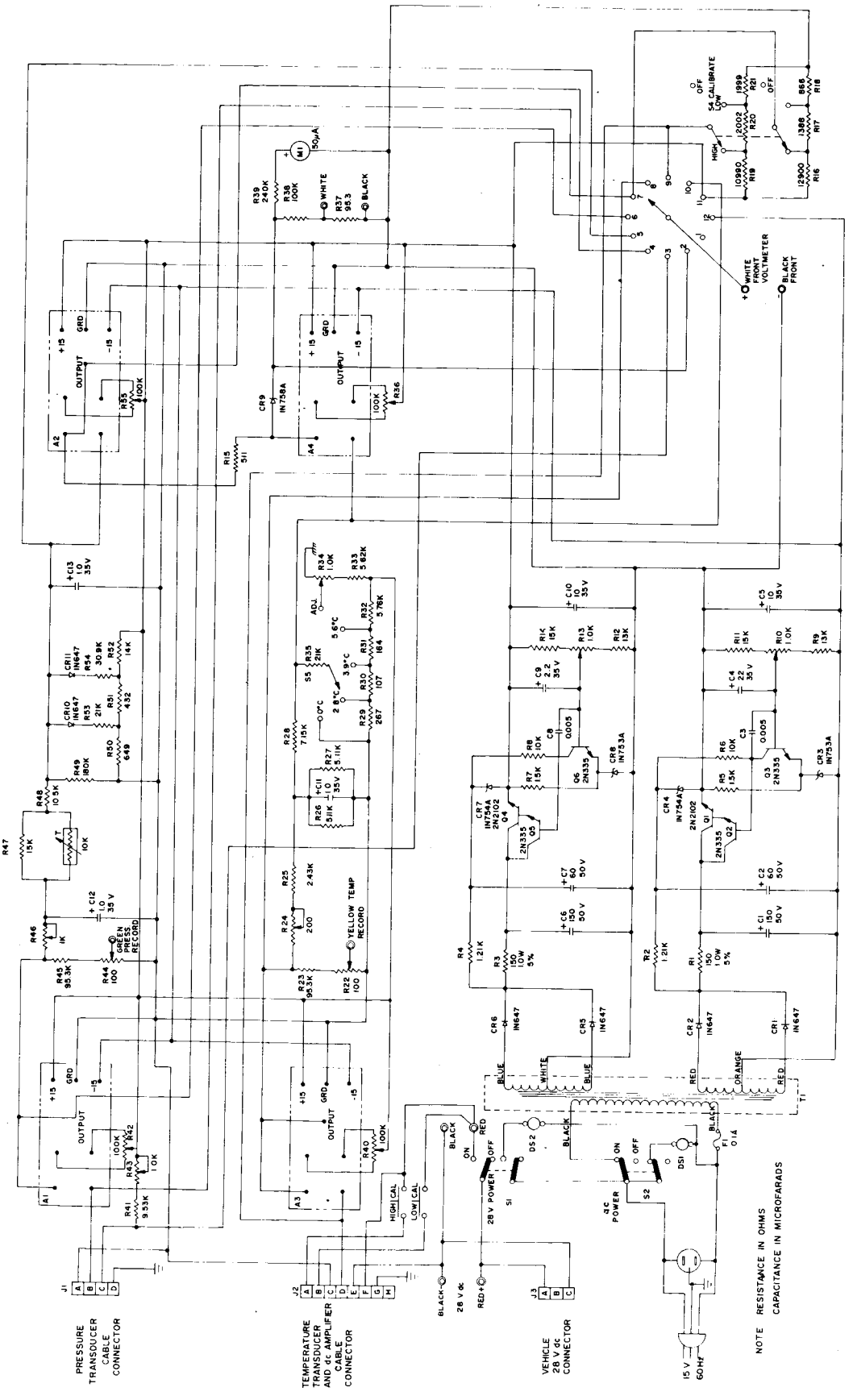

FIGURE 4. SCHEMATIC OF HELIUM BUBBLING CONTROL BOX

the amplifier; if the diode were not across the amplifier, any voltage difference of 12/10,000 = 0.0012 volts or greater would give an output of positive or negative 12 volts depending upon the polarity of the input signal. The diode limits the negative output to approximately -0.5 volts or less. If the diode has a zener voltage of 10 volts, output in the positive direction cannot exceed 10 volts. During the actual operation of the system, the signal (vaporization temperature) applied to the amplifier through R15 is normally higher than the signal (temperature) applied through R28 by at least 1.2 millivolts. Therefore, the output of the amplifier is approximately -0.5 volts. As the emergency condition is approached, the magnitude of the signal coming through R28 increases; this increase, if further amplified by the comparator, causes the output to swing from -0.5 to + 10 volts almost instantly.

The coefficient and control setting network is formed by an attenuator consisting of resistors R24, R25, R26, and R27, and a biasing arrangement consisting of resistors R29 through R34. R28 and R35 act as adding resistors by isolating the two networks. By means of S5, four discrete temperature differential settings can be obtained; by means of R36, any temperature differential setting between 0° and 5.6°C can be obtained.

All important voltages in the operating system can be selected and read with a voltmeter at S3. The calibration network formed by resistors R16 through R21 is used to verify the proper operation of the circuit and to adjust the amplifier. The two switches designated as HI CAL and LOW CAL are used to calibrate the temperature transducer/amplifier combination.

Voltage dividers R44, R45 and R22, R23 provide an attenuation of 1000 for recording purposes. Resistors R37 and R38 also attenuate the output signal by a factor of approximately 200 for recording purposes.

System Performance Characteristics. The 137.9 N/cm^2 potentiometric flight-model pressure transducer was calibrated over its operational range. The resulting calibration curve is presented in Figure 5.

The platinum resistance flight-model temperature transducer was also calibrated over its operational range, -185° to -155°C, and found to be nonlinear.

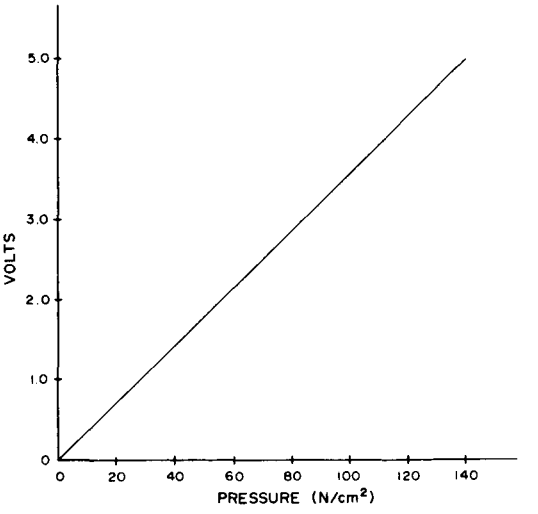

FIGURE 5. FLIGHT PRESSURE TRANSDUCER CALIBRATION

The resulting calibration curve is presented in Figure 6.

The system's circuitry performance characteristics were obtained during operation with the transducers electronically simulated. The pressure transducer was simulated by a 2000 ohm potentiometer in series with a 3000 ohm resistor; 5.076 volts was applied across this series combination at the source end of the cable. The potentiometer output was adjusted manually to give different voltage values corresponding to pressure values from 20.7 to 55.1 N/cm^2. The temperature transducer was simulated by a decade resistance box. At each pressure setting, the value of resistance was varied until an output signal (approximately half scale deflection) was observed on the front panel meter. When the signal appeared, the voltage at pin 7 of S4 was read and recorded. The

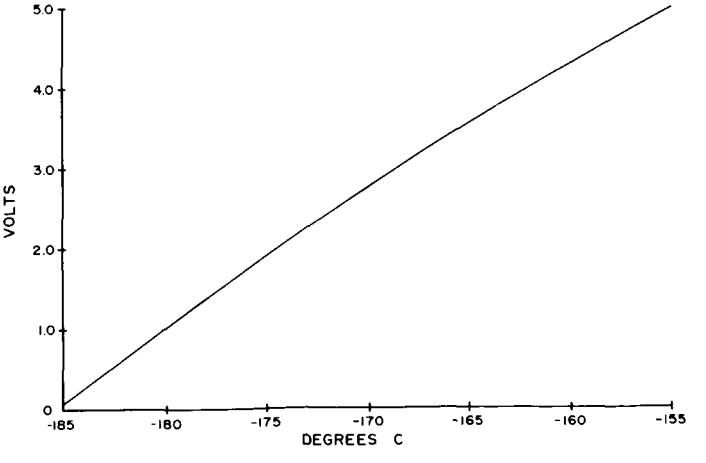

FIGURE 6. FLIGHT TEMPERATURE TRANSDUCER CALIBRATION

corresponding temperature was obtained from the calibration curve of the temperature transducer. This procedure was repeated at differential temperature settings of 0°, 3°, 4.2°, and 5.8°C at each pressure value from 20.7 to 55.1 N/cm^2. System calibration data are plotted in Figures 7A and 7B. Notice that all four differential temperature setting curves do not maintain a constant difference of temperature in relation to the vaporization curve; these differences get smaller as pressure increases. This condition is caused by the nonlinearity of the temperature measurement. When the diode function generator was designed, the temperature measurement was assumed to be linear.

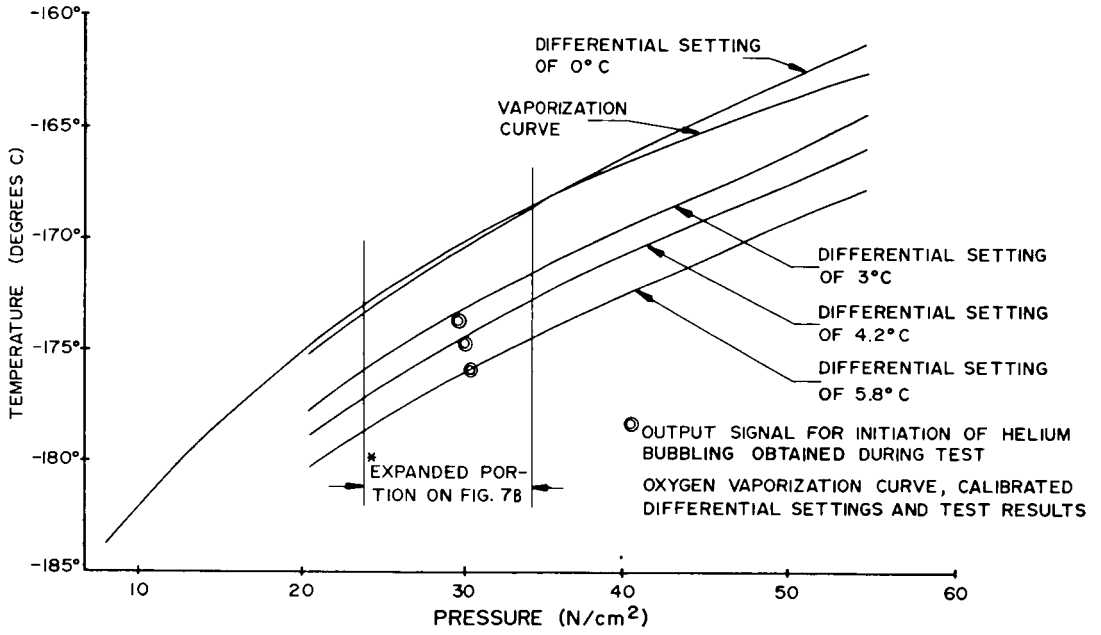

FIGURE 7A. SIMULATED SYSTEM CALIBRATION

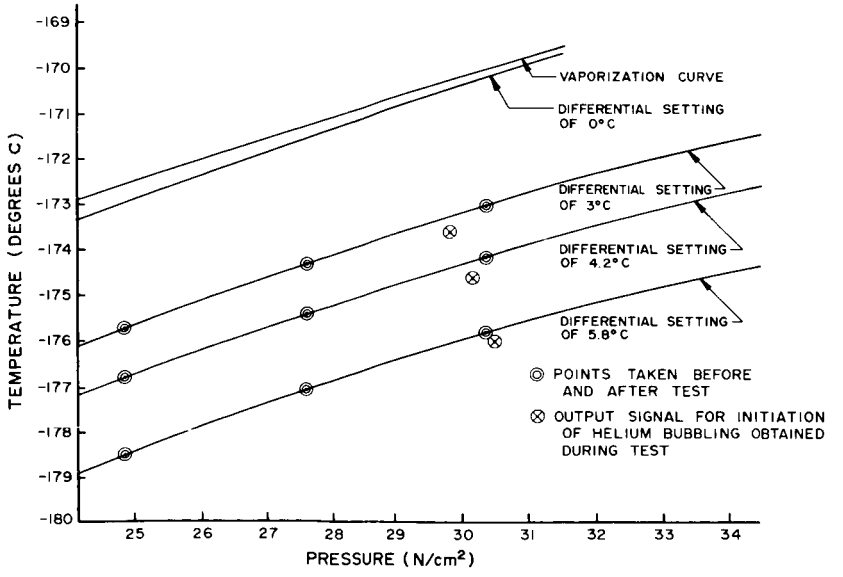

FIGURE 7B. EXPANDED PORTION FROM FIGURE 7A

OPERATIONAL TESTING OF THE DEVELOPMENT SYSTEM

Operational tests were performed to demonstrate the feasibility of the entire helium bubbling control system. The flight measurement pressure and temperature transducers were mounted in a LOX suction line test facility that simulated the vehicle LOX suction lines and tank. Three successive control set points, 5.8°, 4.2°, and 3° C below LOX vaporization temperature, were established by a switch in the system circuit. At each set point, the system correctly emitted an alarm signal within the prescribed alarm range as LOX inside the test suction lines warmed toward vaporization temperature. In an operational system, the alarm would have released gaseous helium into the suction lines to reduce the danger of LOX vaporization and subsequent geysering. These results are presented in Table 4.

CONCLUSIONS

The results of the theoretical study and the feasibility test indicate that a system can be developed which would reliably initiate helium bubbling into the S-IC LOX suction lines to prevent geysering.

In a test using the least sensitive of the systems considered, i.e., a 137.9 N/cm^2 pressure transducer and a 28° C range for the temperature measurement, a maximum error of 0.35° C resulted. This result indicates that the calculated values could be depended upon over the necessary period of time and over a large variation of ambient temperature.

A development system produced for a feasibility test does not necessarily, however, incorporate all the features that an operational system should have. Features not included in the feasibility model would be required in the operational system. The units should be self-checking in case of malfunction; an alarm should be initiated, the malfunctioning unit automatically turned off, and the system switched to manual operation. A pressure transducer and a temperature transducer should probably be installed in each suction line. A "signal processor" may therefore be desirable to select the transducer combination approaching or nearest the alarm condition and to provide an analog display of the two signals. All transducers should, however, be connected to initiate helium bubbling.

A successful operational helium bubbling control system will allow the conservation of helium, which is considered a critical item in short supply. Helium release would be initiated only as needed, rather than continuously as in some space systems.

TABLE 4. FEASIBILITY TEST RESULTS

Control Set Point (°C Below LOX Vaporization Point)	Time From End of Thermal Pumping to Alarm Signal (seconds)	LOX Line Pressure (N/cm^2)	LOX Line Temperature (°C)	LOX Vaporization Temperature (°C)	System Error (°C)
5.8°C	220	30.48	-176	-170	-0.2
4.2°C	430				-0.35
3.0°C	550	29.79	-173.6	-170.3	-0.3

C. AN UP-CONVERTER/DOWN-CONVERTER METHOD OF DATA TRANSMISSION by Edmund H. Gleason

An up-converter/down-converter wideband microwave relay link is presented. The system involves converting VHF telemetry signals to microwave frequencies for transmission and then converting them back to VHF at the receiving site for demodulation.

Also discussed are the advantages and disadvantages of the system as compared to existing means of relaying telemetry data via microwave links.

Author

INTRODUCTION

As launch vehicles increase in size and complexity, additional telemetry links are required to handle transmission of the increasing number of measurements. For example, Saturn V will have as many as 24 VHF telemetry links in the 215 to 260 MHz band, causing checkout requirements and problems to become quite complex. Allowing each onboard transmitter to radiate from the vehicle antennas would require radio frequency silence in the vicinity of the launch area. If the checkout is prolonged, other vehicle checkouts would be delayed.

A proposed system to eliminate these problems involves up-conversion of the VHF telemetry frequencies, which can be transmitted within a tight directional beam. To prove the feasibility of such a scheme, an experimental system was devised to transmit quick-look SA-6 telemetry data from the Green Mountain receiving site to the Astrionics Laboratory ground station at the Marshall Space Flight Center, a distance of about ten miles.

SYSTEM CONCEPT

The only change required within the vehicle is the addition of a coaxial switch, a directional coupler, and a dummy load (Fig. 1). For checkout, the

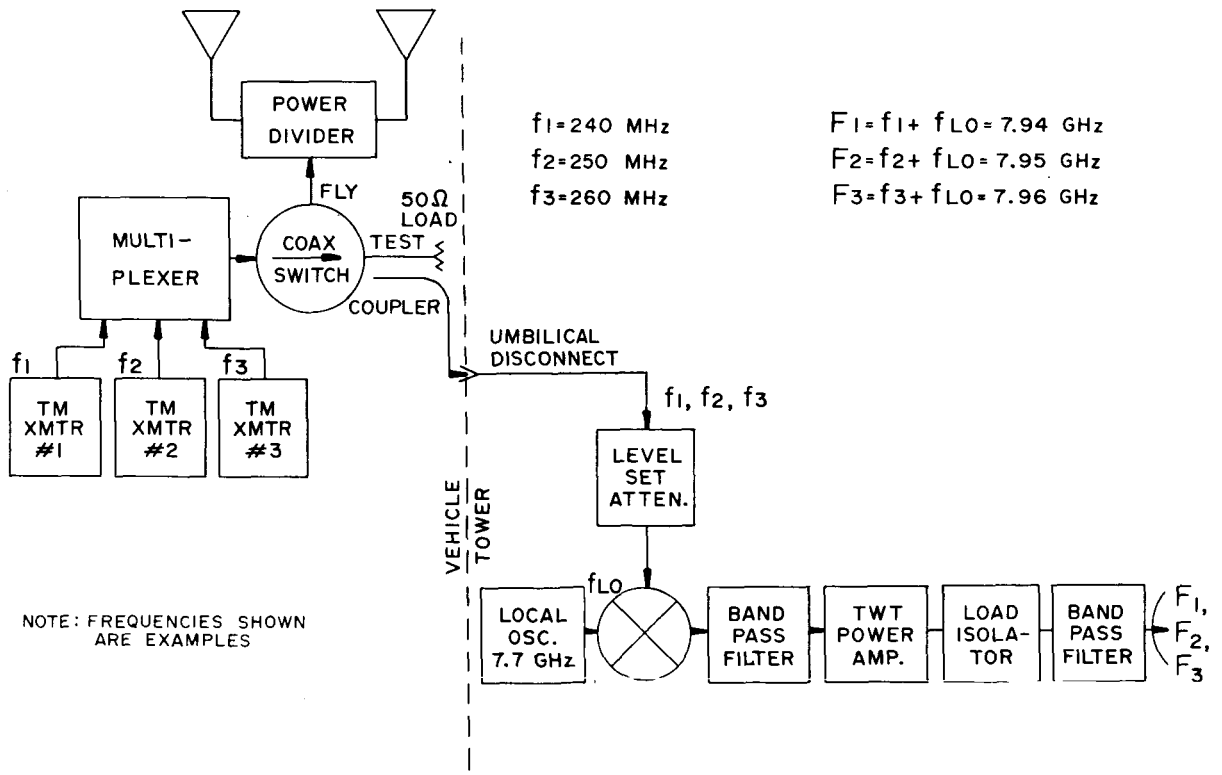

FIGURE 1. VHF-TO-MICROWAVE UP-CONVERTER/TRANSMITTER FOR LAUNCH-PAD INSTALLATION

coaxial switch is placed in the TEST position and a portion of the power is sampled by the coupler and routed to the umbilical tower. These signals are applied to a mixer along with the output of a stable local oscillator (stalo) operating at, for example, 7.7 GHz. The mixer output is filtered to allow only the upper sideband frequencies in the 7.915 to 7.96 GHz band to pass on to the traveling wave tube amplifier. The amplified signals are then transmitted via a microwave link to the receiving site.

The receiving end is shown in Figure 2. The incoming microwave frequencies are heterodyned with a 7.7 GHz stalo signal to recover the original VHF telemetry frequencies, which are then amplified and routed to individual receivers for demodulation and recording.

The advantages of such a system are obvious. Only the up-converted microwave frequencies are allowed to radiate and these are kept within a tight beam directed to the receiving site. Simultaneous checkout of several vehicles can take place simply by assigning different microwave bands to each pad. Checkout accuracy is maintained because the up-conversion and down-conversion processes do not deteriorate the signals in any way.

Solid state multiplier chains that provide stabilities of one part in 10^7 long term are available. Stabilities one magnitude better are within the state of the art. The resulting long term system drift, assuming the worst case, would not exceed 1600 Hz, which is well within the tolerances of telemetry receivers having a bandwidth of 500 kHz.

SYSTEM DESIGN

Output Sampling

The first requirement of the transmitting system is to sample the outputs of each VHF telemetry link within the vehicle. This feature can be accomplished by installing a remotely controlled, single pole, double throw coaxial switch in the telemetry antenna line and routing the sampled outputs through the umbilical disconnect to a level set attenuator. The attenuator can then be adjusted to provide a nominal 0.1 milliwatt (-10 dbm) per channel signal for application to the up-converter.

Up-Converter

The up-converter consists of an Orthomode balanced mixer and a local oscillator. Figure 3 shows a

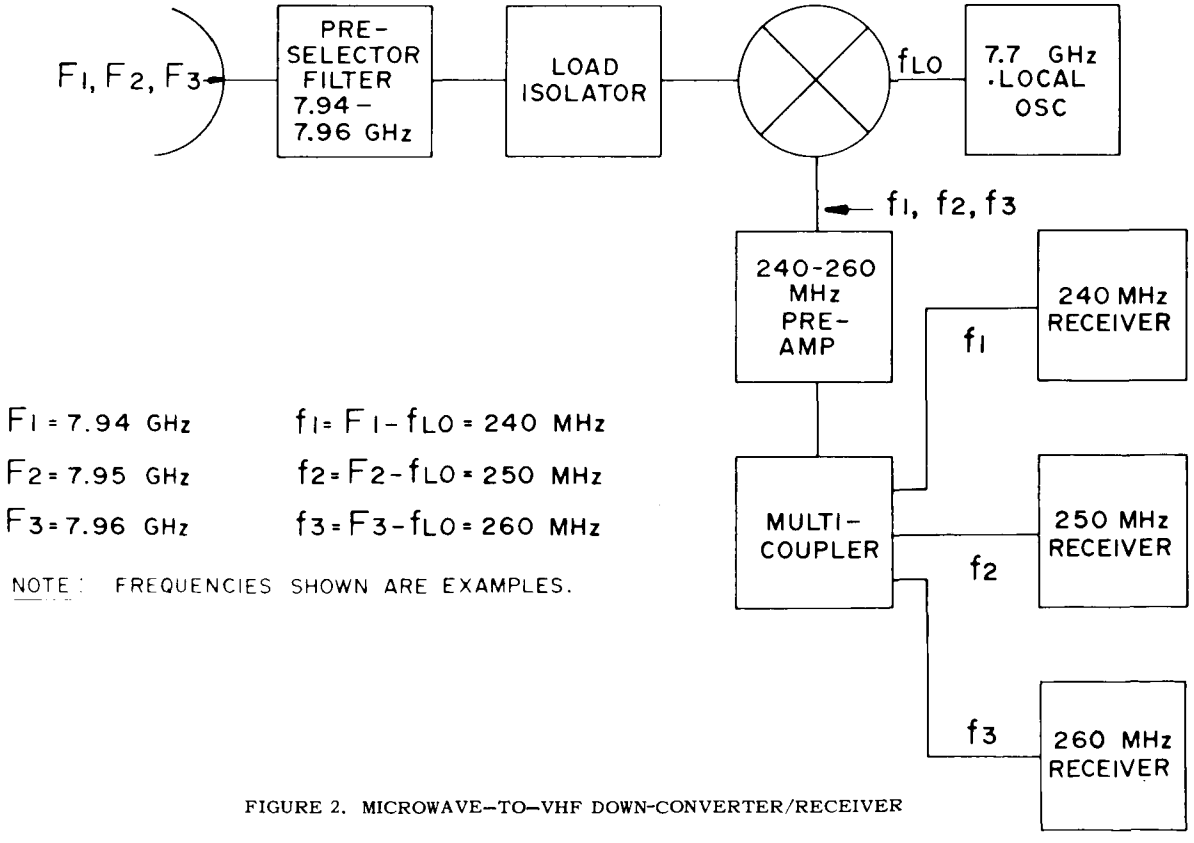

FIGURE 2. MICROWAVE–TO–VHF DOWN-CONVERTER/RECEIVER

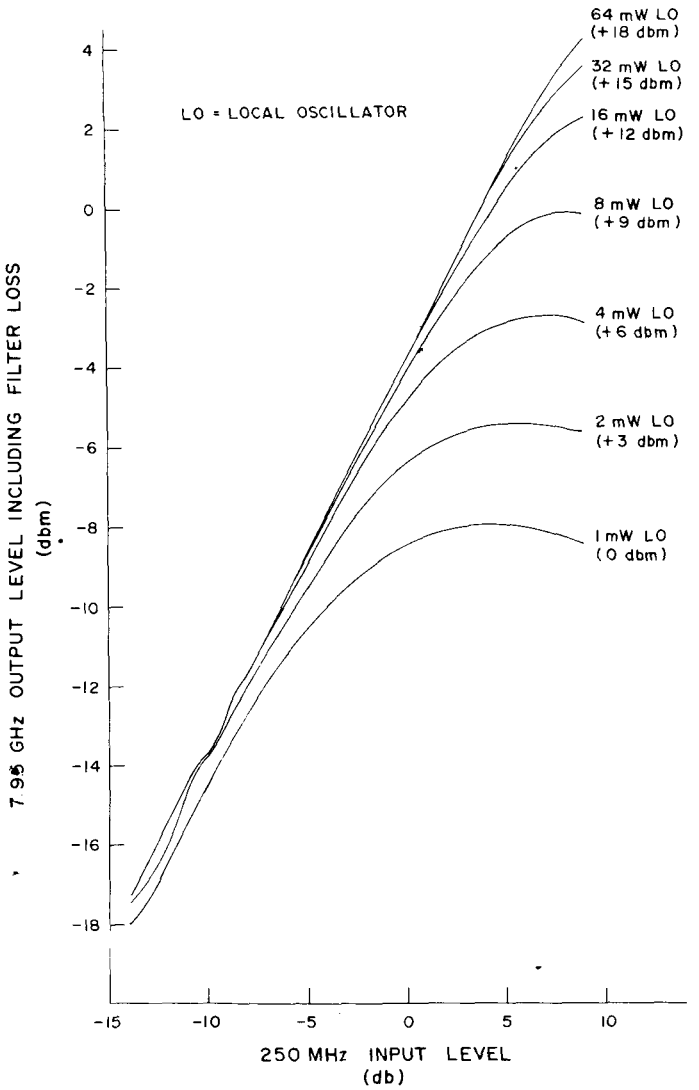

FIGURE 3. EFFECT OF LOCAL OSCILLATOR POWER ON MIXER CHARACTERISTICS

family of curves of input versus output characteristics for different local oscillator power input levels. The output of the mixer, produced by heterodyning action, consists of the first order upper and lower sidebands, the suppressed carrier, and the higher order sidebands.

The mixer characteristic becomes more linear as local oscillator power is increased (Fig. 3). It is important that the most linear characteristic be used to minimize cross modulation effects between channels. Therefore, a local oscillator drive level in the range of 64 to 150 milliwatts should be used to operate the mixer in the linear region. Diode burnout level is approximately 300 milliwatts; the maximum drive level is limited to 150 milliwatts by imposing a safety factor of two. Assuming a maximum of 24 channels, there will be a total VHF signal power of 2.4 milliwatts (+3.8 dbm) applied to the mixer. Figure 3 shows that for this level the mixer will still be operating within the linear portion of the curve for a 64-milliwatt local oscillator drive level and the resulting upper sideband output level will be 0.045 milliwatts (-13.5 dbm).

To achieve the desired stability of one part in 10^7, a local oscillator source consisting of a crystal-controlled varactor multiplier chain is preferred. A klystron, phase locked to a crystal oscillator reference, could also be used but requires much higher voltages and would be much larger.

Since only the first order upper sidebands are to be transmitted, a bandpass filter must be provided at the mixer output to adequately attenuate the local oscillator signals, the lower sidebands, and the higher order sidebands. The filter must have a 45 MHz flat bandwidth. All signals outside this passband must be attenuated at least 60 db, since the filter is followed by a wideband power amplifier.

Power Amplifier

To amplify the 0.045 milliwatt (-13.5 dbm) per channel signals to 100 milliwatts (+20 dbm), a traveling wave tube amplifier with 33.5 db gain is required. This amplifier must be operating below saturation to minimize any cross modulation effects between channels. Amplifiers with these capabilities are presently available with mean-time-before-failure rates higher than 10,000 hours and with completely solid state power supplies.

Receiving System

The receiver must be capable of receiving the transmitted signals, down converting to VHF, and providing outputs for each of the VHF telemetry receivers required for checkout of the vehicle.

To prevent interference from other microwave sources, a preselector with characteristics identical to those of the filter in the transmitter is used. A low noise mixer preamplifier and a local oscillator source is required to convert the microwave signals back to VHF frequencies. The local oscillator must have the same frequency output and the same stability

as the one used in the transmitter. However, the required power output is only 1 to 3 milliwatts, thereby reducing the size of this device as compared to the transmitter local oscillator.

To provide the outputs for the telemetry receivers, a passive multicoupler is used at the output of the mixer preamplifier. The receivers are then tuned separately to each of the 24 channels, enabling checkout of the systems.

EXPERIMENTAL SYSTEM

To substantiate the feasibility of the proposed system, an experimental link was constructed to relay telemetry signals received during the SA-6 launch. The VHF-to-microwave up-converter/transmitter shown in Figure 4 was located at the Green Mountain receiving site some ten miles from Astrionics Laboratory at MSFC. The principle was the same as that of the launch pad scheme except that the signals from the vehicle were received by a tri-helix antenna, amplified, and then converted to microwave frequencies for transmission to Astrionics Laboratory. The receiver/down-converter is shown in Figure 4 and is identical to the one proposed for launch pad checkout.

Since low level received signals were being dealt with in this case, maintaining a desirable signal-to-noise ratio for the overall system required use of a VHF preamplifier with a noise figure equal to or better than that of the receivers used. Also, the overall gain in the transmitting system was greater than the loss caused by the frequency conversion process, the insertion loss of the components used, and the microwave path loss.

Figure 5 shows the measured system signal-to-noise characteristics that were determined by applying an FM modulated signal to the VHF preamplifier at the transmitting end and measuring the video signal-to-noise ratio at the receiving end. The resultant characteristics are nearly identical to those of a typical telemetry receiver, thus demonstrating the superiority of this system to a typical microwave link utilizing subcarrier channels with no better than a 30 db signal-to-noise ratio per link.

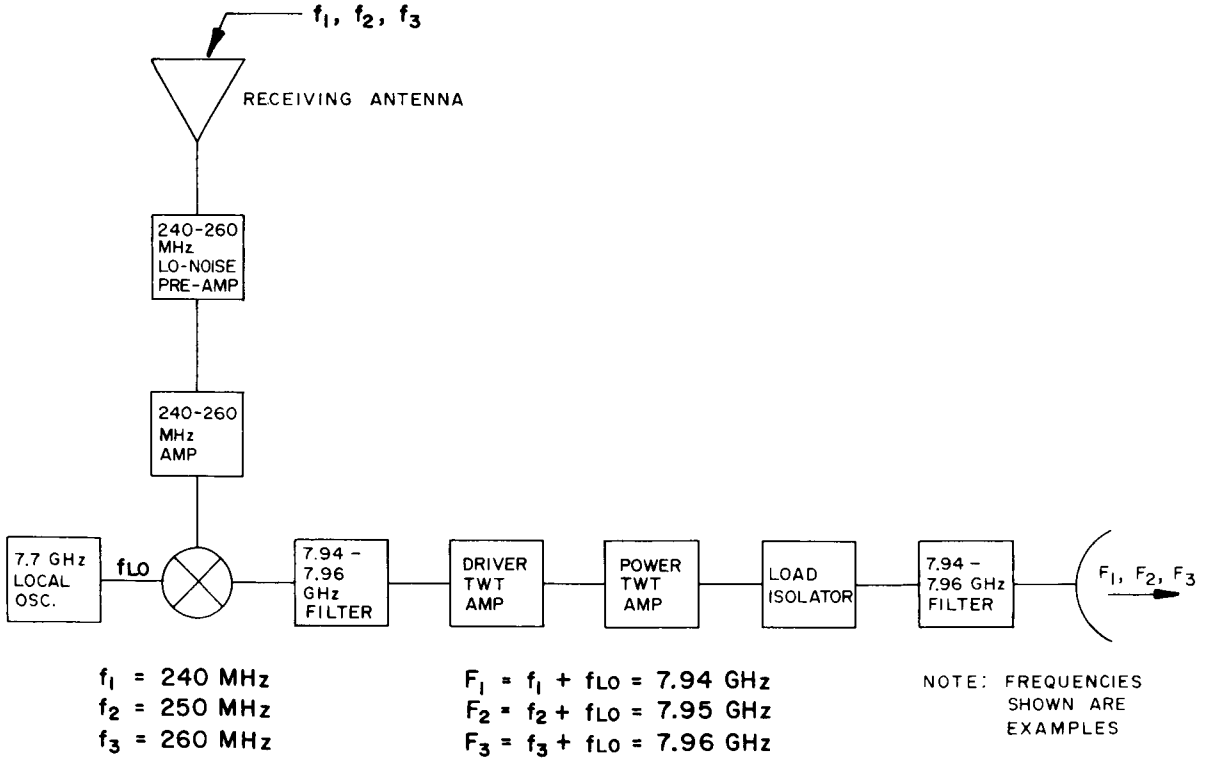

FIGURE 4. VHF–TO–MICROWAVE UP-CONVERTER/TRANSMITTER (GREEN MOUNTAIN)

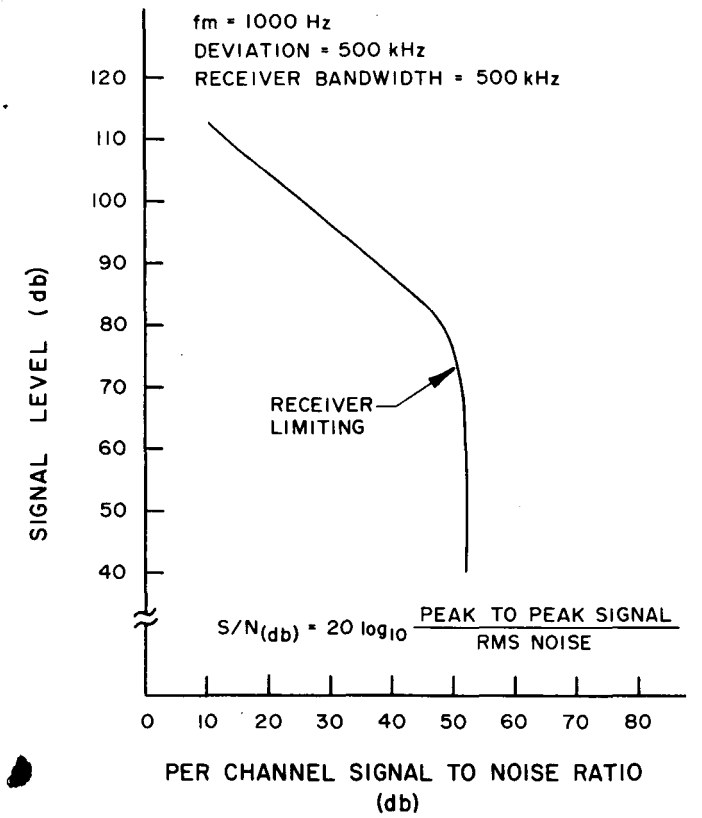

FIGURE 5. FM–MODULATED VHF SIGNAL APPLIED AT GREEN MOUNTAIN AND RECEIVED AT ASTRIONICS LABORATORY

The only disadvantage of this system is high level interference in the 240 to 260 MHz band. Because this is picked up by the tri-helix antenna, saturation of the amplifier occurs, blocking out the lower level telemetry signals. However, RF silence was maintained during the SA-6 flight and the system provided excellent quick-look data to the Astrionics Laboratory ground station.

It should be noted that no interference problem would result in the launch pad scheme because the VHF signals are carried via "hard line" and the microwave frequencies are held within a directional beam.

CONCLUSIONS

1. The proposed microwave relay system indicates capabilities for eliminating problems encountered during telemetry checkouts for large boosters.

2. The proposed system is simple to devise, should be relatively trouble free, and should not introduce any inaccuracies in the checkout results.

III. PUBLICATIONS AND PRESENTATIONS

A. PUBLICATIONS

SATURN INSTRUMENTATION SYSTEMS, J. T. Powell, ISA Journal, November 1964 (also presented at the 10th National Aerospace Instrumentation Symposium, New York, N. Y., May 4-6, 1964)

A brief description of the Saturn vehicles is given, delineating the makeup of and differences between the Saturn I, Saturn IB, and Saturn V. Certain ground rules and constraints for instrumentation system design are discussed. The measuring system (transducers and signal conditioning) is outlined, showing the signal paths into the telemetry systems. Various telemetry modulation and multiplexing methods are defined, and the combining of these techniques into a typical Saturn telemetry system is illustrated. Special emphasis is given to digital techniques and their interrelationship to vehicle checkout procedures. Radio frequency tracking systems used are briefly discussed, giving the characteristics of each and the coverage obtained. Command systems for range safety and guidance are explained in some detail. The use of optical instrumentation (television and film cameras) is covered, showing the arrangement planned for Saturn V. The "operational" Saturn V vehicles to be used for moon launches have somewhat reduced instrumentation and are briefly discussed.

STABILITY OF A THIRD ORDER NONLINEAR DIFFERENTIAL EQUATION, Bernard Asner, Jr., IEEE Transactions on Automatic Control, October 1964, Vol. AC-9

Utilizing the second method of Liapunov, the stability properties of a third order nonlinear differential equation are investigated. The Liapunov function used establishes asymptotic stability in the large if the nonlinear function is restricted to a sector for which the lower bound satisfies an inequality analogous to the Routh-Hurwitz conditions.

RADIO FREQUENCY EVALUATION OF SA-4 VEHICLE, Olen Ely, MTP-ASTR-I-64-3, January 15, 1964

All radio frequency systems on board the SA-4 vehicle functioned properly throughout powered flight. The systems were still operating at the time of reentry; but some data were lost on the tracking systems because of the rolling and tumbling of the vehicle. This was expected since the tracking system used only one antenna.

Good telemetry data were received at the Cape Telemetry 2 station throughout the entire powered flight, including retrorocket ignition. Some of the smaller stations experienced interruptions during this time.

Main engine flame attenuation was similar to previous flights. Retrorocket attenuation was more severe in some instances than on SA-3. The most significant result of retrorocket firing was that it caused the signal to be attenuated and noisy for approximately five to six seconds; yet the retrorockets burned for only two seconds.

This was the first flight carrying the radar altimeter and the Mistram tracking system. The roll of the vehicle caused some problems with the radar altimeter; however, the equipment performed satisfactorily. A comparison of the data from the Azusa system, the UDOP system, and the Mistram system shows that the data agreed within three to five meters during powered flight.

DISCRETE ACTIVITY INDICATOR SYSTEM, George A. Bailey, NASA TM X-53045, May 4, 1964

A discrete activity indicator system processes 768 discrete signal inputs and presents information to a computer only when a change in an input occurs. Resolution time of the system is approximately 1.2 milliseconds for 1000 discrete inputs.

A basic clock in the system drives a functional clock which, in turn, drives a binary counter and six 8-phase

drivers in parallel. Each 8-phase driver operates a 128-way current-steering switch, which sequentially interrogates the cores of a 128-bit memory bank. If a change occurs in a discrete signal input (from 0 to 28 V dc or 28 to 0 V dc), an output is obtained from the associated memory core (when the core is interrogated) and applied to a sense amplifier. The outputs from the sense amplifier and the binary counter are then applied to a system register for transfer to the computer. These signals allow the computer to determine which discrete signal changed and the direction of the change. When a change occurs, a priority-interrupt circuit stops the interrogation until the computer processes the information. After the information is processed, a clock-start multivibrator allows the interrogation to resume.

The power requirement for the system is reduced 75 percent by using a ground commutator to turn on the discrete drivers of the memory in groups of 16 when each particular group is being interrogated.

Positive synchronization between the binary counter and the current-steering switches is provided by a binary synchronizer.

A NONDESTRUCTIVE MEMORY BUFFER USING SINGLE APERTURED CORES, George A. Bailey, NASA TM X-53057, June 4, 1964

A nondestructive memory buffer using single apertured cores is described. The principle of operation is that of using read currents and a decoding device to rewrite into previously read cores. This memory operates faster and consumes less power than those using multi-apertured cores. The supporting logic system features unconventional use of magnetic devices to minimize the need for semiconductors.

INFLIGHT GRAVITATIONAL COMPUTATION, Joseph R. Dabbs, NASA TM X-53061, June 9, 1964

A generalized scheme of gravitational computation was considered for solution by airborne digital vehicle computers. The only assumption was that the coordinate systems used were rectangular, orthogonal, and right-hand. A computational scheme was derived that should be valid for any Saturn class vehicle computer and requires only the change of certain constants for any change in mission.

An added advantage of this scheme is that by inserting different constants the gravitation function of the moon would be readily computable with the same set of equations.

The scheme presented is readily programable and has inherent scheme accuracy sufficient for any foreseeable missions.

RADIO FREQUENCY EVALUATION OF SA-5 VEHICLE, Olen Ely, R. W. Hockenberger, Parley Howell, and Geddes Boone, NASA TM-X53073, June 10, 1964

All radio frequency systems on the SA-5 vehicle performed satisfactorily except the radar altimeter, which was unable to remain in a locked condition. The only other discrepancy was an instantaneous drop of between 8 and 10 db in the C-band radar signal level at 472.8 seconds.

Signal strength degradation caused by main engine flame was less severe than on any previous Saturn flight. The level of attenuation varied from station to station, reaching a maximum of 26 db on VHF telemetry at the Cape Telemetry 2 station. UDOP signal strength data showed a maximum attenuation of 15 db. Higher frequency equipment, such as Mistram, Azusa/Glotrac, and C-band radar, was not significantly affected by the main engine exhaust plume.

Retrorocket attenuation was very severe, causing all signals to drop to threshold. However, C-band radar recovered before retrorocket burning was completed. Ullage rockets alone did not affect the signal level of any RF system.

PRECISION OPTICAL TRACKING SYSTEM FOR ADVANCED LAUNCH VEHICLES, Charles L. Wyman, Klaus Juergensen, Robert L. Kurtz, Larry Hayes, and John M. Gould, NASA TM X-53076, June 25, 1964

The development efforts on an experimental optical radar system for precision tracking for advanced launch vehicles during the early launch phase are described. Basic concepts for a prototype system are discussed along with some advanced techniques that are being investigated. Analyses and investigations concerning the project are discussed. An error analysis is made assuming a tracker that measures elevation angle, azimuth angle,

and distance in digital form. The analysis is concerned with errors in distance, velocity, and acceleration computed from distance measurements. The distance measurements are assumed to be inaccurate by a systematic error and a distributed error. Also, the error caused by linear interpolation between displayed points is considered. No data smoothing is taken into account. Equations are developed that can be used to obtain optimal data rate and highest frequency with which the true range and angular parameters may change without causing errors exceeding the required accuracies.

A trajectory analysis is performed utilizing a typical Saturn V trajectory to determine the dynamic range of the instrument parameters. Vehicle and instrument parameters are plotted against time, and the curves are used for design purposes.

A range analysis develops optical radar equations. The system uses retrodirective corner reflectors on the booster to increase the return signal. The increase is calculated and included in the range equations along with calculations of atmospheric attenuation. A preliminary calculation of background radiation is made.

A preliminary synthesis of the tracking mount servo assumes a type one servo with tachometer stabilization. The analysis indicates that the system has the desired static accuracy in the presence of high breakaway friction, can operate at very small dynamic errors, and exhibits good stability.

An investigation concerning refractive and turbulence effects of the atmosphere on laser beams is also discussed.

DEVELOPMENT OF SATURN FIRE DETECTION SYSTEMS, H. D. Burke, R. Stockard, and J. E. Zimmerman, NASA TM X-53141, September 24, 1964

The research and development leading to the advancement of fire detection techniques are discussed, with emphasis on the flight fire detection system. This system, which has been designed for flight operation, is an extension of the prelaunch fire detection system presently in use on the Saturn vehicle.

The prelaunch fire detection system is given considerable attention, as well as the fire detection sensing element. Both systems use a thermocouple gauge as the sensing element and operate on the basis of the temperature rate of rise at the gauge, rather than the absolute temperature.

EVALUATION OF ADHESIVES FOR INSTALLING FLAT CONDUCTOR CABLES, Bobby W. Kennedy, NASA TM X-53080, October 8, 1964

Fourteen adhesives for mylar-insulated flat conductor cable were tested for creep and peel strength, corrosion effects, heat distortion, vacuum effects, and cryogenic temperature effects.

Minnesota Mining and Manufacturing Company's 1099 adhesive was found to be the best liquid adhesive. Fasson Products Corporation's S-277 adhesive was found to be the best pressure sensitive adhesive. Dow Corning Company's Silastic 140 is suitable in areas where initial tack is not a problem.

SPACE VEHICLE SA-4, TELEMETRY SYSTEM, E. H. Reeves, Jr., J. R. Stovall, and W. B. Threlkeld, Jr., NASA TM X-53153, October 26, 1964

The performance evaluation of the complete telemetry system (ten links) used for flight testing Saturn vehicle SA-4 is presented. The eight operable telemetry links, the two experimental telemetry links, and the telemetry auxiliary equipment assembly have been technically analyzed on an individual basis.

Statistical analyses were performed on much of the telemetry data, and the results of these analyses are presented.

No RF signal fade or dropout difficulties were encountered on any of the links.

A malfunction of the PCM system occurred during the flight. An analysis of the cause and effect of this malfunction is included.

It is concluded that the overall performance of the telemetry system used for flight testing SA-4 was as anticipated. It is inferred that the derived test data will facilitate the development of more efficient telemetry systems.

SECURE RANGE SAFETY COMMAND SYSTEM FOR SATURN, H. R. Lowery, NASA TM X-53162, November 9, 1964

A high alphabet range safety command concept using digital methods compatible with the present modulation technique used on the Eastern Test Range is discussed.

The new system provides a high degree of protection against intentional interrogation by unfriendly intruders and against unintentional interrogation (false alarms) by noise. The security against intentional interrogation is measured by the fraction of the total code combinations that an intelligent unfriendly interrogator, having unlimited technical resources, would be able to transmit during equipment access time. It is assumed that all system parameters are known to him except the code-of-the-mission. The security against unintentional or randomly generated false alarms is, as it should be, much greater than against intentional, intelligent interrogation. Operational difficulties of handling the security aspects of the system are minimized by using a removable, inexpensive, easily stored code plug to change the code-of-the-mission. All hardware is unclassified except the actual flight code plugs.

In contrast to a binary system, which utilizes a language consisting of only two distinct characters, the new secure range safety command system uses a language consisting of 21 characters. Each character of the 21-character alphabet is formed from a subalphabet of seven symbols taken two at a time. Each symbol is a burst of an audio-frequency tone. A pair of tones transmitted simultaneously comprise a character. This high-alphabet technique provides the necessary high security without sacrificing essential performance characteristics of the present system. Further, the new high-alphabet system is, by design, tolerant of relatively wide radar or pulse interference.

The security is realized mainly by the message format, which consists of a nine-character address word, followed by a two character function (command) word. The limited time of access to the equipment is the final factor in the security.

Each character of the nine-character address word is unique within a given address, and therefore the new system can operate without the necessity of transmitted clock or reference synchronizing information. The symbols are, however, synchronous with the character interval period (and with each other) and are spaced and phased to minimize intersymbol interference, which could create unwanted characters.

The main RF carrier is frequency modulated by a subcarrier system which, in turn, employs a multiple frequency shift (MFS) technique. The term frequency shift keying (FSK) is also used to describe the technique. The portion of the baseband occupied by the subcarrier system is approximately the same as that now reserved and used for range safety purposes. The nominal tone frequencies, however, are not the same as the Inter-Range Instrumentation Group (IRIG) tone channel frequencies. The tone-frequency spacing is, by design, an integral multiple of the character repetition rate. This makes possible a simple phase-coherent tone keying scheme.

The two main vehicular components of the new secure range safety command system (receiver and decoder) are presently being manufactured. Provided all present schedules can be met, prototype receivers and decoders will fly as IU passengers on vehicle SA-8 and several later vehicles. Upon qualification by the Range Safety Activity at PAFB, the new system will become an active system on all Saturn vehicles, replacing the present non-secure equipment.

A system design has been evolved which has a high degree of security, will work with reliability in its expected communication environment, and lends itself to implementation of dependable hardware.

RADIO FREQUENCY EVALUATION OF SA-6 VEHICLE, Olen Ely, R. W. Hockenberger, Parley Howell, and Geddes Boone, NASA TM X-53170, November 24, 1964

All RF systems performed satisfactorily with the exception of C-band radar, which was approximately 10 to 20 db below the theoretical values of signal strength. This system suffered an additional 10 db drop in signal at 480 seconds; however, it recovered at 560 seconds. This was almost identical to the phenomenon that occurred on SA-5 at 472.8 seconds. This malfunction has been attributed to arcing either in the cabling connecting the radar beacon to the antenna or in one of the connectors.

Signal strength degradation caused by main engine flame was very similar to that of SA-5. However, unlike SA-5, some of the signal strength data contained noise caused by main engine exhaust until inboard engine cutoff at 143 seconds.

Retrorocket ignition caused the signal level of all RF systems to drop below threshold. The C-band radar system recovered within 2.4 seconds, prior to any other system.

The ullage rocket exhaust did not noticeably affect the signal propagation. It is possible that the severe attenuation of the RF signals is caused by combining the ullage rocket and retrorocket exhausts.

EVALUATION OF POLYMERIC MATERIALS FOR ELECTRONIC PACKAGING, Bobby W. Kennedy, NASA TM X-53181, December 16, 1964

Certain potting and conformal coating materials were contributing to the failure of critical glass-sealed components and solder joints in cordwood modules and on printed circuit boards. The cause of these failures was determined to be differences in coefficients of thermal expansion for materials. Analysis indicated the necessity of selecting materials with a lower coefficient of thermal expansion for potting cordwood modules and changing from a hard, rigid epoxy to a soft, flexible polyurethane for printed circuit board conformal coating.

Of the four potting materials tested, Emerson and Cuming's Stycast 1090 epoxy was selected for potting cordwood modules.

Three of the coating materials were too thin to support components; therefore, no further testing of these materials is anticipated. However, these materials may be used when a thin protective coating is needed and when component support is not a problem.

Products Research-1538 polyurethane material is recommended and is being used for coating printed circuit boards; however, in high frequency circuits, an epoxy may be used after encapsulating the component with vinyl sleeving to prevent RF losses.

B. PRESENTATIONS

THE APPLICATION OF Z-TRANSFORM THEORY TO THE ANALYSIS OF SWITCHED-TYPE NONLINEAR SYSTEMS, E. S. McVey* and G. S. Nurre, presented at the IEEE Symposium, New York, N. Y., March 23, 1964

The stability of certain discontinuous feedback systems is analyzed by the use of the z-transform theory. It is shown that there can be found in the z-plane a system which is equivalent to the nonlinear system under steady state conditions. The existence of any limit cycle can be found together with the frequency at which it occurs. An intuitive argument for the stability of a limit cycle is also presented. Several examples are worked and the results are compared with those obtained by other methods. The z-transform method is exact and is not restricted by the order of the system.

A SELF-ADAPTIVE TRACKING FILTER, Michael T. Borelli and Hans H. Hosenthien, presented to the SAE Aerospace Vehicle Flight Controls System Committee, Missile and Pilotless Aircraft Subcommittee, New York, N. Y., July 8-10, 1964

This presentation describes an adaptive tracking notch (ATN) filter that has the capability of either gain- or phase-stabilizing the low frequency structural bending modes of large aerospace vehicle boosters, such as Saturn V. The basic principle of the ATN filter is to construct a reversed-phase bending signal, utilizing modulation techniques, and then to sum this constructed signal with the sensor output signal, suppressing the undesired bending signal for gain-stabilization or shifting its phase for phase-stabilization. A brief discussion of the ATN filter's characteristics is presented. Results from analog computer simulations of the Saturn V vehicle utilizing breadboard ATN filters are reviewed and evaluated.

DEVELOPMENT OF SERVOVALVES WITH IMPROVED RELIABILITY FOR SPACE VEHICLES, M. A. Kalange, W. H. Pollock**, and W. J. Thayer***, presented to the SAE Committee A-6, Aerospace Fluid Power Technologies, Boston, Mass., September 14-18, 1964

Considerations for improvement in the reliability of Saturn engine gimbal servosystems are briefly covered.

*U. S. Army
**Cadillac Gage Co.
***Moog Servo Control, Inc.

Saturn I servovalves operate with increased electrical input power. Saturn V vehicle stages will use mechanical feedback actuators with increased electrical input power, larger orifices and nozzle sizes, larger torque motor wire size, and greater spool driving forces.

Further considerations for improvement in system reliability led to the development of servovalves with improved reliability. The primary objective was to develop servovalves that have a higher reliability factor by increasing electrical input power and minimizing sensitivity to fluid contamination. Two approaches were taken; in the first approach, a conventional two stage, double nozzle flapper electrohydraulic servovalve with mechanical feedback from the spool position was used. Methods for optimizing the characteristics effecting the reliability are shown, and the test results are given for the optimized functional model. In addition to being built for use on an electrical feedback actuator, the valve was modified to show that it was designed with sufficient power for its operation on a mechanical feedback actuator. The second approach is also a two stage mechanical feedback servovalve; however, the hydraulic amplifier in this case is of the jet pipe receiver design. The study began with a theoretical analysis of the conventional state-of-the-art servovalves and selection of the jet pipe as offering the greatest potential for high reliability. The study then progressed to a series of test fixtures and breadboard hardware to evaluate the optimized design, which through further development resulted in a functional model. The characteristics of the functional model are presented.

STATUS OF GUIDANCE AND CONTROL METHODS, INSTRUMENTATION, AND TECHNIQUES AS APPLIED IN THE APOLLO PROJECT, Walter Haeussermann and Robert C. Duncan*, presented at the Lecture Series on Orbit Optimization and Advanced Guidance Instrumentation, Advisory Group for Aeronautical Research and Development, North Atlantic Treaty Organization, Duesseldorf, Germany, October 21-22, 1964

Future space missions will place numerous and extremely variable requirements on launch vehicles and spacecraft. To meet these diverse requirements and provide adequate safety for the space crew, guidance and control systems must be extremely flexible. As a means of presenting these requirements and the methods used to meet them, this paper describes the Apollo mission in detail. This description touches briefly on the Saturn-Apollo space vehicle and goes into deeper detail concerning the various phases of the lunar landing mission (including transit between the earth and moon). A detailed description of the guidance and control theory, schemes, and hardware to be used is presented.

A short history and description of the development of the delta-minimum guidance scheme and its successful utilization in ballistic missiles are presented. The path-adaptive guidance theory used to guide the Saturn launch vehicle is discussed in some detail. This theory is based on utilization of the calculus of variations to solve for an optimum path to achieve a given mission. Several means of implementing this theory are being investigated to determine which will be most suitable for achieving the wide spectrum of expected mission with the greatest simplicity and accuracy. The path-adaptive guidance schemes permit the guidance system to accept a wide range of nonstandard conditions and furnish the vehicle with commands to place it on an optimum path.

The Saturn guidance and control hardware is described in detail, including the factors that determine the final selection of components. The guidance and control system is designed around a central system of basic components, principally a digital computer and a data adapter. The subsystems, such as the attitude control and the guidance subsystems, all operate in conjunction with this central system. For unprecedented reliability, redundancy of components and circuits is applied almost throughout the entire guidance and control system.

Flight simulation for verification of component and system design is also discussed. In its early stages, this simulation is accomplished by simulating the components themselves. As development progresses, actual components are placed in the flight simulation.

Prelaunch operations are discussed briefly, followed by a discussion of the operations that occur during earth orbit. One of these operations is the checkout of the onboard guidance and control equipment. Injection of the Saturn-Apollo space vehicle into a translunar conic will not be initiated until the checkout operations have

*Manned Spacecraft Center

been successfully completed. A short description of the transposition and docking maneuver, which occurs after injection, is given.

Following a brief description of the Apollo spacecraft and the attached lunar excursion module (LEM), a general description of the guidance theory that governs their motion is presented. This theory embodies statistically optimum navigation techniques for updating the knowledge of position and velocity in space. The guidance and control hardware used in the Apollo spacecraft and the LEM is described in detail.